The cyanobacterial circadian clock follows midday *in vivo* and *in vitro*

Eugene Leypunskiy[1], Jenny Lin[2], Haneul Yoo[2], UnJin Lee[3], Aaron R. Dinner[1,4*], Michael J. Rust[1,3,5*]

[1] Graduate Program in Biophysical Sciences

[2] Department of Biochemistry and Molecular Biology

[3] Department of Ecology and Evolution

[4] Department of Chemistry and the James Franck Institute

[5] Department of Molecular Genetics and Cell Biology and Department of Physics

The University of Chicago, Chicago, IL 60637

*To whom correspondence should be addressed: dinner@uchicago.edu, mrust@uchicago.edu

ABSTRACT

Circadian rhythms are biological oscillations that schedule daily changes in physiology. Outside the laboratory, circadian clocks do not generally free-run, but are driven by daily cues whose timing varies with the seasons. The principles that determine how circadian clocks align to these external cycles are not well understood. Here we report experimental platforms for driving the cyanobacterial circadian clock both *in vivo* and *in vitro*. We find that the phase of the circadian rhythm follows a simple scaling law in light-dark cycles, tracking midday across conditions with

variable day length. The core biochemical oscillator comprised of the Kai proteins behaves similarly when driven by metabolic pulses *in vitro*, indicating that such dynamics are intrinsic to these proteins. We develop a general mathematical framework based on instantaneous transformation of the clock cycle by external cues, and it successfully predicts clock behavior under many cycling environments.

INTRODUCTION

Circadian clocks generate biological rhythms that temporally organize physiology to match the 24-hour diurnal cycle. Though these clocks continue to oscillate in constant laboratory conditions, in natural environments they are driven by the external cycle of day and night. Because of latitude-dependent changes in the duration of day and night throughout the year, clock architectures must incorporate mechanisms that respond appropriately to environmental signals, such as dawn and dusk, whose schedule changes throughout the year. Data from several species indicate that circadian clocks adapt to different day lengths by modulating their phases relative to the light-dark cycle (1, 2). In this way, circadian oscillators are able to coordinate physiological events relative to specific times of day and, in multicellular organisms, specialized mechanisms exist that allow oscillators in different cells to follow distinct times of day (3, 4). Because the biochemical circuits governing circadian rhythms and light-dark sensing in such organisms are complex, it has been difficult to identify which features of circadian systems are responsible for seasonal adaptation. More generally, it remains unclear what features oscillators must have to respond appropriately to varying light-dark cycles and how those features are implemented molecularly in specific systems.

47 Cyanobacteria present a unique opportunity to elucidate molecular mechanisms in
48 circadian biology because the core oscillator responsible for driving genome-wide transcriptional
49 rhythms can be reconstituted using purified KaiABC proteins, and these proteins have been
50 extensively studied biochemically in constant conditions (5, 6). However, cyanobacteria must
51 contend with large seasonal variations in day length because their natural aquatic environments
52 span a wide range of latitudes (7). Yet, comparatively little is known about how the
53 cyanobacterial clock functions when driven by light-dark cycles that mimic days in different
54 seasons.

55 To study how the circadian clock is affected by light-dark cycles with different day
56 lengths, we developed multiplexed LED illumination devices to grow cyanobacteria in a wide
57 range of light-dark conditions (Fig. 1A). We used square-wave illumination patterns in our
58 experiments, and used the times of lights-on and lights-off as experimental analogs of dawn and
59 dusk, respectively. We defined the day length (τ) as the total time the lights are on each day (Fig.
60 1A). We found that the circadian rhythm in the cyanobacterium *Synechococcus elongatus* PCC
61 7942 (*S. elongatus*) follows a simple rule: the phase of clock-driven gene expression scales
62 linearly with day length and remains fixed relative to the middle of the day over a wide range of
63 day lengths.

64 We biochemically simulated seasonal effects in the reconstituted KaiABC oscillator by
65 driving the Kai proteins with pulses of nucleotides on a 24-hour cycle, simulating *in vivo*
66 metabolic conditions during day and night. Remarkably, this *in vitro* system shows a similar
67 linear scaling of clock phase with simulated day length, indicating that core mechanisms for
68 seasonal adaptation are intrinsic to the Kai proteins. We developed a minimal mathematical
69 model for oscillator entrainment based on rapid transitions between distinct day and night clock

cycles. The model can account for the ability to track midday if the phase shifts caused by dawn and dusk depend linearly on clock time with appropriate slopes. By calibrating this model with independent measurements *in vitro* and *in vivo*, we were able to predict the results of phase response experiments, and the behavior of the clock in non-24 hour light-dark cycles.

The essential feature of the model, the linear dependences of phase shifts on clock time, has a simple geometric interpretation in terms of the deformation of the clock orbit caused by a transition between light and dark. Thus, the entrained behavior of the circadian clock can be captured quantitatively by a mathematical framework with a small number of parameters. This framework in turn can be used to guide the design of experiments that probe the molecular origins of key mathematical features. The precisely defined nature of the cyanobacterial clock facilitates such experiments, but the model is general, so we expect it to be useful for other organisms as well.

RESULTS

Cyanobacteria respond to seasonal changes in day length by aligning the phase of circadian gene expression relative to midday.

S. elongatus is a photosynthetic bacterium whose physiology is closely tied to light and dark. In constant light, the circadian clock exerts pervasive control over gene expression: most transcripts cycle in abundance with ≈24-hour period, with the majority of transcripts peaking either near subjective morning (dawn genes), or nearly 12 hours later, at subjective nightfall (dusk genes) (8, 9). In the dark, however, growth stops, and most gene expression is highly repressed (10–12).

93 Thus, portions of the circadian gene expression program that fall into nighttime hours are
94 strongly attenuated.

95 Viewed in this way, the hours between dawn and dusk provide a limited window for gene
96 expression, so that winter months at high latitude provide fewer daylight hours for this
97 cyanobacterium to accomplish biosynthetic tasks relative to summer months. We surmised that
98 an important function for the circadian clock in this organism might be to schedule gene
99 expression appropriately during daylight hours, when biosynthetic resources are available. We
100 thus expected that asymmetric light-dark cycles mimicking days in different seasons would
101 realign the clock cycle.

102 To systematically study how circadian gene expression in *S. elongatus* adjusts to
103 asymmetric light-dark schedules, we built a microcontroller-driven LED array device and used it
104 to grow cells in 24-hour day-night cycles with photoperiod (day length) varying from 4 to 20
105 hours (Fig. 1A). This LED array was coupled to a plate reader that allowed us to monitor clock
106 output—gene expression from clock-driven promoters—using strains engineered with
107 luminescent reporters for representative dusk (*kaiBC*) and dawn (*purF*) genes.

108 In these experiments, the circadian clock stably entrained to light-dark cycles with a wide
109 range of day lengths (τ = 8-16 hours) within roughly three days (Fig. 1—figure supplements 1,
110 2). We found that the phase of the oscillation, that is, when the peak clock output signal occurred
111 relative to dawn, varied systematically as a function of day length. In general, longer days
112 resulted in the peak reporter signal occurring later in the day (Fig. 1B). By plotting the time of
113 peak reporter signal versus day length, we found that the driven behavior of the clock follows a
114 simple scaling law: the clock phase is proportional to day length (Fig. 1C). The proportionality
115 constant, m, falls in an intermediate range (Table 1) between the limits corresponding to either

116 dawn (m=0) or dusk (m=1) fully resetting the clock. The linear relationship between clock phase
117 and day length with slope $m \approx 0.5$ implies that cyanobacteria set their clock to reach the same
118 internal time at the middle of the daylight hours, independent of day length. This entrainment
119 behavior is not unique to the *kaiBC* promoter; a reporter for *purF*, a representative of the dawn
120 class of genes, shows similar scaling behavior with day length (Fig. 1—figure supplement 3).
121 The fact that the core oscillator of the cyanobacterial circadian clock can be reconstituted
122 *in vitro* from purified Kai proteins (13, 14) naturally led to the question of whether the ability to
123 track midday that we observed *in vivo* is intrinsic to the core oscillator, or if it requires additional
124 factors present in the cell. We thus sought to extend the reconstituted system such that we could
125 drive the biochemical oscillator with rhythmic input signals.
126
127 ***In vitro* reconstitution of seasonal clock response.**
128
129 A purified mixture of the KaiA, KaiB, and KaiC proteins spontaneously generates a stable
130 circadian rhythm in KaiC phosphorylation and in the formation of KaiB-KaiC complexes (13,
131 14). Though the Kai proteins are not light-sensitive, recent work has shown that they are
132 sensitive to metabolite pools that shift in response to changes in photosynthetic activity in the
133 cell: KaiA is sensitive to the redox state of quinones, and KaiC phosphorylation is sensitive to
134 the ATP/ADP ratio (15–17). We thus developed a protocol to mimic repeated light-dark cycles
135 *in vitro* by cycling the ATP/ADP ratio between physiologically relevant levels experienced
136 during day and night, using ADP addition to simulate nightfall ($[\mathrm{ATP}]/([\mathrm{ATP}] + [\mathrm{ADP}]) \approx$
137 25%) followed by buffer exchange into an ATP-only buffer to simulate dawn
138 ($[\mathrm{ATP}]/([\mathrm{ATP}] + [\mathrm{ADP}]) \approx 100\%$) (Fig. 2A).

139 We found that the KaiC phosphorylation rhythm readily responded to this metabolite
140 pulsing protocol. Stepping into the lower ATP/ADP conditions promoted dephosphorylation, in
141 accord with previously published observations (18). Conversely, stepping into higher ATP/ADP
142 conditions favored phosphorylation (Fig. 2B). Pulsing the ATP/ADP ratio in this way caused the
143 KaiC phosphorylation rhythm to synchronize to the external cycle. By the third cycle, the
144 oscillator appeared to have stably entrained, and, similar to the clock behavior we observed in
145 live cells, longer times in daytime buffer led to later peak phosphorylation times. We estimated
146 peak times for these oscillator reactions during the third entraining cycle and found that the
147 phase of the *in vitro* rhythm scales linearly in proportion with simulated day length (Fig. 2C),
148 with KaiC phosphorylation rhythm peaking roughly 3 hours after the midpoint of simulated
149 daytime, suggesting that the reconstituted Kai oscillator is capable of tracking the approximate
150 midday point of an externally imposed metabolic rhythm.
151 To more accurately measure the scaling of entrained phase with day length in KaiABC
152 oscillator reactions, we turned to a fluorescence polarization probe that enables automated
153 measurement of oscillator state with high temporal resolution (Figure 2—figure supplement 1)
154 (19, 20). We used this assay to determine clock phases in free-running conditions after entraining
155 the Kai proteins with three metabolic cycles, analogous to the design of the *in vivo* experiments.
156 We again measured linear scaling of the entrained phase, albeit with a lower slope than the
157 estimate from sparser gel-based measurements of KaiC phosphorylation (m=0.38±0.07 for
158 polarization probe vs. m=0.51±0.04 for phosphorylation data, Figure 2C). Despite the variability
159 in our estimates of m, these measurements argue that the *in vitro* oscillator successfully captures
160 the essential feature of seasonal entrainment we observed *in vivo*: linear scaling of entrained
161 phase with an intermediate slope.

162 In the cell, the Kai proteins interact with histidine kinases and a network of other factors
163 absent from the reconstituted system, ultimately leading to rhythms in transcription across the
164 genome, including the *kai* genes themselves (21–23). These additional factors may account for
165 the differences we observe between proportionality constants *in vitro* and *in vivo*, and the time
166 delay between KaiC phosphorylation and luminescent output of the *kaiBC* expression reporter is
167 likely responsible for the offset in Fig. 2C. While these considerations suggest that care must be
168 taken in connecting the *in vitro* and *in vivo* results, they also underscore the significance of our
169 observation that the Kai oscillator proteins by themselves are sufficient to yield the linear
170 response of the system to altered day length. We therefore sought to use this *in vitro* model of
171 seasonality to uncover the biochemical basis of the linear seasonal clock response.
172
173 **Seasonal adaptation of the circadian oscillator can be decomposed into step responses to**
174 **individual metabolic cues.**
175
176 In the purified system, the entraining cues are steps between high and low ATP/ADP that
177 simulate dawn and dusk. We therefore sought to decompose the seasonal adaptation of the clock
178 into step responses following each metabolic transition. This approach is related to the limit
179 cycle theory of oscillators: if we assume that a unique stable orbit exists for both the day and
180 night conditions, then a metabolic transition forces the system to adjust from its current cycle to
181 one associated with the new condition. If relaxation to the new orbit occurs rapidly relative to the
182 length of the day—that is, if the light and dark orbits are strongly attracting—then the state of the
183 oscillator at each transition can be specified simply by a phase angle on that orbit. In this limit,
184 the response of the system is fully determined by instantaneous phase shifts caused by the

185 transitions. Mathematically, we describe this limit as an oscillator comprised of a single phase
186 variable, θ, that runs along a fixed limit cycle trajectory at constant speed (see Mathematical
187 Appendix). The responses to dark-to-light or light-to-dark transitions are then represented by
188 phase shifts that are specified by the functions $L(\theta)$ and $D(\theta)$, respectively.

189 To determine whether this fast-relaxation approximation can describe phase shifts in the
190 core Kai oscillator, and to study their biochemical basis, we measured the $L(\theta)$ and $D(\theta)$ shift
191 functions in our reconstituted system. To measure the $D(\theta)$ function, we incubated the Kai
192 proteins in daytime buffer, then transferred them into nighttime buffer at various times
193 throughout the circadian cycle and studied how the oscillation was affected. As previously, we
194 assayed oscillator response in separate experiments using either SDS-PAGE to measure KaiC
195 phosphorylation or the fluorescence polarization probe to achieve high temporal resolution;
196 example time series from the fluorescence polarization measurements are shown in Fig. 3A-B.

197 We proceeded to calculate phase shifts from these measurements, taking into
198 consideration that a switch to nighttime buffer conditions could affect the oscillator in two ways:
199 the phase of the oscillation can shift, and the oscillator period may change, both of which can
200 change the relative timing of peaks. In order to separate these effects, it is necessary to collect
201 enough data to accurately determine the period, and then extrapolate backwards to infer the
202 instantaneous phase shift at the time of buffer exchange. We detail our procedure for analyzing
203 these data to extract phase shifts in Figure 3—figure supplement 1. We used an analogous design
204 to measure the reverse steps from nighttime to daytime buffer (Fig. 3B). Plotted together in
205 Figure 3C-D, the extrapolated phase shifts measure the sensitivity of the clock to individual light
206 and dark steps throughout the 24-hour day.

The measured $L(\theta)$ and $D(\theta)$ step-response functions show that the phase of the purified KaiABC oscillator is responsive to both step-up and step-down metabolic changes. For example, a day-to-night shift lengthens the period of the clock by about 2 hours, and, when it is applied at subjective morning, leads to an instantaneous phase delay of about 3 hours (Figure 3—figure supplement 1). On the other hand, a night-to-day transition in the middle of subjective night shortens the period and causes a phase advance of about 1.5 hours.

These measurements characterize how the oscillator responds to a metabolic step-change throughout the entire clock cycle. However, when the clock is stably synchronized to a cycling environment, dawn and dusk fall only in a limited window of clock phases. To determine this window, we returned to our measurements in Figure 2C. We identified phases that correspond to dawn or dusk in entrained conditions mimicking LD 6:18 to LD 18:6 and marked these phases on the $L(\theta)$ and $D(\theta)$ functions (Fig. 3C-D, colored arrows). These points fell on gradually changing, approximately linear, regions of both curves, spanning roughly 6-hour windows near subjective dawn (for $L(\theta)$) and subjective dusk (for $D(\theta)$). Because these regions of $L(\theta)$ and $D(\theta)$ represent phase shifts comparable in magnitude but opposite in sign, we hypothesized that their opposing forces could enable oscillator entrainment to light-dark cycles.

To check this hypothesis, we simulated a simple (phase-only) oscillator that runs at constant frequencies in the light and dark and adjusts its phase in response to dawn and dusk according to the phase shift functions that we measured in Fig. 3C-D (see Computational Methods). This model essentially maps the one-dimensional phase variable from one cycle to the next according to $L(\theta)$ and $D(\theta)$. We analyzed the stability properties of this map and found that the oscillator could entrain with a unique phase to driving periods of within 4-5 hours of its

229 natural circadian period. Outside this range, the oscillator failed to entrain or exhibited more
230 complex dynamics (Figure 3—figure supplement 2).

231 We proceeded to test whether the measured $L(\theta)$ and $D(\theta)$ step-response functions could
232 successfully reproduce the entrainment of the oscillator to repeated 24-hour metabolic cycles of
233 varying day length, shown in Figure 2. When subjected to light-dark cycles in simulations, the
234 oscillator model stably entrains to the diurnal schedule within two-to-five cycles (Fig. 4A-B, Fig.
235 4—figure supplement 1A). Importantly, the simulated entrained phase scales linearly with day
236 length with a slope similar to the experimental data, indicating that the driven clock response can
237 indeed be decomposed into a series of step responses to environmental transitions (Fig. 4C, Fig.
238 4—figure supplement 1B).

239 As mentioned above, we also measured $L(\theta)$ and $D(\theta)$ step-response functions with a
240 separate preparation of Kai proteins using a gel-based assay to read out the phase of the KaiC
241 phosphorylation rhythm (Figure 3E-F). Though the absolute magnitude of the step responses in
242 these measurements was larger, they still predict linear scaling of entrained phase in simulations
243 for day lengths between 6 and 14 hours (Fig. 4—figure supplement 2B). The discrepancy in
244 magnitude between these measurements may point to differences in sensitivity to input cues
245 between different preparations of Kai proteins, or to a slight perturbative effect of fluorescently
246 labeled KaiB.

247 We found that simulated entrainment of the phase oscillator model was particularly
248 sensitive to the regions surrounding subjective dusk (on $D(\theta)$) and subjective dawn (on $L(\theta)$)
249 (Fig. 3E-F, *colored arrows*), which were only sampled with small numbers of points. Because
250 the fluorescence polarization approach allows us to measure many conditions in an automated
251 way over many days, and thus to disentangle phase shifts from period differences (Fig. 3C-D,

Figure 3—figure supplement 1), these higher time resolution measurements better constrain the portions of the response functions critical for entrainment.

Given the observation that oscillator entrainment was sensitive to local shapes of $L(\theta)$ and $D(\theta)$, we wondered if midday tracking required a specific form of these response functions or if certain generic features are enough to account for midday tracking. Based on our observation that $L(\theta)$ and $D(\theta)$ in the KaiABC system are approximately linear in the regions used during metabolic entrainment, we asked whether linear $L(\theta)$ and $D(\theta)$ were sufficient to result in a linear dependence of clock phase on day length.

Linear regions of step-response functions underlie proportional tracking of day length.

Consider a phase oscillator driven by light-dark cycles of period T and day length τ (Eq. 1). When the oscillator is entrained (phase-locked) to the light-dark cycle, the oscillator returns to the same state by the end of a full cycle. Starting from an initial phase θ_0, the clock accumulates phase $\omega_L\tau$ during the day, then experiences a phase shift of magnitude $D(\theta_\tau)$ at dusk, accumulates phase $\omega_D(T-\tau)$ at night, and finally responds to dawn with a phase shift $L(\theta_T)$:

$$\theta_T = \theta_0 + \omega_L\tau + D(\theta_\tau) + \omega_D(T-\tau) + L(\theta_T), \qquad \text{(Eq. 1)}$$

where all angles are measured in units of cycles (1 cyc $= 2\pi$), and ω_L and ω_D are the oscillator frequencies in the light and dark, respectively. For stable entrainment, the effects of $L(\theta)$ at

dawn and $D(\theta)$ at dusk must balance the phase accumulated by the oscillator, so that the phase returns to the same point at the end of each cycle.

This expression for the entrained clock phase scales linearly with day length if its derivative with respect to τ is constant. The simplest way to achieve this condition is if $L(\theta)$ and $D(\theta)$ are themselves linear functions of θ, such that $D(\theta) \approx -d(\theta - \theta_D)$ and $L(\theta) \approx -l(\theta - \theta_L)$ over the relevant range of clock times. If oscillator frequency is the same in light and dark, as is approximately true for the Kai oscillator ($\omega_D/\omega_L = 0.93 \pm 0.01$, see Computational Methods), the peak time of the oscillation (measured in hours after dawn) can be expressed as $t_{pk} = m\tau + C$, with the slope $m(l, d) = d(1 - l)/(d + l - ld)$ determined by the slopes of the linear $L(\theta)$ and $D(\theta)$ functions. If the day and night oscillator frequencies differ, we still obtain a linear dependence on day length, but with an altered expression for the proportionality constant *m* (see Mathematical Appendix). This expression for *m* imposes constraints on values of *l* and *d* required for an oscillator to track different portions of the day-night cycle. Figure 4—figure supplement 3 highlights such requirements on *l* and *d* for a midday-tracking clock.

To determine whether $L(\theta)$ and $D(\theta)$ for the Kai oscillator are in line with this mathematical requirement, we examined the linear portions of the step-response functions in Fig. 3C-D. Indeed, the slopes of $L(\theta)$ and $D(\theta)$ from the fluorescence polarization assay ($l = 0.34 \pm 0.03$, $d = 0.38 \pm 0.05$) predict an *m* value consistent with our measurements of the entrained *in vitro* oscillator using the same method ($m(l, d) = 0.34 \pm 0.04$, calculated in the linear model vs. $m = 0.38 \pm 0.07$, measured) (Figure 4—figure supplement 3).

Because $L(\theta)$ and $D(\theta)$ are periodic functions on a circle, they cannot be linear everywhere with non-integer slope. However, maintaining the linear scaling of phase with day

length only requires that both $L(\theta)$ and $D(\theta)$ be linear over the range of clock times when dawn and dusk occur, respectively, with the nonlinearities required to satisfy periodicity appearing at other times. The exact width of the linear region of $L(\theta)$ and $D(\theta)$ depends on m and the range of day lengths that the oscillator is required to track. For example, an oscillator capable of tracking midday (m=0.5) over a 12-hour range of day lengths requires that $L(\theta)$ and $D(\theta)$ be linear over at least one quarter of the cycle. This criterion is met by the measured $L(\theta)$ and $D(\theta)$ (Fig. 3C-D).

To further test whether entrainment of the Kai system can be described by this framework, we returned to our phase oscillator simulations (Fig. 4C). When we replaced our experimentally measured $L(\theta)$ and $D(\theta)$ functions with linear approximations, the simulated oscillator exhibited a similar scaling of entrained phase over a wide range of day lengths (Fig. 4—figure supplement 2A-B). The linear approximations work because the regions where the step response functions deviate strongly from linearity are avoided in our entrainment simulations (Fig. 4—figure supplement 2C).

Together, these results indicate that the driven behavior of the cyanobacterial circadian clock in 24-hour cycles can be approximated as a simple oscillator that shifts in response to light-dark transitions with a sensitivity that varies linearly with phase. To test whether this linear mathematical framework holds more generally and to understand how the cyanobacterial clock responds to a broader range of environments, we sought to measure clock response to a variety of external conditions with both single and repeated light-dark transitions.

The behavior of the driven circadian clock across diverse conditions can be collapsed to a simple mathematical representation.

The phase oscillator model described above was inspired by the observation of linear scaling of clock phase in 24-hour days with various day lengths. The key model assumptions are (i) a unique clock cycle in the light and in the dark, (ii) rapid relaxation from one cycle to another when conditions change, and (iii) sensitivity to environmental changes that varies linearly with clock time. While these assumptions hold, the model should be capable of describing the behavior of a biological clock in arbitrary fluctuating environments. For example, the response to a single dark pulse can be decomposed into sequential step-down and step-up responses.

To test the range of validity of this mathematical model, we used our LED array system (Fig. 1A) to collect data on *S. elongatus* clock function in response to dark pulses administered at different clock times. This corresponds to a classical phase response curve analysis, a commonly used tool in circadian biology for characterizing the response of a biological clock to perturbations. We also probed clock responses to dark pulses of varying lengths (a so-called "wedge" analysis), and to repeated light-dark cycles with periods different from 24 hours. Our phase oscillator model predicts that the quantitative response to these various perturbations should all be related through the step-up and step-down functions (see Mathematical Appendix). One specific prediction of the model is that changing the time at which a dark pulse begins and the duration of a dark pulse should have separable linear effects on the oscillator, which would manifest as linear curves in phase response and wedge analyses. These experimental data and a fit of our linear model to the results are presented in Figure 5. The lines of best fit in Fig. 5A-C were obtained from a single global fit to all of the datasets, with two fitting parameters underlying the slopes of the regression lines across all conditions (Mathematical Appendix). The

337 overall agreement between the model and data suggest that limited data on clock response can be
338 successfully extrapolated to other conditions using this approach.

339 To understand the implications of these results, consider the phase response curve (PRC)
340 for a 12-hour dark pulse (Fig. 5A). Though phase response analyses frequently separate PRCs
341 into regions of low sensitivity to perturbation ("dead zones") followed by highly nonlinear
342 regions with large phase shifts, our model suggests a different interpretation (18, 24–26). Clock
343 response is weakest at times when nightfall is expected (t = 36 and 60 hours) and increases
344 gradually with clock time. The slowly changing regions of the PRC are well described by line
345 segments with the same slope, in agreement with our model based on linear step-response
346 functions $L(\theta)$ and $D(\theta)$. The "breakpoint" in the PRC near 50 hours is a consequence of the
347 fact that these periodic step-response functions cannot be linear everywhere with non-integer
348 slope, as discussed earlier.

349 In other words, a circadian clock capable of tracking midday over a wide range of day
350 lengths is expected to have a PRC that is approximately linear over many hours except for a
351 narrow region of rapid change that is required to satisfy periodicity. Indeed, in simulations where
352 $L(\theta)$ and $D(\theta)$ are linear everywhere except for a discontinuous jump, the PRC for a long dark
353 pulse appears as a straight line except for a single breakpoint (Fig. 5—figure supplement 1).
354 Near the breakpoint, small changes in the timing of darkness result in large differences in phase
355 shifts, and we would expect to find this region of the PRC at a clock time when such a
356 perturbation is least likely to occur naturally. In the dark-pulse PRC for *S. elongatus*, the
357 breakpoint near 50 hours occurs when prolonged darkness is improbable (Fig. 5A). The maximal
358 phase shift in a PRC can be a useful tool to characterize clock mutants, but our analysis

359 highlights that these regions are unlikely to be experienced in natural conditions and may exist
360 only as consequences of periodicity constraints.
361
362 **A geometric interpretation of oscillator response to varying day length.**
363
364 Finally, we asked how step response functions with linearly increasing sensitivity are related to
365 the mathematical structure of the oscillator and ultimately to the underlying molecular
366 mechanism. Do step response functions with these properties arise generically, or do they require
367 fine-tuned choices of parameters? To address these issues, we considered the simplest possible
368 dynamical representation that allows for distinct day and night clock cycles. In this model, the
369 clock cycle during the day is represented by a circular limit cycle with unit radius, and the clock
370 time is defined by the angular coordinate of the oscillator on this limit cycle (Fig. 6A). The effect
371 of darkness is to deform the limit cycle, transforming the daytime orbit to a nighttime orbit. For
372 simplicity, we assume this night cycle lies in the same plane as the day cycle and is also circular,
373 but may be offset relative to the day cycle and have a distinct radius (Fig. 6A).
374 After a transition from one condition to the other, the system state must evolve to the new
375 limit cycle. We suppose that each cycle is very strongly radially attracting. That is, when the
376 system is in a state off the limit cycle, it is rapidly pulled to the closest point on the cycle. Under
377 these conditions, the step transitions from one cycle to another are determined purely by
378 geometry (Fig. 6A), and we can connect this picture with the phase-only description we used to
379 analyze the experimental data. Here, linearly increasing sensitivity of a step response has a
380 simple geometric interpretation: when the two cycles are displaced from each other, a step
381 transition maps an arc of one cycle onto an arc of the other cycle that subtends a smaller angle

than the original (Fig. 6B). Thus, step transitions compress or expand angular distance when mapping one circle onto another. The slopes of the step response functions are thus given by the compression factor in this mapping (Fig. 6C-D, Figure 6—figure supplement 1; see Mathematical Appendix).

To determine how the entrained clock phase depends on geometry in this model, we simulated step transitions and then calculated the slope m of clock phase versus day length (Fig. 6E). This calculation indicates that midday tracking ($m \approx 0.5$) requires that the separation between the light and dark cycles is comparable to the radius of the cycle ($R \approx X$). This requirement can be understood intuitively by considering three cases where orbits have the same center-to-center separation ($\log X = 0.5$) but different sizes (Figure 6—figure supplement 1). Dusk transitions are strongly resetting for this choice of X, but the strength of dawn resetting varies with the relative size of the orbits. Dawn-tracking entrainment results when the night orbit is much smaller than the day orbit ($l \approx 1$) and dusk-tracking entrainment results when the night orbit is much larger ($l \approx 0$, $d \approx 1$), in accord with how m varies as a function of l and d (Figure 4—figure supplement 3). When the size of both orbits is similar to their center separation, the oscillator can track intermediate phases, such as midday.

Though this model makes a simple connection between attractor geometry and entrainment, it also makes a number of simplifying assumptions about oscillator dynamics that may not hold true for real biological clocks, such as instant transitions between cycles, perfectly circular orbits and constant angular frequencies along each cycle. To test the consequences of relaxing these assumptions, we used a dynamical model where the evolution of the system is described explicitly (see Computational Methods). Our simulations in Figure 6—figure supplement 2 show that in these more complicated scenarios the geometric arrangement of day

405 and night cycles remains a key determinant of the slope of entrained clock phase as a function of
406 day length. Indeed, in all cases we studied, midday tracking was only possible for geometries
407 where the center-to-center distance between the day and night cycles was comparable to the
408 radius of the larger orbit ($R \approx X > 1$).

409 This dynamical systems perspective allows us to reframe conditions on the underlying
410 biochemical mechanisms that can produce the observed midday tracking behavior. Changes in
411 the external environment caused by transitions between night and day should affect the oscillator
412 in such a way that the period remains close to 24 hours, but that the limit cycle is shifted by an
413 amount comparable to its radius. The relative geometry of the two limit cycles, which is
414 determined by the mechanisms that couple the environment to the clock, must be fine-tuned to
415 give a specific slope for the entrained phase. Indeed, when we plotted experimentally determined
416 orbits of the purified KaiABC oscillator on axes showing the extent of phosphorylation of two
417 key sites, we observed an arrangement similar to the expected geometry ($R \approx X$) using nucleotide
418 conditions that simulate either day or night (Fig. 6F) (6, 17).

419

420 **DISCUSSION**

421

422 Though circadian clocks are defined in part by their ability to continue to cycle in constant
423 environments, the defects associated with clock mutants are often most apparent when organisms
424 are faced with fluctuating environments (27–31). Thus, an important challenge is to understand
425 how biological clocks respond to the cycling environments found in nature, and how they
426 function to appropriately schedule gene expression and behavior.

For most organisms, there is an asymmetry between day and night, in terms of food availability, predation risk, etc., so that the need to carry out certain activities diurnally or nocturnally presents changing demands as the length of the day varies throughout the year. The situation is especially dramatic for cyanobacteria because there is an extreme metabolic contrast between day and night. We found that *S. elongatus* contends with these challenges using a clock that tracks the middle of the day.

The ability of circadian systems to keep track of the phase of the light-dark cycle has been long recognized in plants, insects, rodents and higher mammals (1, 32–36). Though molecular mechanisms that give rise to these entrainment behaviors are still being uncovered, analysis of circadian clock models has found that the presence of multiple feedback loops in complex clocks determines the number of points in the driving cycle that the oscillator can track simultaneously, by allowing different internal phase relationships between the clock components (37). For example, the multi-feedback loop clocks in plants are able to track phases of both dawn and dusk (33).

Consistent with this picture, we find that the core circadian oscillator in cyanobacteria, which relies on a single posttranslational feedback loop, keeps track of a single phase—the midpoint of the day portion of the cycle, a property described in our mathematical framework as a linear scaling of entrained phase with day length with slope $m \approx 0.5$. Why might keeping track of midday be useful for a photosynthetic organism with a simple clock? Clock-controlled gene expression in *S. elongatus* tends to be bimodal, with most genes falling into subjective dawn or dusk classes. Because the biosynthetic capacity of *S. elongatus* is severely limited in darkness, the midday tracking effect we describe here could be a mechanism to ensure that biosynthetic resources are partitioned in a balanced way between the dawn and dusk genes, even as the day

450 length changes with the seasons (Fig. 6—figure supplement 3). In particular, clock-driven
451 transcription in this organism has been shown to implement a switch between anabolic and
452 catabolic carbon metabolism, suggesting that a role for the midday tracking we observe here is to
453 ensure balanced growth by timing this switch appropriately in days of different length (38).

454 The ability to reconstitute this effect *in vitro* by delivering metabolic pulses to the
455 purified Kai proteins indicates that midday tracking is not necessarily achieved through
456 additional feedback mechanisms in the cell, but appears to be a property of the clock proteins
457 themselves. The purified clock responds to metabolic steps with phase shifts that are linear
458 functions of the previous phase. The slopes of these response functions are presumably tuned to
459 give an appropriately entrained clock phase. Notably, linear responses have also been observed
460 for the Kai oscillator following temperature steps, suggesting that this is a general reaction of the
461 system to inputs (39).

462 The mathematical framework that we describe here has deep similarities to the theory of
463 nonparametric entrainment developed by Colin Pittendrigh (40–42). His work motivated a theory
464 of entrainment to diurnal cycles mediated by instantaneous phase shifts at dawn and dusk, which
465 can be summarized by a phase response curve. Daan and Pittendrigh suggested that the ability of
466 the clock to track specific phases of the day-night cycle in different seasons depends on the shape
467 of the phase response curve as well as the difference between the free-running period of the
468 clock and the period of the day-night cycle (40, 43). Our decomposition of driven behavior of the
469 KaiABC oscillator into individual step responses is in the spirit of this classic paradigm.

470 We note that a mismatch between the free-running clock period and the external cycle is
471 not required for stable entrainment in our phase oscillator model (see Mathematical Appendix).
472 Instead entrainment can be achieved from the opposing effects of the step-up and step-down

473 phase shifts, which occur at different clock times in days of different length. The step-response
474 curves underlying entrainment in our model are nonlinear functions of clock phase, but they can
475 be successfully approximated by linear functions over the interval of clock phases used during
476 entrainment. Our simulations suggest that the slopes of these locally linear functions are key
477 determinants of entrained phase, along with changes in clock period in daytime and nighttime
478 conditions. Successful prediction of how the *in vitro* oscillator entrains to rhythmic environments
479 is due in large part to the ability to map out the step-response curves with high temporal
480 resolution. In this study, we achieve this by measuring free-running oscillations in an automated
481 way using the fluorescence polarization probe.

482 Though there are likely other effects at play in natural environments, as long as the
483 system can be described by fast relaxation back to distinct limit cycles in day and night,
484 instantaneous step-response descriptions of the kind used here should be applicable. The data
485 reduction achieved in our linear model holds the promise of predicting the behavior of the
486 circadian rhythms in many time-varying environments from a minimal data set that characterizes
487 oscillator response, and may be applicable to clocks in many organisms.

488 Though the biochemistry of even the simplest circadian clock is complex, our analysis
489 suggests that a key determinant of entrained behavior is how the clock limit cycle is deformed by
490 coupling to the environment. Viewed in this way, the entrainment properties of circadian
491 oscillators arise from simple features of the geometry of the limit cycle attractor that could be
492 measured in any organism. The concept that the phase-shifting of oscillators can be studied in
493 terms of their geometric properties was initially developed by Winfree (44). In this context, it
494 would be informative to analyze the geometric arrangement of day and night limit cycles of
495 clock gene transcripts in other species. An important goal for the future is to understand how the

496 biochemical properties of the clock components in cyanobacteria and other organisms achieve
497 the effect of shifting the limit cycle without changing the period, allowing us to use dynamical
498 systems theory to bridge the gap between molecular detail and systems-level clock phenotypes.
499

500 **ACKNOWLEDGMENTS**

501 We thank Arvind Murugan and members of the Rust and Dinner labs, particularly H. Gudjonson
502 and G. Pattanayak, for feedback and useful discussions. Joel Heisler and Andy LiWang assisted
503 us with fluorescence polarization measurements. This work was supported by NIH Training
504 Grant 5T32EB009412 (E.L.), NIH Training Grant T32GM07197 (U.L.), NIH R01 GM107369-
505 01 (to M.J.R.), NSF PHY-1305542 (to A.R.D.), a Pew Biomedical Scholarship (to M.J.R.). E.L,
506 J.L, H.Y., and U.L. carried out experiments. E.L. analyzed data. E.L., A.R.D. and M.J.R.
507 designed the study, performed mathematical modeling, and wrote the paper.
508

509 **MATERIALS AND METHODS**

510

511 **EXPERIMENTAL METHODS**

512 **Cyanobacterial strains and culture conditions.** Two strains of *Synechococcus elongatus* PCC
513 7942 were used for this study. AMC1300 is a wild-type derivative carrying a bacterial luciferase
514 bioluminescent reporter of *kaiBC* expression. AMC1300 carries *PkaiBC::luxAB* at NS1 and
515 *PpsbAI::luxCDE* at NS2, which enables the cells to produce the luciferase enzyme and the long-
516 chain aldehyde substrate for the luminescent reaction (45). AMC408 carries a *purF* reporter
517 (*PpurF::luxAB* at NS2*, PpsbAI:luxCDE* at NS1) (46). Prior to experimental measurements, all

518 cultures were grown in test tubes in BG11M liquid medium at 30 °C with shaking under cool
519 white fluorescent bulbs (≈60 μmol photons m^{-2} s^{-1}, Philips AltoII).
520
521 **Creating custom light-dark environments using LED arrays.** To simulate different light-dark
522 cycles, we used custom-built red LED arrays in a 96-well format (LEDs from
523 superbrightleds.com, cat. no. RL5-R12008; 96-well plates from Corning, cat. no. 3916). The
524 LEDs were mounted into a hollowed-out 96-well plate and the tails of the LEDs were soldered
525 into a circuit board, where they were wired in parallel in groups of four to the analog inputs of an
526 Arduino Mega 2560 microcontroller. Another hollow 96-well plate was glued to the bottom of
527 the LED-carrying plate, beneath the LEDs, in order to create a light baffle and prevent light
528 leakage between the wells. These devices were placed ≈2 mm above a black 96-well plate
529 containing cells growing on BG11-agar, such that every well of the growth plate received
530 illumination from a single LED (≈1.8 cm between LED and agar surface). The growing plate
531 was sealed with transparent film, with holes punctured above each well to provide aeration.
532 Custom Arduino scripts were written to administer appropriate light-dark schedules to cells in
533 the growth plates. Every well received the same light intensity (1.8 V across each LED, ≈200
534 μmol photons m^{-2} s^{-1}) in the light portion of the day. The temperature of the agar was 31.6 ± 0.8
535 °C underneath LEDs that were turned on and 28.9 ± 0.3 °C under LEDs that were off (mean ±
536 standard deviation of 6-10 wells).
537
538 **Monitoring gene expression *in vivo* using bioluminescent reporters.** Cells were grown in test
539 tubes until OD 0.5-0.8, as described above, and diluted to OD 0.2 immediately prior to
540 experiment. A black 96-well plate was filled (200 μL/well) with BG11M-agar (15 g/L agar)

541 supplemented with sodium thiosulfate (1 mM) and HEPES (20 mM, pH 8.0). When the BG11M-
542 agar mixture cooled to room temperature, 35 μL of cells from growing culture at OD 0.2 were
543 added to each well of the plate. The plate was sealed with transparent UniSeal (GE HealthCare
544 Life Sciences cat no. 7704-0001), holes were punched above each well using 26G½ needle (BD
545 Falcon, cat. no. 305111), and the plate was placed underneath an LED array. Bioluminescence
546 from luciferase reporters was measured every 30 minutes using a TopCount scintillation counter
547 (PerkinElmer, IL). Each well of a 96-well plate was read for 1 second per measurement.
548
549 **KaiABC *in vitro* reactions.** KaiA, KaiB and KaiC were recombinantly expressed and purified as
550 previously described (47), though the anion exchange chromatography purification step was
551 omitted in the preparation of KaiC used for fluorescence polarization experiments. Protein
552 concentration was measured via Bradford Assay Kit (Promega). For experiments relying on
553 SDS-PAGE analysis of KaiC phosphorylation, KaiABC proteins were mixed in master reaction
554 buffer (20 mM Tris [pH 8], 150 mM NaCl, 5 mM $MgCl_2$, 10% glycerol, 0.5 mM EDTA)
555 supplemented with a mixture of ATP and ADP (day buffer: 2 mM ATP, night buffer: 2 mM
556 ATP, 7.5 mM ADP). All reactions were incubated at 31 °C. To mimic light-to-dark transitions,
557 ADP stock (400 mM, pH 7.5) was added to appropriate reactions to 7.5 mM final [ADP]. To
558 mimic dark-to-light transitions, the reactions were passed through Zeba desalting columns (7
559 MW kDa cutoff, ThermoFisher) equilibrated in day buffer. Because every buffer exchange step
560 dilutes the proteins by about 10%, the reactions were performed at 3× protein concentration (10.5
561 μM KaiB and KaiC, 4.5 μM KaiA). At every measured time point, 2 μL of reaction mixture was
562 removed from the reaction mixture and mixed with 4 μL of 1.5× SDS-PAGE sample buffer.

563 KaiC phosphorylation was assayed by SDS-PAGE and quantified by densitometry, as previously
564 described (17).
565 In the cases where oscillations were read out by monitoring fluorescence polarization,
566 KaiABC proteins were mixed at 3× standard protein concentration in the master reaction buffer
567 supplemented with a mixture of ATP and ADP (day buffer: 2.5 mM ATP, night buffer: 2.5 mM
568 ATP, 7.5 mM ADP). All reactions were incubated at 31 °C. Day-to-night transitions were
569 mimicked by addition of 7.5 mM ADP (final), and night-to-day transitions were mimicked by
570 passing the reactions through Zeba desalting columns twice.
571 For step-up perturbations shown in blue in Fig. 3D, buffer exchange steps were
572 administered every 2 hours over a 24-hour interval, and phase shifts were measured relative to an
573 unperturbed control reaction. For every other experiment in Fig. 3C-D, buffer exchange or ADP
574 addition steps were performed every 2 hours over a 12-hour interval on two out-of-phase
575 reactions, prepared as follows. A master mix containing proteins and appropriate nucleotides was
576 split into two tubes, which were flash-frozen in liquid nitrogen immediately after mixing and
577 stored at −80 °C. To prepare out-of-phase reactions, one of the two tubes was thawed in a 30 °C
578 water bath 12 hours later than the other.
579 After all buffer exchanges were completed, the reactions were supplemented with
580 fluorescently labeled KaiB (0.2 μM final) and transferred to the plate reader.
581
582 **Preparation and labeling of fluorescently tagged KaiB.** We introduced a K25C mutation in
583 KaiB using site-directed mutagenesis of the pMR0019 plasmid carrying 6xHis-PSP-KaiB^{WT}
584 construct in the pET47b(+) backbone. KaiB^{K25C} was expressed in BL-21 (DE3) *E. coli* by
585 overnight induction with IPTG at 18 °C and purified following the standard protocol (47).

586 Labeling with 6-iodoacetofluorescein (6-IAF) was performed as previously described (19) with
587 minor modifications. Briefly, 130 μL of $KaiB^{K25C}$ stock (50-100 μM) was buffer-exchanged into
588 labeling buffer (20mM Tris, 1 mM TCEP, pH 7.0 – 7.5) using a Zeba desalting column (7 MW
589 kDa cutoff). A freshly prepared solution of 6-IAF in DMSO was added to the protein solution in
590 10-fold molar excess, and the mixture was incubated overnight at 4 °C in the dark. The labeling
591 reaction was quenched by addition of DTT in approximately 10-fold molar excess relative to 6-
592 IAF. Unincorporated dye was removed through three rounds of 5-fold dilution in reaction buffer
593 and subsequent concentration using a centrifugal filter (10 kDa cutoff, Amicon, Millipore).
594 Concentration of final fluorescein-labeled $KaiB^{K25C}$ solution was determined by Bradford assay.
595
596 **Monitoring fluorescence polarization rhythms using labeled KaiB.** Oscillations in KaiABC
597 reaction mixtures supplemented with fluorescently labeled $KaiB^{K25C}$ (10.5 μM KaiB and KaiC,
598 4.5 μM KaiA, 0.2 μM KaiB-fluorescein) were monitored on an Infinite F500 plate reader
599 equipped with a fluorescence polarization module (Tecan Trading AG, Switzerland). At least 30
600 minutes prior to measurement, the built-in heating module was turned on to warm the instrument
601 and a black 384 well-plate (Greiner, cat. no. 781900) was loaded into the plate reader. For the
602 metabolic entrainment experiment shown in blue in Figure 2—figure supplement 1A and the
603 step-up experiment shown in blue in Figure 3D, the plate reader temperature was 28 °C; for all
604 other experiments, the plate reader temperature was 31 °C. Reactions were quickly transferred
605 onto the pre-warmed plate (20-35 μL/well) and 1-3 wells were filled with master reaction buffer.
606 The plate was sealed with a polyethylene silicone plate sealer (Nunc™, ThermoFisher cat. no.
607 235307) and returned to the instrument. Fluorescence polarization of wells of interest (exc. 485
608 nm, 20 nm bandpass; emm. 535 nm, 25 nm bandpass; dichroic 510 nm.) was read out every 15

609 minutes using a script created in iControl software (v. 1.12, Tecan Trading AG). Wells
610 containing reaction buffer only were used as blanks, and the G factor was calibrated such that a
611 solution of free fluorescein in reaction buffer produced a reading of ≈20 mP.
612
613 **Data analysis.** All oscillating trajectories were fit to sinusoids using optimization routines
614 written in MATLAB (Mathworks, Inc.) (RRID: SCR_001622). See Computational Methods for
615 detailed fitting procedures and descriptions of simulations. Computational pipelines used for
616 analysis and simulations have been deposited to GitHub at
617 https://github.com/euleip/Simulations_and_analysis_pipelines_github_repo (48).
618
619 **COMPUTATIONAL METHODS**
620
621 **Optimization and curve-fitting routines**
622 All nonlinear fitting procedures were written in MATLAB using the lsqnonlin() or nlinfit()
623 routines. Linear regressions were performed using the polyfit() function. Uncertainties around
624 the best-fit slopes were evaluated using standard formulas for linear regression with known
625 errors in dependent variables (49). For *in vivo* experiments, these errors were computed as
626 standard errors of the mean from replicate measurements; for *in vitro* measurements in Fig. 2, the
627 errors in fit phases were computed from the curvature of the cost function at the optimum using
628 the nlpredci() function in MATLAB. Where indicated, 95% confidence intervals were also
629 estimated by nlpredci().
630

631 **Normalization of bioluminescent reporter traces recorded in light-dark cycles or in**
632 **continuous light**
633
634 Prior to fitting, bioluminescence trajectories were normalized to zero mean and unit standard
635 deviation over the fitting interval, unless specified otherwise. In all analyses, we discarded data
636 from the first 2.5 hours after lights-on to avoid masking effects.
637
638 **Estimation of clock phase *in vivo* in light-dark cycles**
639
640 The bacterial luciferase reporter system that we use exhibits transient masking effects following
641 dark-to-light transitions. To overcome this issue in determining the phase of gene expression in
642 light-dark cycles of varied day length, we employed a drive-and-release strategy. In this
643 approach (illustrated for LD 8:16, LD 12:12 and LD 16:8 in Fig. 1A), cells were first entrained to
644 a given diurnal schedule and then released into constant light for several days to determine the
645 peak times of the entrained rhythm.
646 We relied on two approaches to calculate the peak times of normalized bioluminescence
647 trajectories recorded after release into constant light: (i) we fit sinusoids to 48-hour segments of
648 the trajectories in constant light, and (ii) we locally fit parabolas near the maxima of the
649 trajectories. The advantage of sinusoidal fitting is that it captures phase information for the entire
650 waveform; on the other hand, local parabolic fitting allows for a precise determination of the
651 time of an individual peak without influence from others. In practice, we found that the estimates
652 of the scaling between entrained phase and day length derived from the two approaches are in

653 good agreement with each other (Table 1, Figure 1—figure supplement 2). Fitting details are
654 described in the following two subsections.

655 Error bars in Fig. 1C, Fig. 1—figure supplement 2A, and Fig. 5 represent the standard
656 deviation of peak times calculated from technical replicates (n=4-8). Technical replicates refer to
657 measurements obtained from side-by-side cultures subjected to the same light-dark conditions. In
658 rare cases, cells in individual wells died or produced noisy bioluminescent signals or trajectories
659 that fit poorly to sinusoids or parabolas. We rejected trajectories as outliers from our analysis if
660 they produced fits with a squared error greater than 10 (0-13 outliers per 96 wells).

661

662 <u>(i) Estimation of period and peak times from sinusoidal regression</u>

663 Sinusoidal fits were performed by least-squares minimization of the cost function:

$$cost = \sum_{i=1}^{N} \left[y_i - \left(A \sin\left(\frac{2\pi x_i}{T} - \phi \right) + m x_i + C \right) \right]^2 ,$$

664 where y_i and x_i represent, respectively, the normalized bioluminescence signal and the time after
665 release into constant light for the i-th timepoint. The period in the fits was constrained to $23 < T$
666 < 25 hours. The best-fit period was distributed within these bounds, independent of the day
667 length of the preceding entraining cycle (Fig. 1—figure supplement 2D), a conclusion we
668 confirmed in a peak-to-peak analysis described below.

669 We considered whether the quality of sinusoidal fits affected the estimated slope m.
670 When we performed sinusoidal fits of the dataset in Fig. 1C, the least-squares errors, normalized
671 by degrees of freedom, were distributed between 0 and 1. If data from all of the wells were
672 included in the analysis, linear regression to this data yielded a slope of $m = 0.55 \pm 0.02$ (Table
673 1). As the table below shows, imposing stricter cutoffs on least-square fitting error did not

674 significantly impact the estimate of the slope, so an estimate of *m* based on all of the data is

675 reported in Table 1.

least-squares error threshold	*% wells satisfying*	*m ± SD of estimate*
1	100%	0.55 ± 0.02
0.5	90%	0.53 ± 0.01
0.1	45%	0.51 ± 0.03
0.05	17%	0.64 ± 0.03

676

677

678 <u>(ii) Estimation of period and peak times from local parabolic regression</u>

679 We found that certain bioluminescent trajectories were fit poorly by sinusoids. As Fig. 1—figure

680 supplement 3 shows, *purF* reporter waveforms display (a) strong asymmetry, marked by faster

681 rising and slower falling dynamics (e.g., second peak in τ = 18 hours curve), (b) wide peaks (e.g.,

682 first peak in τ = 8 hours curve), and (c) broad "shoulders" after the peak that occasionally give

683 rise to secondary peaks (e.g., first peak in τ = 18 hours curve). In some cases *kaiBC* reporter

684 trajectories also exhibited successive peaks with significantly different amplitudes. In Fig. 1C

685 and Fig. 1—figure supplement 3, we fit parabolas to 6-hour intervals around the peaks of

686 normalized bioluminescence trajectories and estimated phases from the first peak positions and

687 periods from the average peak-to-peak times (n=4-8). We verified that this peak-fitting

688 procedure produced comparable results to sinusoidal fitting for the *kaiBC* datasets in Fig. 1C and

689 Fig. 1—figure supplement 2 (see Table 1 and Fig. 1—figure supplement 2B-E).

690

691 **Comparison of waveforms during light-dark cycling and in continuous light**

692

693 To compare clock reporter dynamics during entrainment and in continuous light in Fig. 1—
694 figure supplement 1, we computed nonparametric correlations (Kendall's τ coefficient) between
695 the reporter signal (P_{kaiBC}*::luxAB*) measured during the "day" windows in light-dark cycles (days
696 1-5) and during the corresponding time interval after release into continuous light (day 6). For
697 example, in the case of LD 10:14, the normalized luminescence data recorded between 2.5 and
698 14 hours during each of the five entraining cycles were correlated with the luminescence
699 dynamics measured between 2.5 and 14 hours after release into constant light. The fact that we
700 observe Kendall's $\tau > 0.8$ after the second driving cycle suggests that cells are effectively
701 entrained within three cycles and that rhythms observed during the lights-on portion of a light-
702 dark cycle can be thought of as a fragment of a free-running rhythm.

703

704 **Estimation of clock phase *in vitro* in metabolic cycles**

705

706 For the %P-KaiC measurements in Fig. 2C, normalized KaiC phosphorylation time courses from
707 day 3 of each reaction were fit independently to sinusoids. Best-fit parameters were obtained by
708 minimizing the cost function:

$$cost = \sum_{i=1}^{N} \left[y_i - \left(A \sin\left(\frac{2\pi x_i}{T} - \phi \right) + C \right) \right]^2 ,$$

709 with the period T fixed at 24 hours to match the period of the imposed metabolic cycles.

710 For the fluorescence polarization experiments in Figure 2C, fluorescence polarization
711 dynamics were recorded for 48 hours after the last buffer exchange, normalized (to zero mean,

712 unit variance) and fit to sinusoids according to the expression above, with fits to all reactions
713 from the same experiment sharing a globally-fit period T.
714
715 **Fitting and error propagation analysis of step-response experiments**
716
717 Step-response experiments described in this section were performed a total of three times: once
718 using KaiC phosphorylation to read out clock phase and twice using the fluorescence
719 polarization reporter of KaiB-KaiC interaction. The phosphorylation measurements were made
720 using an independent preparation of proteins from the fluorescence polarization experiments.
721 We performed step-response experiments in Fig. 3 in order to determine whether the
722 behavior of the clock in metabolic cycles could be decomposed into a sum of phase shifts due to
723 individual clock transitions. To do so, we first needed (a) to extract L and D functions from step
724 response measurements, and then (b) to use these L and D functions in numerical simulations of
725 clock entrainment to light-dark cycles, as described in the main text and Mathematical Appendix.
726 In our experiments, we directly observed how the dynamics of the fluorescence
727 polarization reporter or KaiC phosphorylation changed as a function of lab time (e.g., Fig. 3A-
728 B), but for our downstream simulations and analysis (e.g., Fig. 4) these values had to be
729 converted to clock phase coordinates (e.g., Fig. 3C-D) consistent with how $L(\theta)$ and $D(\theta)$ are
730 defined. Specifically, we needed to (i) convert the lab time of each step to corresponding clock
731 phase θ (or clock time, CT), and then (ii) determine the phase of each fluorescence polarization
732 trace or KaiC phosphorylation trajectory after the perturbation in order to compute the phase
733 shift ($L(\theta)$ and $D(\theta)$) relative to an unperturbed control.
734 Though these conversions are straightforward in principle, it is important to note that

735 both (i) and (ii) rely on sinusoidal regression of phase from measured data, and that the best-fit
736 phases in both cases are only estimates of the true values. The corresponding uncertainty in the
737 best-fit parameters must be propagated through numerical simulations of entrainment.
738 Because the temporal resolutions of the KaiC phosphorylation and fluorescence
739 polarization measurements are very different (3 hours vs. 15 minutes, respectively), we expected
740 the sources of uncertainty in fitting these data to be different (see Figure 2—figure supplement
741 1), and we thus analyzed their errors in different ways. The sparse measurement of KaiC
742 phosphorylation dynamics leads to relatively high uncertainty in best-fit phase and period, and
743 we propagated the errors through our simulations using nonparametric bootstrapping of the
744 datasets. In the case of the fluorescence polarization measurements, experiment-to-experiment
745 variability is the major source of uncertainty. We therefore performed two replicate
746 measurements of *L* and *D* (Figure 3C-D) and used the four possible combinations of *L* and *D* in
747 entrainment simulations to assess the range of entrainment behavior constrained by our
748 measurements of these step-response measurements. We describe each of these approaches in
749 turn in the following two sections.
750
751 **Error propagation analysis of step-response experiments performed using the fluorescence**
752 **polarization reporter of KaiB-KaiC interaction**
753
754 Periods and phases of reactions in each set were determined by global sinusoidal fitting:
755 amplitude, offset and phase terms were fit independently for each reaction, but a single best-fit
756 period was shared among all fits in a given step-up or step-down set. To avoid transient effects
757 due to a metabolic pulse, only those data points which were collected at least 16 hours after a

758 step-up or step-down perturbation were used for fitting. Mathematically, we used a non-linear

759 least-squares optimization routine to minimize the cost functions:

$$cost_{day} = \sum_{r=1}^{N_{rxns}} \sum_{i=1}^{N_r} \left[y_{r,i} - \left(A_r sin\left(\frac{2\pi t_{r,i}}{T_{day}} - \phi_r \right) + C_r \right) \right]^2 \text{ (for reactions in day buffer)}$$

760 and

$$cost_{night} = \sum_{r=1}^{N_{rxns}} \sum_{i=1}^{N_r} \left[y_{r,i} - \left(A_r sin\left(\frac{2\pi t_{r,i}}{T_{night}} - \phi_r \right) + C_r \right) \right]^2 \text{ (for reactions in night buffer),}$$

761 where $y_{r,i}$ refers to the i-th data point in the r-th normalized fluorescence polarization trajectory,

762 $t_{r,i}$ refers to the lab time when that data point was collected, and N_r is the number of data points

763 fit in the r-th reaction. Here A_r, φ_r and C_r are the best-fit parameters for the r-th reaction; T_{day} and

764 T_{night} are best-fit periods for all reactions in the 100% ATP and 25% ATP datasets, respectively.

765 These best-fit parameters were used to determine the phase θ of each step perturbation

766 and corresponding phase shifts $L(\theta)$ and $D(\theta)$, analogously to the way described for the KaiC

767 phosphorylation datasets below. The step-response functions were interpolated linearly to

768 generate smooth curves while enforcing 2π-periodicity.

769 Linearized step-response functions $L_{lin}(\theta)$ and $D_{lin}(\theta)$ were prepared by linear regression

770 of $L(\theta)$ and $D(\theta)$ centered on the regions used during metabolic entrainment: D functions were

771 linearized between 6 and 22 CT hours; L functions were linearized between 18 and 34 CT hours

772 (see Fig. 3C-D). To satisfy periodicity, the step-response functions were assembled as piecewise-

773 linear functions with the same slope everywhere but with offsets every 2π radians at

774 "breakpoints," which were selected by manual inspection. See Figure 4—figure supplement 2C

775 for an illustration of $L(\theta)$ and $D(\theta)$ and the corresponding $L_{lin}(\theta)$ and $D_{lin}(\theta)$.

776 Finally, step phases deduced from polarization trajectories were adjusted to match the

phases of the KaiC phosphorylation rhythm. This conversion made use of measurements in Figure 2—figure supplement 1, which indicated that the phase of oscillation in KaiC phosphorylation lags behind the phase of the polarization reporter of KaiB-KaiC binding by approximately $2\pi/3$.

By performing this analysis for the two step-up and two step-down datasets in Figure 3C-D, we generated two sets of $\{L, L_{lin}, T_{day}, T_{night}\}$ and two sets of $\{D, D_{lin}, T_{day}, T_{night}\}$. The phase oscillator simulations described below require using the L and D functions together in each simulation. To propagate the experiment-to-experiment variability in step-response measurements through our simulations, we combined the two measurements of L and two measurements of D into the four possible combinations of $\{L, D\}$ pairs. This resulted in four sets of $\{L, L_{lin}, D, D_{lin}, T_{day}, T_{night}\}$, which were used in the simulations below.

The ratio of oscillator frequencies in dark and light, $\frac{\omega_D}{\omega_L} = \frac{T_{day}}{T_{night}} = 0.94 \pm 0.01$, was determined by averaging the values of T_{day} and T_{night} from the two step-up and two step-down sets above. Best estimates for the slopes l and d in Figure 4—figure supplement 3 were computed via the following bootstrap analysis. For each L and D function in Fig. 3C-D, we selected points from the regions used for linearization above (6-22 CT hours on D, 18-34 CT hours on L). We sampled these data points with replacement until we generated 500 samples containing at least 3 unique points. For each set of resampled points, we computed the slope of the best-fit line, for a total of 1000 samples of l and d. The crosshair in Figure 4—figure supplement 3 marks the average ± standard deviation of these values ($l = 0.34 \pm 0.03$, $d = 0.38 \pm 0.05$).

The phase oscillator model discussed in the main text and the Mathematical Appendix

799 makes the prediction that the proportionality constant *m* between entrained phase and day length

800 depends on *l* and *d* coefficients according to $m(l,d) = 1 - \frac{-(1-l)\times(\omega_D/\omega_L)}{d+l-ld} - \frac{1}{d+l-ld}$. To check

801 whether this prediction is in line with our experimental measurement of *m*, we used this formula

802 to calculate *m* for every pair of *l* and *d* samples generated in the bootstrapping procedure above,

803 assuming $\frac{\omega_D}{\omega_L} = 0.94$. According to this calculation, $m(l,d) = 0.34 \pm 0.04$ (mean ± standard

804 deviation of the distribution), which is in agreement with the experimental measurement in

805 Figure 2C ($m = 0.38 \pm 0.07$).

806

807 **Non-parametric bootstrapping of step-response datasets collected using SDS-PAGE**

808 **analysis of KaiC phosphorylation**

809

810 Recall that measuring each step-response function requires (i) conversion of the lab time of each

811 step to corresponding clock phase θ (or clock time, CT), and then (ii) determination of the phase

812 of each KaiC phosphorylation trajectory after the perturbation in order to compute the phase shift

813 ($L(\theta)$ and $D(\theta)$) relative to an unperturbed control. In particular, uncertainties in (i) manifest as *x*

814 errors on *L* and *D* in Fig. 3E-F; these errors are correlated across all points on the step-response

815 function. Uncertainties in (ii) manifest as *y* errors on *L* and *D*; these errors derive from the errors

816 in the phase estimates of both the control and step reactions. To propagate both of these sources

817 of error, we used the following non-parametric bootstrapping strategy.

818 First, KaiC phosphorylation dynamics from all step-response measurements were

819 assembled into a master dataset containing 9 step-up trajectories, 9 step-down trajectories, as

820 well as two control reactions. These measurements were performed once on an independent

821 preparation of proteins from the batch used to generate data in Fig. 3C-D. This master dataset
822 was then trimmed to include only data collected at least 16 hours after a step transition, and
823 every trajectory was normalized. To generate bootstrapped datasets, we sampled with
824 replacement from the entire master dataset (as opposed to resampling reactions individually)
825 1000 times.

826 Next, we used each resampled dataset to compute phase shifts in KaiC phosphorylation
827 due to step-up and step-down transitions; in other words, each bootstrapped dataset was used to
828 derive a bootstrapped pair of $L(\theta)$ and $D(\theta)$. For a given dataset, we globally fit all 100% ATP
829 trajectories (9 step-up trajectories, plus the 100% ATP control reaction) such that all fits shared a
830 best-fit period (T_{day}), but phase, amplitude and offset terms were fit independently for each
831 reaction, as described above for polarization datasets. Likewise, we fit all 20% ATP trajectories
832 (9 step-down reactions, plus the 20% ATP control reaction) to obtain a globally best-fit period
833 (T_{night}) and independently fit phases for every reaction.

834 $L(\theta)$ and $D(\theta)$ map the phase at which a metabolic step occurs to the resulting phase shift.
835 The phase at which the metabolic step occurred for every reaction r was computed from the best-
836 fit phase of the appropriate control reaction at step time $t_{r,step}$:

$$\theta_{r,step}^{control} = \frac{2\pi t_{r,step}}{T_{con}} - \phi_{con},$$

837 where ϕ_{con} is the best-fit phase of the control reaction and T_{con} is the globally-fit oscillator period
838 in the appropriate control condition (i.e., $T_{con} = T_{day}$ for step-down reactions, $T_{con} = T_{night}$ for step-
839 up reactions).

840 Similarly, we computed the apparent phase of each perturbed reaction at the time of each
841 step:

$$\theta_{r,step} = \frac{2\pi t_{r,step}}{T_{pert}} - \phi_r,$$

where ϕ_r is the best-fit phase of the r-th reaction and T_{pert} is the globally-fit oscillator period in the perturbed condition ($T_{pert} = T_{night}$ for step-down reactions, $T_{pert} = T_{day}$ for step-up reactions).

Finally, we defined the phase shift in response to each step perturbation as the difference in phase of the perturbed reaction and the appropriate unperturbed control.

$$L\left(\theta_{r,stepUp}^{control}\right) = \theta_{r,stepUp} - \theta_{r,stepUp}^{control}.$$

$$D\left(\theta_{r,stepDown}^{control}\right) = \theta_{r,stepDown} - \theta_{r,stepDown}^{control}.$$

To estimate phase shifts at other values of θ, we linearly interpolated L and D between the measured values while enforcing 2π-periodicity.

For each set of L and D generated in this way, we also prepared linearized versions L_{lin} and D_{lin}. Linear fits to L and D were performed over the range of step times similar to the ones we selected for fluorescence polarization-based step-response functions as discussed above (L between 18 and 33 CT hours, D between 6 and 23 CT hours). These regions of L and D were selected by visual inspection because they are centered on phases used by the KaiABC oscillator in diurnal cycles (i.e., see arrows in Fig. 3E-F) but also contain enough points (5-7) to avoid biasing the slope estimate by a single poorly fit data point.

We extrapolated the linear approximations to L and D over the entire cycle, with a single breakpoint away from the linear region to satisfy 2π-periodicity. Breakpoints were selected by visual inspection. While interpolating between data points near the breakpoint, we assumed that L and D (or L_{lin} and D_{lin}) never generate phase shifts larger than one cycle (i.e., winding number of 0). We anticipate that this choice does not significantly affect entrained phase in most of our simulations because the regions of L and D near the breakpoint are rarely used by the oscillator

during entrainment when $\tau < 14$ hours.

We repeated this procedure for each of the 1000 bootstrapped datasets, thereby generating 1000 sets of $\{L, D, L_{lin}$ and $D_{lin}, T_{day}, T_{night}\}$ that were used for subsequent analysis. Fig. 3E-F shows the mean ± standard deviation of the distribution of bootstrapped L and D generated this way.

Simulations of a phase oscillator driven by a light-dark cycle

We simulated entrainment to a step-like driving cycle for a phase oscillator governed by the four combinations of $\{L, L_{lin}, D, D_{lin}, T_{day}, T_{night}\}$ determined from the fluorescence polarization assays and the 1000 bootstrapped sets of $\{L, D, L_{lin}$ and $D_{lin}, T_{day}, T_{night}\}$ derived from KaiC phosphorylation measurements. Electing to work in units of cycles (1 cycle = 2π rad), we defined a phase variable $\hat{\theta} = \frac{\theta - \pi/2}{2\pi}$, such that $\hat{\theta} = 0$ cycles and $\hat{\theta} = 1$ cycles correspond to the trough of the KaiC phosphorylation trajectory and $\hat{\theta} = 0.5$ cycles corresponds to the peak. Where circadian time (CT) is mentioned in the text, we have adopted the convention that CT = 0 and 24 hours refer to $\hat{\theta} = 0$ and 1 cycles, respectively; CT = 12 hours refers to $\hat{\theta} = 0.5$ cycles. We also defined corresponding analogs of L and D in units of cycles:

$$\hat{\theta} = \frac{\theta - \pi/2}{2\pi}$$
$$\hat{L}(\hat{\theta}) = \frac{L(\theta)}{2\pi}$$
$$\hat{D}(\hat{\theta}) = \frac{D(\theta)}{2\pi}$$

See Figure 4—figure supplement 2C for examples of $\hat{L}, \hat{D}, \hat{L}_{lin}$ and $\hat{D}_{lin}$. For each set of $\{\hat{L}, \hat{D}, \hat{L}_{lin}, \hat{D}_{lin}, T_{day}, T_{night}\}$ generated in this way, we modeled oscillator entrainment to a driving cycle. As shown schematically in Fig. 4A and the Mathematical Appendix, oscillator

881 phase increases with constant angular velocity (given by $\omega_L = \frac{1}{T_{day}}$ during the day and $\omega_D =$

882 $\frac{1}{T_{night}}$ during the night); at dawn and dusk, oscillator phase shifts instantaneously according to $\hat{L}$

883 and $\hat{D}$, respectively. Therefore, oscillator phases at dusk and dawn of the *n*-th entraining cycle

884 can be computed iteratively:

$$\hat{\theta}_n^{dawn} = \hat{\theta}_{n-1}^{dusk} + \hat{D}\left(\mathrm{mod}(\hat{\theta}_{n-1}^{dusk}, 1)\right) + \frac{T-\tau}{T_{night}}$$

$$\hat{\theta}_n^{dusk} = \hat{\theta}_n^{dawn} + \hat{L}\left(\mathrm{mod}(\hat{\theta}_n^{dawn}, 1)\right) + \frac{\tau}{T_{day}}$$

885 We simulated oscillator behavior in 24-hour light-dark cycles (T_{dr} = 24) with day length τ lasting

886 from 4 to 18 hours. In simulations relying on $\hat{L}$ and $\hat{D}$ determined from KaiC phosphorylation

887 measurements, we set the initial condition $\hat{\theta}_0$ for a given value of τ based on our measurements

888 of entrained phase of the KaiABC oscillator in corresponding metabolic cycles (i.e., based on

889 values interpolated between black markers in Fig. 2C). Simulations using step-response

890 functions based on fluorescence polarization measurements were started from $\hat{\theta}_0 = 0$. We

891 simulated 10 light-dark cycles and recorded oscillator phase after each dawn (immediately after

892 $\hat{L}(\hat{\theta}_t)$ phase shift).

893 For each set of $\hat{L}$ and $\hat{D}$, we performed simulations for τ = 4-18 hours for both the

894 phosphorylation-based step functions and fluorescence polarization-based step functions. Fig.

895 4—figure supplement 1 illustrates simulations governed by one such set of $\hat{L}$ and $\hat{D}$ (derived

896 from magenta and blue step-response measurements shown in Figure 3C-D). We also carried out

897 entrainment simulations for the linearized step-response functions described above. For each

898 value of τ, mean entrained phase at dawn and its standard deviation are plotted as shaded areas in

899 Fig. 4—figure supplement 2A. Fig. 4—figure supplement 2B illustrates one example of the
900 driven behavior of a phase oscillator driven by the linearized versions of $\hat{L}$ and $\hat{D}$ shown in Fig.
901 3E-F.

902 We judged that the oscillator entrained stably to a given diurnal cycle if the standard
903 deviation of clock phases at dawns of the last five driving cycles was less than 0.01 cycles. For
904 each value of τ, we selected those simulations where the oscillator entrained stably to the light-
905 dark cycle, and computed the mean phase at dawn and its standard deviation (σ) for that set of
906 simulations. These values are represented in shaded areas in Fig. 4C (for fluorescence
907 polarization data) and Figure 4—figure supplement 2C (for KaiC phosphorylation data).

908 We were also interested in how quickly the oscillator approached entrainment in
909 simulations for $6 \leq \tau \leq 18$, the range we profiled experimentally in Fig. 2. To make this
910 determination for a given value of τ, we computed how much oscillator phase at dawn varied
911 over 3 successive cycles in a sliding window:

$$EC_n = \sqrt{var\left(\hat{\theta}_{n\times T_{dr}}, \hat{\theta}_{(n+1)\times T_{dr}}, \hat{\theta}_{(n+2)\times T_{dr}}\right)} \text{ for } n = 1\text{-}8$$

912 We used the first value of n for which $EC_n < 0.01$ as a proxy for the speed of approach to
913 entrainment.

914 The tables below display summary statistics for the entrainment simulations.

915 **Simulations based on step-response functions measured via fluorescence polarization reporter**

step fun. type	τ's profiled	no. sim.	% entrained sim.		% entrained within 3 cycles (8 < τ < 16)	
			4 < τ < 18	8 < τ < 16	all sim.	all sim. entr. within 8 cyc,
$\hat{\boldsymbol{L}}$ and $\hat{\boldsymbol{D}}$	4, 4.01, …, 18 hours	564	100%	100%	83%	83%
$\hat{\boldsymbol{L}}_{lin}$ and $\hat{\boldsymbol{D}}_{lin}$	4, 4.01, …, 18 hours	564	100%	100%	100%	100%

916

917 **Simulations based on step-response functions measured via SDS-PAGE analysis of KaiC phosphorylation**

step fun. type	τ's profiled	no. sim.	% entrained sim.	% entrained within 3 cycles (8 < τ < 16)

			$4 < \tau < 18$	$8 < \tau < 16$	all sim.	all sim. entr. within 8 cyc,
$\hat{\boldsymbol{L}}$ and $\hat{\boldsymbol{D}}$	4, 4.25, …, 18 hours	57 000	76%	87%	86%	97%
$\hat{\boldsymbol{L}}_{\boldsymbol{lin}}$ and $\hat{\boldsymbol{D}}_{\boldsymbol{lin}}$	4, 4.25, …, 18 hours	57 000	98%	100%	99%	100%

In the large majority of our simulations, we found that the phase oscillator entrained stably within 3 light-dark cycles. For simulations derived from KaiC phosphorylation datasets, we found that the oscillator either entrained to the driving cycle quickly or not at all. Indeed, when we restricted our analysis only to those simulations that were judged as entrained within 8 cycles, over 96% entrained within 3 light-dark cycles. Generally, the oscillator entrained readily for day lengths shorter than 14 hours, but often failed to entrain for longer day lengths. We determined that this occurs because for $\tau > 14$ dawn phases often sample the $\hat{L}$ function near the breakpoint of the curve (near 18 CT hours in Fig. 3F), leading to erratic responses to driving cues (i.e., lack of entrainment) or disagreement between simulations and experiment (Figure 4—figure 2B). Relatedly, we believe that the better agreement with experiment achieved in simulations using the step functions derived from the fluorescence polarization data than from the KaiC phosphorylation data reflects the better temporal resolution of the breakpoint (4 hours using polarization approach vs. 8 hours for KaiC phosphorylation).

In simulations of entrainment to light-dark cycles of varying period in Figure 3—figure supplement 2, we relied on a single set of $\{L, D, L_{lin}$ and $D_{lin}, T_{day}, T_{night}\}$ based on step-response measurements shown in blue and magenta in Fig. 3C-D. We simulated entrainment to driving periods from 6-48 hours, in increments of 0.0025 hours. For each driving period T_{drive}, we subjected the phase oscillator to 1000 cycles with equal day and night durations ($\tau = T_{drive}/2$) and plotted the phases attained by the oscillator at the end of night-time (immediately preceding the action of L) at the last 950 cycles.

939

940 **Simulations of phase resetting**

941

942 We used $\hat{L}_{lin}$ and $\hat{D}_{lin}$ derived from the same step-response measurements as in Fig. 4—figure
943 supplement 1 to simulate response of a phase oscillator to 12-hour dark pulses administered
944 throughout the circadian cycle (Figure 5—figure supplement 1, Mathematical Appendix—Figure
945 1D). Phase evolution of the oscillator was simulated explicitly for 120 hours using a timestep of
946 dt = 0.01 hours:

$$\hat{\theta}_{t+dt} = \begin{cases} \hat{\theta}_t + \dfrac{dt}{T_{day}} & \text{(in light)} \\ \hat{\theta}_t + \dfrac{dt}{T_{night}} & \text{(in dark)} \\ \hat{\theta}_t + \hat{L}\big(\mathrm{mod}(\hat{\theta}_t, 1)\big) & \text{(at dawn)} \\ \hat{\theta}_t + \hat{D}\big(\mathrm{mod}(\hat{\theta}_t, 1)\big) & \text{(at dusk)} \end{cases}$$

947

948 **Estimation of phase shifts in response to dark pulses *in vivo***

949

950 For phase resetting and wedge experiments (Fig. 5), clock phase was estimated by sinusoidal
951 regression of normalized bioluminescence data collected 36-48 hours after the end of the applied
952 dark pulse. Phase shifts in response to dark pulses were computed as differences in average peak
953 times between perturbed wells ($t_{pk,DP}$) and controls ($t_{pk,LL}$): $\Delta t_{pk} = \bar{t}_{pk,DP} - \bar{t}_{pk,LL}$, where
954 overbars indicate averages over replicate wells (n=4-8). Clock phases at which the dark pulses
955 were applied were determined from the average fit phase and period of the unperturbed (control)

wells ($\bar{\phi}_{LL}$ and $\bar{T}_{LL}$) according to $\theta_t = \frac{t}{\bar{T}_{LL}} - \frac{\bar{\phi}_{LL}+0.5\pi}{2\pi}$, where θ_t is measured in cycles and $\theta = 0$ corresponds to the minimum of an oscillatory trajectory.

Global fit to phase response and seasonal entrainment datasets

In the Mathematical Appendix, we show that in the regime where the circadian clock is well-approximated by a phase oscillator governed by linear *L* and *D* step-response functions, the slopes of seasonal entrainment and phase resetting of the clock can be described by a model with two free parameters β_1 and β_2: for phase resetting, $\Delta t_{pk} = \theta_t \left(\frac{1}{\omega_L \beta_2}\right) + \delta \left(1 + \frac{\beta_1}{\beta_2}\right) + C_1$ and for entrainment $t_{pk} = \tau(1 - \beta_1 - \beta_2) + T\beta_1 + C_2$. Here δ is dark pulse duration (in hours), τ is day length (in hours), θ_t is the clock phase at time *t* (in cycles), ω_L is the clock frequency in the light (in units of cycles/hour), *T* is the driving period (in hours), and C_1 and C_2 are constants that do not depend on θ_t, δ, τ, or T. For phase resetting experiments, θ_t and ω_L were estimated based on the average of the best sinusoidal fits to unperturbed wells in each experiment ($\bar{\phi}_{LL}$ and $\bar{T}_{LL}$). In particular, we set $\theta_t = \omega_L t - \frac{\bar{\phi}_{LL}+0.5\pi}{2\pi}$. In the formula for Δt_{pk}, the term $\theta_t \left(\frac{1}{\omega_L \beta_2}\right)$ thus simplifies to $\frac{t}{\beta_2} - (\frac{\bar{\phi}_{LL}+0.5\pi}{2\pi\beta_2})$, and the term to the right of the minus sign was incorporated into the constant term C_1.

In the global fits of all datasets in Fig. 5A-C, we varied β_1 and β_2 to simultaneously fit Δt_{pk} to our phase-resetting and wedge data and t_{pk} to our seasonal entrainment data. The constant terms were allowed to vary as follows:

- in Fig. 5C, a single C_2 term was fit for all curves, referred to as $C_{entrainment}$ below;

- in Fig. 5B, a single C_1 intercept was fit for both datasets (t_{DP} = 36 and t_{DP} = 39 hours), referred to as C_{wedge} below;
- in Fig. 5A, the points before and after the breakpoint were fit using the same slope, but varying constant (C_1) terms. The breakpoint was selected by visual inspection. Below, the intercepts to the left and right of the breakpoint are referred to as C_{PRC_left} and C_{PRC_right}, respectively.

In total, only two parameters (β_1 and β_2) were used to determine the slopes of all curves, and six parameters in total were used for the entire global fit of nine linear segments, which minimized the cost function:

$$\chi^2 = \sum_{i=1}^{N} \left(\frac{\hat{y}_i - y_{fit,i}}{\sigma_i} \right)^2,$$

where each y_i represents the average measurement of phase shift or peak time and σ_i represents the standard error of that measurement. The reduced chi-squared value of the fit was $\chi_\nu^2 = 5.67$. The best-fit coefficients determined in the fit are summarized in the table below.

parameter	*best-fit value*	*95% CI*
β_1	−1.31	[−1.46 −1.17]
β_2	1.79	[1.64 1.95]
C_{PRC_left}	−22.11	[−24.3 −19.9]
C_{PRC_right}	−36.98	[−40.0 −34.0]
C_{wedge}	−24.52	[−26.6 −22.5]
$C_{entrainment}$	39.8	[36.3 43.3]

Simulations of entrainment in the limit cycle geometry model

To simulate entrainment to light-dark cycles of different day length in the geometric resetting framework in Figure 6, we modeled an oscillator running along the daytime limit cycle (centered at 0, radius 1) in the light and the nighttime cycle (centered at X, radius R) in the dark. We set the angular frequency to be $\frac{2\pi \text{ rad}}{24 \text{ hours}}$ in both light and dark. As described in the Mathematical Appendix, dusk and dawn transitions were modeled as radial jumps from one cycle to the nearest point on the other cycle.

We considered values of R and X spanning six orders of magnitude and studied entrainment to 24-hour cycles with day length lasting from 6 to 18 hours. For each pair of R and X, we simulated oscillator dynamics in 30 light-dark cycles of a given day length. We judged that an oscillator failed to entrain to a given diurnal schedule if oscillator phases after 29 and 30 cycles were more than $\pi/180$ radians apart, or if simulations starting from different initial phases ($\theta_0 = \pi/4$ and $5\pi/4$) reached phases over $\pi/180$ radians apart after 30 light-dark cycles.

For every simulation that passed the entrainment criteria above, we computed the best linear fit and slope m of oscillator phase dependence on day length τ. We assessed goodness of fit by computing the mean fit error, defined as the average absolute value of the deviations between the linear fit and simulation results. If the mean fit error was greater than 10% of the deviation between maximum and minimum phases to which the oscillator entrained for this range of τ, the phase dependence on day length was judged to be non-linear.

Relaxing assumptions of the limit cycle geometry model

The results of the simulations described immediately above strongly suggest that the relative

1014 geometry of day and night orbits determines the scaling of entrained phase with day length.
1015 However, those simulations are based on idealized infinitely-attracting circular limit cycles with
1016 constant angular frequency, assumptions which are likely to be violated for biological clocks.
1017 For example, the KaiC phosphorylation limit cycles in Fig. 6F are somewhat elliptical. We were
1018 therefore interested in understanding whether the relative geometry of the limit cycles would be
1019 the dominant determinant of oscillator entrainment if our assumptions were relaxed. To this end,
1020 we explored entrainment in limit cycle models where these features—(i) orbit attraction strength,
1021 (ii) orbit ellipticity, and (iii) variation in angular frequency throughout the cycle—could be
1022 treated explicitly.
1023
1024 <u>(i) Orbit attraction strength</u>
1025 To consider the effect of orbit attraction strength (Figure 6—figure supplement 2A), we studied
1026 an oscillator with constant angular frequency ω orbiting a circular limit cycle of radius R_{orb} that
1027 is exponentially attracting:

$$\dot{\theta} = \omega = \frac{2\pi}{24}\,\frac{\text{rad}}{\text{hr}}$$
$$\dot{r} = -a(r - R_{orb}),$$

1028 where the polar coordinates (r, θ) are defined relative to the center of the limit cycle. Here, the
1029 attraction strength a determines the half-time for relaxation to the orbit according to $t_{1/2} =$
1030 $\ln(2)/a$ (hrs). During the day, the equations of motion were integrated with respect to the
1031 daytime orbit of radius 1 centered at the origin. At night, the oscillator coordinates were
1032 computed with respect to the night limit cycle of radius R centered at (0, X). We considered
1033 geometries with R and X ranging over six orders of magnitude and a = 10, 1, and 0.1. For each
1034 set of R, X and a, we simulated entrainment to ten 24-hour light-dark cycles of day length τ

between 6 and 18 hours starting from two out-of-phase initial conditions ($\theta_0 = 0$ and $\theta_0 = \pi$). After the end of the tenth entraining cycle, the oscillator was allowed to relax back to the daytime orbit. We judged the relaxation to be complete at time t_{relax} when the radial coordinate of the oscillator was within 0.02 units of the daytime orbit ($|r(t_{relax}) - R| < 0.02$). We then computed the "peak time" (t_{pk}) of this oscillator as t_{relax} plus the additional time required to reach phase $\theta = \pi/2$ after return to the orbit. For every simulation that passed the entrainment criteria as defined above, we computed the slope m the best linear fit of oscillator peak time dependence on day length τ. We assessed goodness of fit by computing the mean fit error, defined as the average absolute value of the deviations between the linear fit and simulation results. The phase dependence on day length was judged to be non-linear if the mean fit error was greater than 0.5 hours and also greater than 10% of the deviation between maximum and minimum peak times to which the oscillator entrained for this range of τ.

<u>(ii) Orbit ellipticity</u>

To consider the effect of orbit ellipticity (Figure 6—figure supplement 2B), we studied an oscillator with constant angular frequency ω orbiting an elliptical limit cycle that is exponentially attracting. We only considered orbits with their minor axes (length R_{orb}) positioned along the x axis and major axes (length $\rho \times R_{orb}$) lying parallel to the y axis. Mathematically, such an oscillator is defined by:

$$\dot{\theta} = \omega = \frac{2\pi}{24}\,\frac{\text{rad}}{\text{hr}}$$
$$\dot{r} = -a \times d_{ellipse}(r, \theta) - \dot{r}_{ellipse}(\theta),$$

where the polar coordinates (r, θ) are defined relative to the center of the limit cycle. Here

$d_{ellipse}(r,\theta)$ is the distance from the current point to the nearest point on the ellipse, and $\dot{r}_{ellipse}(\theta)$ measures how the radial coordinate changes as a function of the angle on an elliptical trajectory, assuming that $\dot{\theta}$ is constant. $d_{ellipse}(r,\theta)$ was evaluated numerically at every integration time step using the fminbnd() routine in MATLAB. $\dot{r}_{ellipse}(\theta)$ was computed explicitly based on the definition of the ellipse in polar coordinates: $\dot{r}_{ellipse}(\theta) = -\frac{1}{2}\left(\frac{\cos^2\theta}{R_{orb}^2} + \frac{\sin^2\theta}{\rho^2 R_{orb}^2}\right)^{-3/2}\left(\frac{-2\,\dot{\theta}\cos\theta\sin\theta}{R_{orb}^2} + \frac{2\,\dot{\theta}\cos\theta\sin\theta}{\rho^2 R_{orb}^2}\right)$. For all simulations in Fig. 6—figure supplement 2B, the day orbit was centered at (0, 0) with minor axis length 1 and major axis length ρ_D; the night orbit was centered at (0, X) with minor axis length R and major axis length $\rho_N R$. The attraction strength of both orbits was set to $a = 1$. Entrainment simulations were carried out for 4 light-dark cycles. Slope m was computed as in (i) above.

<u>(iii) Varying angular velocity along the limit cycle</u>

We also considered the case of circular orbits with nonconstant angular velocities (Figure 6—figure supplement 2C). To do so, we considered an oscillator defined by the following equations:

$$\dot{\theta} = \omega\left(1 + \frac{\varepsilon}{\omega}\sin\omega t\right)$$
$$\dot{r} = -a(r - R_{orb}),$$

where $\omega = \frac{2\pi}{24}\,\frac{\text{rad}}{\text{hr}}$ is the natural oscillator frequency. As above, the polar coordinates (r, θ) are defined relative to the center of the limit cycle. Such an oscillator completes one full cycle around the orbit within 24 hours, but the oscillator speed varies sinusoidally along the orbit. Here, the ratio ε/ω defines the maximal deviation of the angular velocity from the natural frequency. In the most perturbative case we considered, $\frac{\varepsilon}{\omega} = \frac{1}{2}$, the oscillator runs at 1.5 times the

1075 natural frequency at the peak of the oscillation and at 0.5 times natural frequency at the trough of
1076 the cycle. Simulations were carried out for ten light-dark cycles for orbits with attraction strength
1077 $a = 1$. Slope m was computed as in (i) above.
1078
1079 **Simulations of daytime resource allocation in days of different length**
1080
1081 Phase of transcriptional dynamics of dawn and dusk genes in Figure 6—figure supplement 3
1082 were derived from a sinusoidal fit to the transcriptional profiles of dawn and dusk genes
1083 identified in microarray time courses by Vijayan et al. (50, 51). Briefly, normalized time course
1084 data from Vijayan et al. was downloaded from the GEO depository, and time series for
1085 transcripts annotated as dawn genes were averaged to obtain the average dawn gene
1086 transcriptional profile. The average dusk gene trajectory was obtained analogously. Average
1087 dawn and dusk waveforms were fit to sinusoids with 24-hour period, and the resulting phase
1088 estimates were used to define the phase shift between the orange and grey curves in Figure 6—
1089 figure supplement 3.
1090 In Figure 6—figure supplement 3, nightfall in LD 12:12 for all values of m coincides
1091 with the 12-hour dark pulses administered during the initial synchronization in the Vijayan et al.
1092 experiment. In simulations of other day lengths (τ), we assumed that the only effect of diurnal
1093 cycling is to adjust the phase of the circadian transcriptional program relative to dawn and dusk,
1094 without affecting the shape or relative timing of dawn and dusk gene transcriptional waveforms.
1095 The bias in allocation of daytime resources between dawn and dusk genes was then computed

1096 according to the expression: $\frac{I(dawn\ gene) - I(dusk\ gene)}{I(dawn\ gene) + I(dusk\ gene)}$, where $I(gene)$ is the integrated RNA

1097 signal for that gene over the daytime hours.

1098

1099

1100 **MATHEMATICAL APPENDIX**

1101

1102 Here we outline a simple and general mathematical framework for describing the interaction

1103 between a circadian clock and its environment. The essential idea is that we model only the

1104 phase of the oscillator and decompose its dynamics into a sequence of free runs interrupted by

1105 step responses to changes in the environment (Mathematical Appendix—Figure 1). We present

1106 the assumptions of the model and then derive key formulas for interpreting our measurements.

1107

1108 **Modeling a Circadian Clock as a Phase Oscillator With Linear Response to Light-Dark**

1109 **Cues**

1110

1111 Circadian rhythms are characterized by the ability to maintain self-sustaining ≈24-hour

1112 oscillations in constant conditions and to adjust the phase of those oscillations in response to

1113 environmental signals (e.g., transitions between light and dark). To represent the first feature, we

1114 model a circadian clock as an oscillator that runs along a "light" limit cycle with speed ω_L when

1115 lights are on, and along a "dark" limit cycle with speed ω_D when lights are off (Mathematical

1116 Appendix—Figure 1A). Because the oscillator is always on one of the limit cycles, its state can

1117 be fully described by a single variable, the phase $\theta(t)$:

$$\frac{d\theta}{dt} = \omega_L \quad \text{(in light)}$$

$$\frac{d\theta}{dt} = \omega_D \quad \text{(in dark)}$$

We define frequencies in units of cycles per hour (1 cycle $= 2\pi$ radians), so that the duration of one cycle in constant conditions is $T = 1/\omega$ hours, and phase $\theta(t)$ is defined between 0 and 1.

We assume that the oscillator transitions between the two limit cycles immediately at dark-to-light ("dawn") and light-to-dark ("dusk") transitions, with a change in phase. We define $L(\theta)$ and $D(\theta)$ as phase-shifts accompanying clock responses to lights on and lights off cues, respectively:

$$\theta(t) \to \theta(t) + L(\theta(t)) \quad \text{(at dark-to-light)}$$

$$\theta(t) \to \theta(t) + D(\theta(t)) \quad \text{(at light-to-dark)}$$

Though in principle $L(\theta)$ and $D(\theta)$ could be arbitrary periodic functions, our measurements in Fig. 3 suggest that $L(\theta)$ and $D(\theta)$ are approximately linear over the range of clock phases when dawn and dusk occurred in our experiments. Henceforth we consequently assume that L and D are linear functions of θ:

$$L(\theta) = -l(\theta - \theta_L)$$

$$D(\theta) = -d(\theta - \theta_D).$$

Given this framework, we can now determine the change in clock state over any interval simply by adding the changes in phase at the transitions and accumulated during the free runs. We now explicitly compute the change in clock state in response to a dark pulse and the state of stable entrainment for light-dark cycles of arbitrary period.

Modeling Phase Resetting

To probe the response of an oscillator, one can subject it to a perturbation of duration δ and compare the resulting phase to that of an unperturbed oscillator. Plotting the results of such an assay as a function of the phase θ_t at which the perturbation is delivered yields a phase response curve (PRC; Mathematical Appendix—Figure 1C, Fig. 5A). Alternatively, varying the duration of the perturbation while delivering it at a fixed phase corresponds to a "wedge" experiment (Fig. 5B).

To determine the phase response, we need to determine the phase evolution as the system transitions to dark, free runs in the dark, and then transitions to light. Note that because this model treats the transitions between the light and dark cycles as instantaneous, we expect that it will only be valid for dark pulses that are long compared to the true relaxation time of the clock. Mathematically,

$$\theta'_{t+\delta,+} = \theta_t + D(\theta_t) + \delta\omega_D + L\left(\theta'_{t+\delta,-}\right),$$

where the prime denotes the perturbed oscillator, and the + and – in the subscripts distinguish the phase after and before the transition from dark-to-light at $t + \delta$. (That is, $\theta'_{t+\delta,-} = \theta_t + D(\theta_t) + \delta\omega_D$.) Substituting the linear forms above for D and L and grouping like terms,

$$\theta'_{t+\delta,+} = \theta_t[(1-d)(1-l)] + \delta(1-l)\omega_D + [(1-l)d\theta_D + l\theta_L].$$

Subtracting the unperturbed phase $\theta_{t+\delta} = \theta_t + \delta\omega_L$,

$$\Delta\theta = \theta'_{t+\delta,+} - \theta_{t+\delta} = \theta_t[ld - d - l] + \delta[(1-l)\omega_D - \omega_L] + [(1-l)d\theta_D + l\theta_L].$$

Thus we obtain a formula for the change in phase in response to a dark pulse, with linear dependences on the phase of the perturbation, θ_t, and its duration, δ.

Modeling Entrainment to Light-Dark Cycles

We can similarly describe the phase of a clock stably entrained to light-dark cycles of varying day length. To this end, consider a phase oscillator subjected to light-dark cycles of period T and day length τ (Mathematical Appendix—Figure 1D). In this case, rather than a phase difference, we need to determine θ_τ such that $\theta_{T+\tau} = \theta_\tau + 1$. If this condition is met, the oscillator is stably entrained to a cycle of period T. In other words, we enforce periodicity.

Proceeding analogously to above, we determine the evolution over a full driving period, starting at dusk. This comprises a transition to the dark at time τ, free run in the dark for duration $T - \tau$, a transition to the light at time T, and free run in the light for duration τ. Mathematically,

$$\theta_{T+\tau} = \theta_\tau + D(\theta_\tau) + \omega_D(T - \tau) + L(\theta_T) + \omega_L \tau.$$

Again, substituting the linear forms above for D and L and grouping like terms,

$$\theta_{T+\tau} = \theta_\tau[(1-d)(1-l)] + T(1-l)\omega_D + \tau[(1-l)\omega_D - \omega_L] + [(1-l)d\theta_D + l\theta_L].$$

Setting $\theta_{T+\tau} = \theta_\tau + 1$ and solving for θ_τ,

$$\theta_\tau = \tau\frac{(1-l)\omega_D - \omega_L}{ld - d - l} - T\frac{(1-l)\omega_D}{ld - d - l} - \frac{(1-l)d\theta_D + l\theta_L - 1}{ld - d - l}.$$

Again, we obtain a formula with linear dependence, here on the day length τ and the driving period T.

Comparison with Experiment

The expressions above describe phases, but we do not measure phase directly. Rather, we measure the time of peak expression of a reporter. Thus it is necessary to convert from phase to

the time of peak expression. To this end, we arbitrarily assign the peak expression to occur at $\theta = 0.5$ (midway through the cycle). Because phase advance and delay correspond to earlier and later peak times respectively, the time of the peak shifts with opposite sign to the phase. In each case above, we are interested when the peak (or $\theta = 0.5$) occurs relative to the last dawn (i.e., immediately after the action of *L*). We can solve for this peak time:

$$t_{pk} = \frac{0.5 - \theta_x}{\omega_L},$$

where $x = t + \delta$ (end of dark pulse) in the case of phase resetting and $x = 0$ (last dawn) in the case of entrainment. To solve for t_{pk} in entrained conditions, we make use of the fact that $\theta_0 = \theta_\tau - \omega_L \tau$, allowing us to substitute the expression above for θ_τ. For phase resetting, we must apply this formula to both the perturbed and unperturbed phase and then subtract: $\Delta t_{pk} = t_{pk}(\theta'_{t+\delta+}) - t_{pk}(\theta_{t+\delta}) = -\Delta\theta/\omega_L$.

Furthermore, we note that certain combinations of the frequencies ω_L and ω_D and the linear sensitivities l and d occur repeatedly. We thus define

$$\beta_1 = \frac{\omega_D}{\omega_L}\left[\frac{(1-l)}{ld - d - l}\right]$$

$$\beta_2 = -\frac{1}{ld - d - l}.$$

Then, for phase resetting

$$\Delta t_{pk} = \theta_t\left(\frac{1}{\omega_L \beta_2}\right) + \delta\left(1 + \frac{\beta_1}{\beta_2}\right) + C_1$$

and for entrainment

$$t_{pk} = \tau(1 - \beta_1 - \beta_2) + T\beta_1 + C_2,$$

where C_1 and C_2 are constants that do not depend on θ_t, δ, τ, or T.

In the global fits for all datasets in Fig. 5A-C, we varied β_1 and β_2 to simultaneously fit Δt_{pk} to our phase-resetting and wedge data and t_{pk} to our seasonal entrainment data. Thus, the slopes of all the linear fits in Fig. 5A-C were derived from the same values of β_1 and β_2. See Computational Methods for further details.

Geometric Resetting

In our experimental measurements, we observed *L* and *D* step-response functions with linear regions with slopes < 1. Here we present a simple dynamical systems picture where a tunable, linear dependence of phase shift magnitude on oscillator phase arises from the geometry of how a strongly attracting limit cycle is deformed by a changing external input.

We suppose that the oscillator during the day is described by a circular limit cycle in the plane with unit radius. During the night, we assume that the limit cycle remains in the plane, but is offset a distance *X* from the daytime cycle and has an altered radius *R* (Fig. 6A). At the moment of the light-to-dark transition, the state of the system is on the daytime limit cycle—it is then attracted to the nighttime limit cycle. The step-response function $D(\theta)$ describes the shift between the new phase angle (measured relative to the center of the nighttime limit cycle) and the original phase θ (Fig. 6A).

If we place the origin at the center of the nighttime limit cycle, the Cartesian coordinates of the system state immediately before the light-to-dark transition, when the system is still on the daytime orbit, are:

$$(\cos\theta + X, \sin\theta)$$

If we assume that the fixed point giving rise to the nighttime orbit is very strongly attracting, then the system approaches the limit cycle much faster than any circulation occurs. In this limit, the light-to-dark transition leads to a purely radial jump from the daytime orbit towards the center of the nighttime orbit (Fig. 6A-B). Under these conditions, the new phase θ_{night} on the nighttime cycle is simply the angle measured relative to the center of the new limit cycle:

$$\theta_{\text{night}} = \tan^{-1}\left(\frac{\sin\theta}{\cos\theta + X}\right)$$

To develop intuition about how this mapping between phase on day and night orbits is affected by their geometric arrangement, we can perform a Taylor expansion for angles near $\theta = 0$ at dusk, corresponding to conditions close to LD 12:12:

$$\theta_{\text{night}} \approx \frac{\theta}{1 + X}$$

Likewise, it can be shown that for transitions from nighttime to daytime cycles, near $\theta = \pi$, the phase immediately after transition to the daytime cycle at dawn can be given by:

$$\theta_{\text{day}} \approx \frac{\theta}{X/R + 1}$$

These expressions show that, in the linear portion of the step response function, angles are compressed by a factor tunable by the relative geometry of the light and dark limit cycles. In this way, the geometric arrangement of the limit cycles sets the slopes of $L(\theta)$ and $D(\theta)$. Numerical simulations in Figure 6 and Figure 6—figure supplement 1 were carried out using trigonometric formulas as above to convert phases between the daytime and nighttime limit cycles. Details of simulations in Figure 6—figure supplement 2 are described in Computational Methods.

1229 **Bibliography**

1230 1. de Montaigu A et al. (2015) Natural diversity in daily rhythms of gene expression
1231 contributes to phenotypic variation. *Proc Natl Acad Sci U S A* 112:905–10. Available at:
1232 http://www.pnas.org/content/112/3/905.short.
1233 2. Rémi J, Merrow M, Roenneberg T (2010) A circadian surface of entrainment: varying T,
1234 τ, and photoperiod in Neurospora crassa. *J Biol Rhythms* 25:318–328.
1235 3. Herzog ED (2007) Neurons and networks in daily rhythms. *Nat Rev Neurosci* 8:790–802.
1236 4. Daan S, Beersma DGM, Spoelstra K (2003) in *Biological Rhythms (10th Sapporo*
1237 *Symposium)*, eds Honma K, Honma S, pp 110–125.
1238 5. Nishiwaki T et al. (2004) Role of KaiC phosphorylation in the circadian clock system of
1239 Synechococcus elongatus PCC 7942. *Proc Natl Acad Sci U S A* 101:13927–32. Available
1240 at:
1241 http://www.pubmedcentral.nih.gov/articlerender.fcgi?artid=518855&tool=pmcentrez&ren
1242 dertype=abstract.
1243 6. Rust MJ, Markson JS, Lane WS, Fisher DS, O'Shea EK (2007) Ordered phosphorylation
1244 governs oscillation of a three-protein circadian clock. *Science* 318:809–12. Available at:
1245 http://www.pubmedcentral.nih.gov/articlerender.fcgi?artid=2427396&tool=pmcentrez&re
1246 ndertype=abstract [Accessed March 2, 2012].
1247 7. Flombaum P et al. (2013) Present and future global distributions of the marine
1248 Cyanobacteria Prochlrococcus and Synechococcus. *Pnas* 110:9824–9829.
1249 8. Liu Y et al. (1995) Circadian orchestration of gene expression in cyanobacteria. *Genes*
1250 *Dev* 9:1469–78. Available at: http://www.ncbi.nlm.nih.gov/pubmed/7601351.
1251 9. Ito H et al. (2009) Cyanobacterial daily life with Kai-based circadian and diurnal

1252 genome-wide transcriptional control in Synechococcus elongatus. *Proc Natl Acad Sci U S*
1253 *A* 106:14168–73. Available at:
1254 http://www.pubmedcentral.nih.gov/articlerender.fcgi?artid=2729038&tool=pmcentrez&re
1255 ndertype=abstract.
1256 10. Hosokawa N et al. (2011) Circadian transcriptional regulation by the posttranslational
1257 oscillator without de novo clock gene expression in Synechococcus. *Proc Natl Acad Sci U*
1258 *S A* 108:15396–401. Available at:
1259 http://www.pubmedcentral.nih.gov/articlerender.fcgi?artid=2729038&tool=pmcentrez&re
1260 ndertype=abstract [Accessed January 10, 2014].
1261 11. Tomita J, Nakajima M, Kondo T, Iwasaki H (2005) No transcription-translation feedback
1262 in circadian rhythm of KaiC phosphorylation. *Science* 307:251–4. Available at:
1263 http://www.ncbi.nlm.nih.gov/pubmed/15550625 [Accessed March 12, 2012].
1264 12. Zhang CC, Jeanjean R, Joset F (1998) Obligate phototrophy in cyanobacteria: more than
1265 a lack of sugar transport. *FEMS Microbiol Lett* 161:285–292.
1266 13. Nakajima M et al. (2005) Reconstitution of circadian oscillation of cyanobacterial KaiC
1267 phosphorylation in vitro. *Science* 308:414–5. Available at:
1268 http://www.ncbi.nlm.nih.gov/pubmed/15831759 [Accessed May 23, 2013].
1269 14. Kageyama H et al. (2006) Cyanobacterial Circadian Pacemaker: Kai Protein Complex
1270 Dynamics in the KaiC Phosphorylation Cycle In Vitro. *Mol Cell* 23:161–171. Available
1271 at: http://www.ncbi.nlm.nih.gov/pubmed/16857583 [Accessed December 26, 2013].
1272 15. Rust MJ, Golden SS, O'Shea EK (2011) Light-driven changes in energy metabolism
1273 directly entrain the cyanobacterial circadian oscillator. *Science* 331:220–3. Available at:
1274 http://www.pubmedcentral.nih.gov/articlerender.fcgi?artid=3309039&tool=pmcentrez&re

1275 ndertype=abstract [Accessed March 21, 2012].
1276 16. Kim Y-I, Vinyard DJ, Ananyev GM, Dismukes GC, Golden SS (2012) Oxidized
1277 quinones signal onset of darkness directly to the cyanobacterial circadian oscillator. *Proc*
1278 *Natl Acad Sci U S A* 109:17765–9. Available at:
1279 http://www.pubmedcentral.nih.gov/articlerender.fcgi?artid=3497819&tool=pmcentrez&re
1280 ndertype=abstract [Accessed November 1, 2012].
1281 17. Phong C, Markson JS, Wilhoite CM, Rust MJ (2013) Robust and tunable circadian
1282 rhythms from differentially sensitive catalytic domains. *Proc Natl Acad Sci U S A*
1283 110:1124–9. Available at: http://www.ncbi.nlm.nih.gov/pubmed/23277568 [Accessed
1284 March 5, 2013].
1285 18. Pattanayak GK, Phong C, Rust MJ (2014) Rhythms in energy storage control the ability
1286 of the cyanobacterial circadian clock to reset. *Curr Biol* 24:1934–1938. Available at:
1287 http://dx.doi.org/10.1016/j.cub.2014.07.022.
1288 19. Chang Y-G, Tseng R, Kuo N-W, LiWang A (2012) Rhythmic ring-ring stacking drives
1289 the circadian oscillator clockwise. *Proc Natl Acad Sci U S A* 109:16847–51. Available at:
1290 http://www.ncbi.nlm.nih.gov/pubmed/22967510 [Accessed March 18, 2013].
1291 20. Heisler J, Chang Y-G, Chavan A, LiWang A in *Circadian Clocks Methods and Protocols*
1292 *(in press)*, ed Brown S (Springer).
1293 21. Takai N et al. (2006) A KaiC-associating SasA-RpaA two-component regulatory system
1294 as a major circadian timing mediator in cyanobacteria. *Proc Natl Acad Sci U S A*
1295 103:12109–14. Available at:
1296 http://www.pubmedcentral.nih.gov/articlerender.fcgi?artid=1832256&tool=pmcentrez&re
1297 ndertype=abstract.

1298 22. Gutu A, O'Shea EK (2013) Two antagonistic clock-regulated histidine kinases time the
1299 activation of circadian gene expression. *Mol Cell* 50:288–94. Available at:
1300 http://www.ncbi.nlm.nih.gov/pubmed/23541768 [Accessed June 13, 2013].
1301 23. Markson JS, Piechura JR, Puszynska AM, O'Shea EK (2013) Circadian Control of
1302 Global Gene Expression by the Cyanobacterial Master Regulator RpaA. *Cell* 155:1396–
1303 1408. Available at: http://linkinghub.elsevier.com/retrieve/pii/S0092867413014189.
1304 24. Johnson CH (1999) Forty years of PRCs--what have we learned? *Chronobiol Int* 16:711–
1305 743.
1306 25. Schmitz O (2000) CikA, a Bacteriophytochrome That Resets the Cyanobacterial
1307 Circadian Clock. *Science (80-)* 289:765–768. Available at:
1308 http://www.sciencemag.org/cgi/doi/10.1126/science.289.5480.765 [Accessed November
1309 11, 2013].
1310 26. Pfeuty B, Thommen Q, Lefranc M (2011) Robust entrainment of circadian oscillators
1311 requires specific phase response curves. *Biophys J* 100:2557–2565.
1312 27. Ouyang Y (1998) The Biological Significance of the Circadian Clock in Cyanobacteria.
1313 Dissertation (Vanderbilt).
1314 28. Woelfle M, Ouyang Y, Phanvijhitsiri K, Johnson C (2004) The adaptive value of
1315 circadian clocks: an experimental assessment in cyanobacteria. *Curr Biol* 14:1481–1486.
1316 Available at: http://www.sciencedirect.com/science/article/pii/S0960982204006062
1317 [Accessed November 17, 2012].
1318 29. Pittendrigh CS (1972) Circadian surfaces and the diversity of possible roles of circadian
1319 organization in photoperiodic induction. *Proc Natl Acad Sci U S A* 69:2734–2737.
1320 30. Spoelstra K, Wikelski M, Daan S, Loudon ASI, Hau M (2015) Natural selection against a

1321 circadian clock gene mutation in mice. *Proc Natl Acad Sci*:201516442. Available at:
1322 http://www.pnas.org/lookup/doi/10.1073/pnas.1516442113.
1323 31. Pittendrigh CS, Minis DH (1972) Circadian systems: longevity as a function of circadian
1324 resonance in Drosophila melanogaster. *Proc Natl Acad Sci U S A* 69:1537–1539.
1325 32. Daan S et al. (2001) Assembling a clock for all seasons: are there M and E oscillators in
1326 the genes? *J Biol Rhythms* 16:105–116.
1327 33. Edwards KD et al. (2010) Quantitative analysis of regulatory flexibility under changing
1328 environmental conditions. *Mol Syst Biol* 6:424. Available at:
1329 http://dx.doi.org/10.1038/msb.2010.81.
1330 34. Hut R a., Oort BEH Van, Daan S (1999) Natural Entrainment without Dawn and Dusk:
1331 The Case of the European Ground Squirrel (Spermophilus citellus). *J Biol Rhythms*
1332 14:290–299. Available at:
1333 http://jbr.sagepub.com/content/14/4/290%5Cnhttp://jbr.sagepub.com/content/14/4/290.sho
1334 rt%5Cnhttp://www.ncbi.nlm.nih.gov/pubmed/10447309.
1335 35. Hut R, Paolucci S, Dor R, Kyriacou CP, Daan S (2013) Latitudinal clines: an
1336 evolutionary view on biological rhythms. *Proc Biol Sci* 280:20130433. Available at:
1337 http://rspb.royalsocietypublishing.org/content/280/1765/20130433.long.
1338 36. Wehr T a (2001) Photoperiodism in humans and other primates: evidence and
1339 implications. *J Biol Rhythms* 16:348–364.
1340 37. Rand D a, Shulgin B V, Salazar D, Millar a J (2004) Design principles underlying
1341 circadian clocks. *J R Soc Interface* 1:119–30. Available at:
1342 http://www.ncbi.nlm.nih.gov/pubmed/16849158.
1343 38. Diamond S, Jun D, Rubin BE, Golden SS (2015) The circadian oscillator in

1344 Synechococcus elongatus controls metabolite partitioning during diurnal growth.
1345 *Proc Natl Acad Sci* 2015:201504576. Available at:
1346 http://www.pnas.org/lookup/doi/10.1073/pnas.1504576112.
1347 39. Yoshida T, Murayama Y, Ito H, Kageyama H, Kondo T (2009) Nonparametric
1348 entrainment of the in vitro circadian phosphorylation rhythm of cyanobacterial KaiC by
1349 temperature cycle. *Proc Natl Acad Sci U S A* 106:1648–53. Available at:
1350 http://www.pubmedcentral.nih.gov/articlerender.fcgi?artid=2635835&tool=pmcentrez&re
1351 ndertype=abstract.
1352 40. Pittendrigh CS, Daan S (1976) A functional analysis of circadian pacemakers in nocturnal
1353 rodents - IV. Entrainment: Pacemaker as clock. *J Comp Physiol A* 106:291–331.
1354 41. Daan S (2000) The Colin S . Pittendrigh Lecture: Colin Pittendrigh, Jürgen Aschoff, and
1355 the Natural Entrainment of Circadian Systems. *J Biol Rhythms*:195–207.
1356 42. Pittendrigh CS, Minis DH (1964) The Entrainment of Circadian Oscillations by Light and
1357 Their Role as Photoperiodic Clocks. *Am Nat* 98:261.
1358 43. Johnson CH, Elliott J a, Foster R (2003) Entrainment of circadian programs. *Chronobiol*
1359 *Int* 20:741–74. Available at: http://www.ncbi.nlm.nih.gov/pubmed/14535352.
1360 44. Winfree A (1973) in *Biological and Biochemical Oscillators*, eds Chance B, Ghosh A,
1361 Pye EK (Academic Press, Inc., New York, New York, USA), p 461. 1stEd.
1362 45. Chen Y et al. (2009) A novel allele of kaiA shortens the circadian period and strengthens
1363 interaction of oscillator components in the cyanobacterium Synechococcus elongatus PCC
1364 7942. *J Bacteriol* 191:4392–4400.
1365 46. Nair U, Ditty J, Min H, Golden S (2002) Roles for Sigma Factors in Global Circadian
1366 Regulation of the Cyanobacterial Genome. *J Bacteriol* 184. Available at:

1367 http://jb.asm.org/content/184/13/3530.short [Accessed January 26, 2014].

1368 47. Lin J, Chew J, Chockanathan U, Rust MJ (2014) Mixtures of opposing phosphorylations
1369 within hexamers precisely time feedback in the cyanobacterial circadian clock. *Proc Natl*
1370 *Acad Sci* 111:E3937–E3945. Available at:
1371 http://www.pnas.org/lookup/doi/10.1073/pnas.1408692111.

1372 48. Leypunskiy E (2017) Simulations_and_analysis_pipelines_github_repo. Available at:
1373 https://github.com/euleip/Simulations_and_analysis_pipelines_github_repo (da4be43).

1374 49. Press WH, Teukolsky S a, Vettering WT, Flannery BP (1992) in *Numerical Recipes in*
1375 *Fortran 77: The Art of Scientific Computing* (Cambridge University Press), pp 650–699.

1376 50. Vijayan V, Zuzow R, O'Shea EK (2009) Oscillations in supercoiling drive circadian gene
1377 expression in cyanobacteria. *Proc Natl Acad Sci U S A* 106:22564–8. Available at:
1378 http://www.pubmedcentral.nih.gov/articlerender.fcgi?artid=2799730&tool=pmcentrez&re
1379 ndertype=abstract.

1380 51. Vijayan V, Zuzow R, O'Shea EK (2009) Oscillations in supercoiling drive circadian gene
1381 expression in cyanobacteria. Available at:
1382 https://www.ncbi.nlm.nih.gov/geo/query/acc.cgi?acc=GSE18902.

1383

1384

1385

1386 **TABLES AND TABLE CAPTIONS**

figure	**driving period *T* (hours)**	**day length *τ* (hours)**	**slope *m* ± *SD of estimate***
Fig. 1C	24	4, 6, 8, 9, 10, 11, 12, 13, 14, 16, 18, 20	0.55 ± 0.02 (sinusoidal fitting), 0.53 ± 0.01 (parabolic fitting)

Fig. 1 – fig. sup. 2	24	8, 12, 16	0.47 ± 0.03 (sinusoidal fitting), 0.57 ± 0.02 (parabolic fitting)
Fig. 5C	22, 23, 24, 25, 26	8, 10, 12, 14	0.51 ± 0.11

Table 1. Summary of biologically independent *in vivo* experiments measuring entrainment to 24-hour light-dark cycles of varying day length and corresponding estimates of *m*, the proportionality coefficient between the peak time of P_{kaiBC}*::luxAB* reporter and day length during light-dark entrainment.

FIGURE CAPTIONS

Figure 1. Phase of the cyanobacterial circadian rhythm scales linearly with day length.
(A) LED array device used to grow *S. elongatus* in programmable light-dark cycles. Cells grown in a 96-well plate on solid media (lower plate, *green circles*) are illuminated from above by LEDs (*red circles*). An Arduino microcontroller is used to dynamically change LED intensity in different columns of the plate (*inset*). Luminescence from the bottom plate is read out every 30 minutes on a plate reader. Drawing not to scale.
(B) Drive-and-release strategy to measure phase of the circadian clock under light-dark (LD) cycling. Cells were exposed to five entraining LD cycles and then released into constant light. Bioluminescence signals (P_{kaiBC}::*luxAB*) from each well were separated into individual "day" and "night" windows. Data from night portions of the experiment were omitted from analysis (*gray bars*) and data from the day portions of the experiment were aligned to zero baseline and normalized to unit variance. Dashed lines indicate time of peak reporter signal calculated by parabolic fitting. See Computational Methods for details.
(C) Peak time of bioluminescence (P_{kaiBC}::*luxAB*) in light-dark cycles of different day length *(red squares)* was quantified by local parabolic fitting around the first maximum of the oscillation after release into constant light. Error bars represent standard deviations of peak time estimates from technical replicates (n=4-8). Slope of the linear fit (*red line*, m=0.53±0.01) was determined by linear regression. *Dashed and dotted black lines* indicate scaling of phase with day length for dawn- and dusk-tracking oscillators; *green line* indicates midday-tracking behavior.

Figure 1—figure supplement 1. Bioluminescence recordings from P_{kaiBC}*::luxAB* reporter in light-dark cycles.
(*left*) Selected bioluminescence traces (P_{kaiBC}*::luxAB, black*) recorded from individual wells of the 96-well LED array device in conditions simulating day-night cycles of different day length (same dataset as in Fig. 1B-C). Data recorded in the dark were omitted from analysis (*gray bars*). Each trajectory was normalized to the mean and variance of the bioluminescence signal recorded after the release into constant light, and trajectories recorded after release into constant light were fit to sinusoids (*green*). For illustration purposes here, trajectories were aligned to zero baseline. See Computational Methods for fitting details. (*right*) Similarity between the bioluminescence rhythms (P_{kaiBC}*::luxAB)* recorded during light-dark entrainment and after release into free running conditions. Nonparametric correlation coefficient (Kendall's τ) between bioluminescence trajectories recorded in the light during entrainment (days 1-5) and the corresponding time period after release into constant light (e.g., a 16-hour window in LL for LD 16:8). See Computational Methods for details.

Figure 1—figure supplement 2. The circadian rhythm of *S. elongatus* rapidly entrains to 24-hour diurnal cycles with 8-16 hours of daylight.

1430 (A) Peak times of P_{kaiBC}*::luxAB* reporter after release into LL from 1-7 LD cycles of different day length
1431 (LD 8:16, LD 12:12 or LD 16:8), as estimated by sinusoidal regression. Error bars represent the standard
1432 deviation (σ) of technical replicates (n=6-8 replicates per condition). Lines mark linear fits to the data.
1433 (B) Slope *m* of clock phase scaling with day length stabilizes after three light-dark cycles. Slope of linear
1434 fits in (A) plotted against day length in diurnal cycles. Error bars mark uncertainty in fit slope (±*σ*).
1435 (C) Slope *m* of clock phase scaling with day length, as estimated by parabolic regression (see
1436 Computational Methods).
1437 (D and E) Free-running period of P_{kaiBC}*::luxAB* reporter rhythms, as estimated from sinusoidal fits (D) or
1438 local parabolic fits (E), recorded in continuous light after entrainment to 24-hour cycles with 8, 12, or 16
1439 hour of daylight.
1440
1441 **Figure 1—figure supplement 3.** Bioluminescence recordings from P_{purF}*::luxAB* reporter in light-dark
1442 cycles.
1443 (A) Rhythms in bioluminescence in continuous light recorded from a dawn gene reporter (*PpurF::luxAB)*
1444 after entrainment to 24-hour light-dark cycles of different day length *τ* (LD 8:16, LD 10:14, LD 14:10,
1445 LD 18:6). Following the protocol in Fig. 1, cells received five light-dark cycles and were then placed
1446 under continuous illumination. Bioluminescence trajectories from first 72 hours after release into constant
1447 conditions were aligned to zero baseline and normalized to unit variance.
1448 (B) Peak times of the *PpurF::luxAB* reporter after release into constant light after five LD cycles of
1449 different day length (LD 4:20 to LD 20:4). Peak times were determined by local parabolic regression (see
1450 Computational Methods). Error bars represent standard errors of technical replicates (n=4-8). Straight
1451 lines represent linear fits to data from wells entrained to day lengths at least 8 hours long.
1452
1453
1454 **Figure 2.** Reconstitution of the seasonal clock response *in vitro*.
1455 (A) Buffer exchange protocol to simulate metabolic driving of the clock. To mimic daytime *in vitro*,
1456 purified Kai proteins (*green, blue and red symbols*) were incubated in "day" reaction buffer containing 2
1457 mM (%P-KaiC) or 2.5 mM (fluorescence polarization) ATP. ADP was added (7.5 mM ADP final) to
1458 mimic nightfall. At simulated dawn, reactions were returned to "day" buffer via buffer exchange.
1459 (B) Example traces of KaiC phosphorylation rhythm from *in vitro* reactions mimicking LD 18:6 (*top*), LD
1460 12:12 (*middle*), and LD 6:18 (*bottom*).
1461 (C) Phase of KaiABC oscillation scales linearly with simulated day length (time spent in "day" buffer), as
1462 assessed by the peak time of KaiC phosphorylation (*black squares*) or peak time of fluorescence
1463 polarization (*cyan squares* and *circles*, for two replicates) of fluorescently labeled KaiB. Peak times of
1464 fluorescence polarization were estimated from sinusoidal fits to oscillations recorded in free-running
1465 conditions after entraining the oscillator with three metabolic cycles. Peak time of %P-KaiC was
1466 estimated by fitting KaiC phosphorylation time series from the third day of reactions to sinusoids. Error
1467 bars represent uncertainty of fit phase from sinusoidal regression. Lines of best fit determined by linear
1468 regression (*cyan squares: m*=0.39±0.06, *cyan circles: m*=0.36 ± 0.04, *black: m*=0.51±0.04). *In vivo* data
1469 (from Fig. 1C) is plotted in *red*. Scaling of entrained phase was measured once via KaiC phosphorylation
1470 analysis (*black*) and twice using the fluorescence polarization probe (*cyan squares* and *circles*) with an
1471 independent preparation of proteins.
1472
1473 **Figure 2—figure supplement 1.** Validation of KaiB fluorescence polarization reporter against KaiC
1474 phosphorylation rhythm.
1475 (*top*) Fluorescence polarization of KaiABC mixture probed with fluorescently-labeled KaiB exhibits
1476 ≈24-hour rhythms (*black and blue squares*). (*bottom*) KaiC phosphorylation rhythm of the same reaction
1477 mixtures as in the top panel (*black and blue squares*). *Black vs blue markers* show data from two identical
1478 reactions started at different times. Curves show best-fit sinusoids, where all reactions share a common

period; the phase offset between out of phase reactions was also a shared parameter in fits to polarization and phosphorylation datasets. This experiment was performed once.

Figure 3. Clock responses to metabolic steps mimicking dawn (step up) and dusk (step down).
(A) Phase shift in fluorescence polarization (*red curve*) caused by a shift to a buffer that mimics the nucleotide pool at night (7.5 mM ADP, 2.5 mM ATP, *gray bar*). The control reaction remained in the original buffer (*black curve*).
(B) Phase shift in fluorescence polarization (*blue curve*) caused by a shift from night buffer back to day buffer (2.5 mM ATP, *beige bar*).
(C, D) Summary of phase shifts caused by metabolic step-down (C) or step-up (D) perturbations throughout the clock cycle. Simulated day-night or night-day steps were administered as in (A) and (B). Different colors represent independent measurements. To estimate the phase of each reaction, trajectories were fit to sinusoids. Phase shifts were determined relative to the respective control reactions. The times at which buffer steps were administered were converted to circadian time (CT 0 corresponds to the estimated trough of KaiC phosphorylation based on Figure 2—figure supplement 1). Colored arrows indicate clock phases when metabolic shifts occur in entrained conditions.
(E, F) Analogs of (C, D) for the gel-based phosphorylation measurements on an independent preparation of Kai proteins. Simulated day-night or night-day steps were administered by ADP addition to simulate nighttime (7.5 mM ADP, 2 mM ATP) or buffer exchange into a high-ATP buffer to simulate daytime (2 mM ATP). Data analysis was analogous to (C, D). Error bars represent standard deviations calculated by bootstrapping (see Computational Methods). Horizontal error bars are smaller than marker widths.

Figure 3—figure supplement 1. Example calculation of phase shifts in response to metabolic step transitions.
Phase shifts are computed from the difference in phase of the control reaction and the perturbed reaction evaluated at the time of the step. Phase of each reaction at the time of the step (*green dashed line*) is calculated based on the sinusoidal fit to the normalized fluorescence polarization trajectory for that reaction. Periods of the oscillator in day and night conditions were fit globally to all reactions measured in one experiment. See Computational Methods for fitting details.

Figure 3—figure supplement 2. Experimentally-measured step-response functions predict entrainment to driving periods near 24 hours.
(A) Entrainment simulations with driving periods 4-48 hours were performed for 1000 cycles, and phases at the end of nighttime (immediately before the action of L) of the last 920 cycles were plotted. Simulation results are double-plotted along the vertical axis for clarity. In each simulation, the oscillator runs at constant angular speed in the light and dark, and experiences instantaneous phase shifts at dawn and dusk, according to the values of L and D. Refer to Fig. 4A for an illustration of a single entrainment simulation.

Figure 4. Entrainment of the phase oscillator model to a driving cycle.
(A) Schematic of a phase-only oscillator that responds to dawn and dusk with instantaneous phase shifts. The oscillator runs at constant velocities ω_L during the day and ω_D at night (*green lines*), except for dawn and dusk where sudden shifts occur (*red and blue arrows*). This simulation illustrates entrainment to a LD 12:12 diurnal cycle for an oscillator with ω_L (1/23.7 hours), ω_D (1/25.7 hours), and $L(\theta)$ and $D(\theta)$ as experimentally measured for the KaiABC oscillator (see main text, Computational Methods). Refer to Figure 4—supplementary figure 1B for illustrations of $L(\theta)$ and $D(\theta)$ used in this simulation.

(B) Simulated approach to stable entrainment in the model (as in Fig. 4A) for light-dark cycles of different day length (τ=8-14 hours).
(C) Simulated seasonal response of an oscillator that responds rapidly to light-dark cues according to the phase shift functions in Fig. 3C (see text). In simulations, t_{pk} is defined as the time when oscillator phase θ equals 0.5 rad/2π, corresponding to the peak of KaiC phosphorylation. Shaded areas correspond to standard deviations of entrainment simulations using the four possible combinations of L and D functions shown in Fig. 3(C-D). *Blue squares and circles* indicate experimentally determined entrained phases measured using the fluorescence polarization reporter in Figure 2C. Peak times in polarization data were converted to equivalent peak KaiC phosphorylation times using the measured phase offset for the polarization reporter of 2π/3 rad (Fig. 2—figure supplement 1). Error bars on *in vitro* data are based on uncertainty of fit phase of sinusoidal trajectories.

Figure 4—figure supplement 1. Example simulation of a phase oscillator governed by one set of experimentally determined $L(\theta)$ and $D(\theta)$ functions and subjected to a driving cycle.
(A) The phase oscillator reaches stable entrainment within 3-5 light-dark cycles (τ=10-14 hours) for a wide range of starting phases. Simulation parameters same as in Fig. 4B; $L(\theta)$ and $D(\theta)$ as shown in (B) below.
(B) Example pair of step response functions, denoted $\hat{L}(\hat{\theta})$ and $\hat{D}(\hat{\theta})$, measured using the fluorescence-polarization reporter of KaiB-KaiC binding (magenta and blue curves in Fig. 3C-D). Colored circles mark phases corresponding to dawn (on $\hat{L}(\hat{\theta})$) and dusk (on $\hat{D}(\hat{\theta})$) in seasonal entrainment simulations of different day length τ (see color bar). θ=0 refers to the phase when the minimum of the KaiC phosphorylation rhythm occurs. See Computational Methods for details.

Figure 4—figure supplement 2. Simulations of seasonal entrainment for a phase oscillator driven by linearized step-response functions (L_{lin} and D_{lin}).
(A) Simulated seasonal response of phase oscillators governed by the four possible combinations of nonlinear $\hat{L}(\hat{\theta})$ and $\hat{D}(\hat{\theta})$ step-response functions in Fig. 3(C-D) (*blue shaded areas*) and their linearized versions $\hat{L}_{lin}(\hat{\theta})$ and $\hat{D}_{lin}(\hat{\theta})$ (*shaded green areas*). In simulations, t_{pk} is defined as the time when oscillator phase θ equals 0.5 rad/2π, corresponding to the peak of KaiC phosphorylation. *In vitro* measurements overlaid in blue as in Fig. 4C.
(B) Simulated seasonal response of phase oscillators governed by step-response functions measured for an independent preparation of clock proteins using SDS-PAGE analysis of KaiC phosphorylation Fig. 3(E-F). Shaded areas correspond to standard deviations determined by bootstrapping (see Computational Methods). *Blue squares* show seasonal response measured in the purified KaiABC oscillator using the same preparation of proteins and measured via SDS-PAGE (Fig. 2C). t_{pk} is defined as in (B) above. Error bars represent uncertainty of fit phase from sinusoidal regression.
(C) Example pair of step-response functions $\hat{L}(\hat{\theta})$ and $\hat{D}(\hat{\theta})$ and their linearized versions, $\hat{L}_{lin}(\hat{\theta})$ and $\hat{D}_{lin}(\hat{\theta})$, used in simulations in (A) above and measured using the fluorescence-polarization reporter of KaiB-KaiC binding (magenta and blue curves in Fig. 3C-D). Colored circles mark stably entrained phases corresponding to dawn (on $\hat{L}(\hat{\theta})$) and dusk (on $\hat{D}(\hat{\theta})$) in simulations of different day length τ (see color bar). θ=0 refers to the minimum of KaiC phosphorylation rhythm. See Computational Methods for details.

Figure 4—figure supplement 3. Dependence of the slope of entrained phase on the slopes of step response functions.
Heat map of slope m, describing the scaling of oscillator peak time with day length, as a function of the slopes l and d of linear $L(\theta)$ and $D(\theta)$ step response functions and oscillator frequencies in light and dark (ω_D and ω_L) (see main text and Mathematical Appendix). This relationship is described by $m(l,d) =$

$1 - \frac{-(1-l)\times(\omega_D/\omega_L)}{d+l-ld} - \frac{1}{d+l-ld}$. The ratio of oscillator frequencies in light and dark was estimated to be $\frac{\omega_D}{\omega_L} = 0.94$ based on the analysis of datasets in Figure 3(C-D). Dashed isolines connect all points with *m*=0.53 (*left*) and *m*=0.38 (*right*), corresponding to our estimates of scaling coefficients *in vivo* and *in vitro* in Figure 2(C). The approximate range of values of *l* and *d* estimated from experimental measurements in Fig. 3(C-D) is indicated by the white crosshair. Crosshair lengths represent mean±standard deviation of estimates of *l* and *d* determined by bootstrapping, as described in Computational Methods.

Figure 5. Phase oscillator model with linear phase shift functions predicts entrainment of the cyanobacterial clock to different light-dark (LD) patterns. In all panels, error bars represent standard deviations (n=4-8 technical replicates per point). Lines are fit globally to all three datasets in (A)-(C). See Computational Methods for details.

(A) Phase resetting analysis. Phase shifts of bioluminescence rhythm (P_{kaiBC}::*luxAB*) due to 12-hour dark pulses (δ=12 hours) administered throughout the circadian cycle. The experimental protocol is represented schematically above the graph. Cells were exposed to one 12-hour dark pulse and released into constant light; 12-hour dark pulses were administered at the indicated times. $\theta(t_{DP})$ is the clock phase at beginning of the dark pulse, with θ=0 defined as clock phase at the trough of the bioluminescence rhythm.

(B) Wedge analysis. Phase shifts of bioluminescence rhythm (P_{kaiBC}::*luxAB*) due to dark pulses of varied length (δ=12-16 hours) administered at subjective dusk (36 or 39 hours after an initial 12 hour dark pulse). Clock phases at the beginning of the dark pulse are listed in parentheses; θ=0 is defined as clock phase at the trough of the bioluminescence rhythm. The experimental protocol is represented schematically above the graph as in (A).

(C) Seasonal response in non-24 hour environmental cycles. Cells were grown in LD cycles with period T=20-26 hours and day length τ=8-14 hours (see schematic on left). After five entraining cycles, cells were released into LL and the phase of the circadian rhythm was estimated by sinusoidal regression.

Figure 5—figure supplement 1. Simulation of a phase-resetting curve.

(*left*) Simulated phase-resetting curve due to a 12-hour dark pulse for a phase oscillator governed by linear step-response functions $\hat{L}_{lin}(\hat{\theta})$ and $\hat{D}_{lin}(\hat{\theta})$ (*right*), as in in Fig. 4—figure supplement 2. Colored circles indicate phases at the beginning of the dark pulse (see color bar). θ=0 refers to the trough of the KaiC phosphorylation rhythm.

Figure 6. Nearly linear step response functions can arise from the relative geometry of day and night limit cycles.

(A) Geometric model of oscillator phase resetting. During the day, the oscillator runs with constant angular velocity along the daytime orbit (*yellow*), which has unit radius and is centered at the origin. At dusk, the oscillator transits to the nighttime orbit (*black*), which has radius *R* and is displaced from the daytime orbit by *X* units. In the limit where the nighttime orbit is strongly radially attracting, we can approximate oscillator response to the light-dark transition ($D(\theta_\tau)$, *red arrow*) as an instantaneous jump from phase θ_τ on the daytime orbit towards the center of the nighttime cycle, resulting in phase $\theta_\tau + D(\theta_\tau)$ on the night orbit.

(B) Simulation of oscillator phase shifts due to light-dark transitions at different phases on the day orbit (*red arrows*) for $R = 2$, $X = 2$. For limit cycle geometries with $X \approx R$, phase angles on the day orbit are compressed to an arc on the night limit cycle that subtends a smaller angle. See Computational Methods for calculation details.

(C and D) Simulations of $L(\theta)$ and $D(\theta)$ step response functions arising from the geometric arrangement of day and night cycles in (B). Linear regions of $L(\theta)$ and $D(\theta)$ are marked with black dashes. See Computational Methods and Mathematical Appendix for calculation details.
(E) Heat map of the slope *m* of the approximately linear relationship between entrained phase and day length, plotted as a function of *X* and *R*. In white regions, the oscillator does not entrain stably or the oscillator does not show linear scaling of phase with day length. Slope determined from simulations of oscillator entrainment to 24-hour driving cycles of day length τ=6-18 hours. See Computational Methods for details.
(F) Limit cycles traversed by the KaiABC oscillator *in vitro* in metabolic conditions mimicking day (*black*, 100% [ATP]/([ATP]+[ADP])) and night (*yellow*, 25% [ATP]/([ATP]+[ADP])). Oscillations in KaiC phosphorylation on Ser431 and Thr432 are replotted from data in Phong et al. (2013) (17).

Figure 6—figure supplement 1. Illustrations of limit cycle geometries that give rise to step-response functions $L(\theta)$ and $D(\theta)$ with different slopes, resulting in dusk-, dawn-, or midday-tracking entrainment. In all schematics, the day orbit (*yellow*) is centered at the origin and has radius 1. The night orbit (*black*) has radius *R* and is displaced from the day orbit ($\log X = 0.5$) units. Light-dark ($D(\theta)$) and dark-light ($L(\theta)$) transitions are indicated by *red* and *blue arrows*, respectively.
(A) When the night cycle is much smaller than the day cycle ($R << 1$), both dawn and dusk are strongly resetting ($l \approx 1$, $d \approx 1$). Because all phases on the night orbit are mapped to a small range of phases on the day orbit, oscillator phase at dawn is independent of day length during entrainment ($m \approx 0$, dawn-tracking).
(B) When the sizes of day and night orbits are comparable ($R \approx 1$), the slopes of $L(\theta)$ and $D(\theta)$ depend on the fine-tuned arrangement of the orbits. Generally, both $L(\theta)$ and $D(\theta)$ exert entraining effects in this regime ($l > 0$, $d > 0$). The slope of entrained phase with day length depends on both *l* and *d*, according to $m(l,d) = d(1-l)/(d+l-ld)$ (see Figure 4—figure supplement 3 and Mathematical Appendix).
(C) When the night cycle is much bigger than the day cycle ($R >> 1$), dusk is strongly resetting, but dawn transitions have little effect on clock phase ($l \approx 0$, $d \approx 1$). Entrainment to repeated light-dark cycles maps clock phases on the night orbit to a shrinking range of angles, leading to dusk-tracking entrainment ($m \approx 1$).

Figure 6—figure supplement 2. The relative size (*R*) and center-to-center distance (*X*) of day and night limit cycles are major determinants of entrained behavior. Heat maps of *m*, the slope of the approximately linear relationship between entrained phase and day length, are plotted as a function of *X* and *R* on the same color scale as in Fig. 6E. See Computational Methods for simulation details.
(A) Entrainment simulations with non-instantaneous jumps between day and night limit cycles. The half-times $t_{1/2}$ for transition between the circular orbits are indicated above the heat maps. Schematic on the left illustrates the evolution of the oscillator from a point on the night limit cycle to the day limit cycle in two scenarios with different relaxation times. Each arrow represents the displacement of the oscillator in 1 hour.
(B) Entrainment simulations for day and night limit cycles of varying ellipticity. The ratios of the major axis length to the minor axis length of the day and night orbits (ρ_D and ρ_N) are indicated above the heatmaps. In these simulations we considered strongly attracting orbits ($t_{1/2} = 0.069$ hours) oriented with their major axes perpendicular to the separation between their centers.
(C) Entrainment simulations for day and night limit cycles with non-constant angular velocities. In these simulations we considered circular orbits for both day and night limit cycles. Orbit attraction timescale was set to $t_{1/2} = 0.69$ hours. The variability in angular speed $\dot{\theta}$ throughout the cycle is given by $\dot{\theta} = \omega\,(1 + \frac{\varepsilon}{\omega}\sin\omega t)$. Schematic on the left illustrates the evolution of the oscillator along day limit cycle in two scenarios with different values of $\frac{\varepsilon}{\omega}$. Each arrow represents the displacement of the oscillator in 1 hour; size of the arrowheads illustrates changes in angular velocity throughout the cycle (not to scale).

Figure 6—figure supplement 3. Interpretation of *m*, the slope of the approximately linear relationship between entrained phase and day length.
(A) The value of *m* dictates whether the circadian rhythm aligns to dawn ($m = 0$), dusk ($m = 1$), or an intermediate point of the day-night cycle (e.g., midday for $m = 0.5$). Orange and gray curves show sinusoidal fits to average transcriptional profiles of dawn and dusk genes in *S. elongatus* based on data from Vijayan et al. (2009) (50). Gray bars indicate night in light-dark cycles for $m = 0$, 0.5, and 1.
(B) Tracking midday as the day length varies represents a strategy to balance biosynthetic resources between dawn and dusk transcriptional programs. For each value of *m*, the corresponding curve shows a numerical estimate of the relative fraction of dusk and dawn gene expression that occurs during the day in *S. elongatus* (arbitrary units, see Computational Methods).

Mathematical Appendix—Figure 1. Phase oscillator with linear response framework.
(A) Schematic of the phase oscillator framework. In the light portion of the day, the oscillator runs along the "light" limit cycle (*orange*) and accumulates phase θ at constant rate ω_L; in the dark, the oscillator runs along the "dark" limit cycle (*blue*) with frequency ω_D. At dawn (*solid blue circle*) and dusk (*solid orange circle*), the oscillator transitions between the light and dark limit cycles (*blue and orange arrows*) and incurs instantaneous phase shifts given by $L(\theta)$ at dawn and $D(\theta)$ at dusk. In the linear approximation framework, $L(\theta)$ and $D(\theta)$ are linear functions of phase, such that $L(\theta) = -l(\theta - \theta_L)$ and $D(\theta) = -d(\theta - \theta_D)$. Colors along the "light" and "dark" limit cycles indicate the magnitude of phase shifts due to light-to-dark ($D(\theta)$) and dark-to-light ($L(\theta)$) responses throughout the cycle for a single set of linearized $L(\theta)$ and $D(\theta)$, shown in (B), generated by bootstrapping the measurements in Fig. 3E-F. $\theta = 0$ refers to the minimum of KaiC phosphorylation rhythm.
(B) One set of linearized step response functions $\hat{L}_{lin}(\hat{\theta})$ and $\hat{D}_{lin}(\hat{\theta})$ for the KaiABC oscillator determined by SDS-PAGE analysis of KaiC phosphorylation rhythms (see Fig. 3E-F). The functions plotted represent one pair of $\hat{L}_{lin}(\hat{\theta})$ and $\hat{D}_{lin}(\hat{\theta})$ generated by bootstrapping (see Computational Methods). Colors denote phase shift magnitude as in (A). Solid circular markers correspond to dawn and dusk transitions in (A).
(C) (*left*) Schematic of phase response analysis in the phase oscillator framework. The phase shift is a linear function of the dark pulse time (t_{DP}) and duration (δ) if $L(\theta)$ and the $D(\theta)$ are linear functions. Slopes of linear dependencies on t_{DP} and duration δ can be computed based on clock frequencies in light and dark (ω_L, ω_D) and slopes of $L(\theta)$ and $D(\theta)$ functions. (*right*) Simulation of a phase response experiment for a phase oscillator with experimentally determined parameters (ω_L, ω_D, l, and d from the same bootstrapped parameter set as in (B)). A 9-hour dark pulse applied 4 hours after the beginning of the simulation to an oscillator (*green*) results in a ≈8 hour phase delay relative to a control (*black*) that remains in light throughout the simulation.
(D) (*top*) Schematic of analysis of seasonal entrainment in the phase oscillator framework. Entrained phase is a linear function of day length (τ) and driving period (T) if $L(\theta)$ and the $D(\theta)$ are linear functions. Slopes of linear dependencies on τ and T can be computed based on four parameters (ω_L, ω_D, l, and d). (*bottom*) Simulation of entrainment to a LD 12:12 cycle for a phase oscillator with experimentally determined parameters (ω_L, ω_D, l, and d from the same bootstrapped parameter set as in (B)).

SOURCE DATA FILES CAPTIONS

Figure 1—source data 1. Source data for Figure 1B.
Figure 1—source data 2. Source data for Figure 1C.
Figure 1—source data 3. Source data for bioluminescence trajectories in Figure 1—figure supplement 1.
Figure 1—source data 4. Source data for Kendall's τ correlations in Figure 1—figure supplement 1.
Figure 1—source data 5. Source data for Figure 1—figure supplement 2A-E.
Figure 1—source data 6. Source data for Figure 1—figure supplement 3A, showing bioluminescence output from the *purF* repoter.
Figure 1—source data 7. Source data for Figure 1— figure supplement 3B.

Figure 2—source data 1. Source data for Figure 2B.
Figure 2—source data 2. Source data for Figure 2C.
Figure 2—source data 3. Source data for Figure 2—figure supplement 1.

Figure 3—source data 1. Source data for Figure 3A-B.
Figure 3—source data 2. Source data for Figure 3C-D.
Figure 3—source data 3. Source data for Figure 3E-F.

Figure 4—source data 1. Source data for Figure 4C. This file contains data from *in vitro* entrainment measurements shown as blue circles and squares.
Figure 4—source data 2. Source data for Figure 4—figure supplement 2. This file contains *in vitro* entrainment measurements shown as blue squares in Figure 4—figure supplement 2B.

Figure 5—source data 1. Source data for Figure 5A-C.

Figure 1.

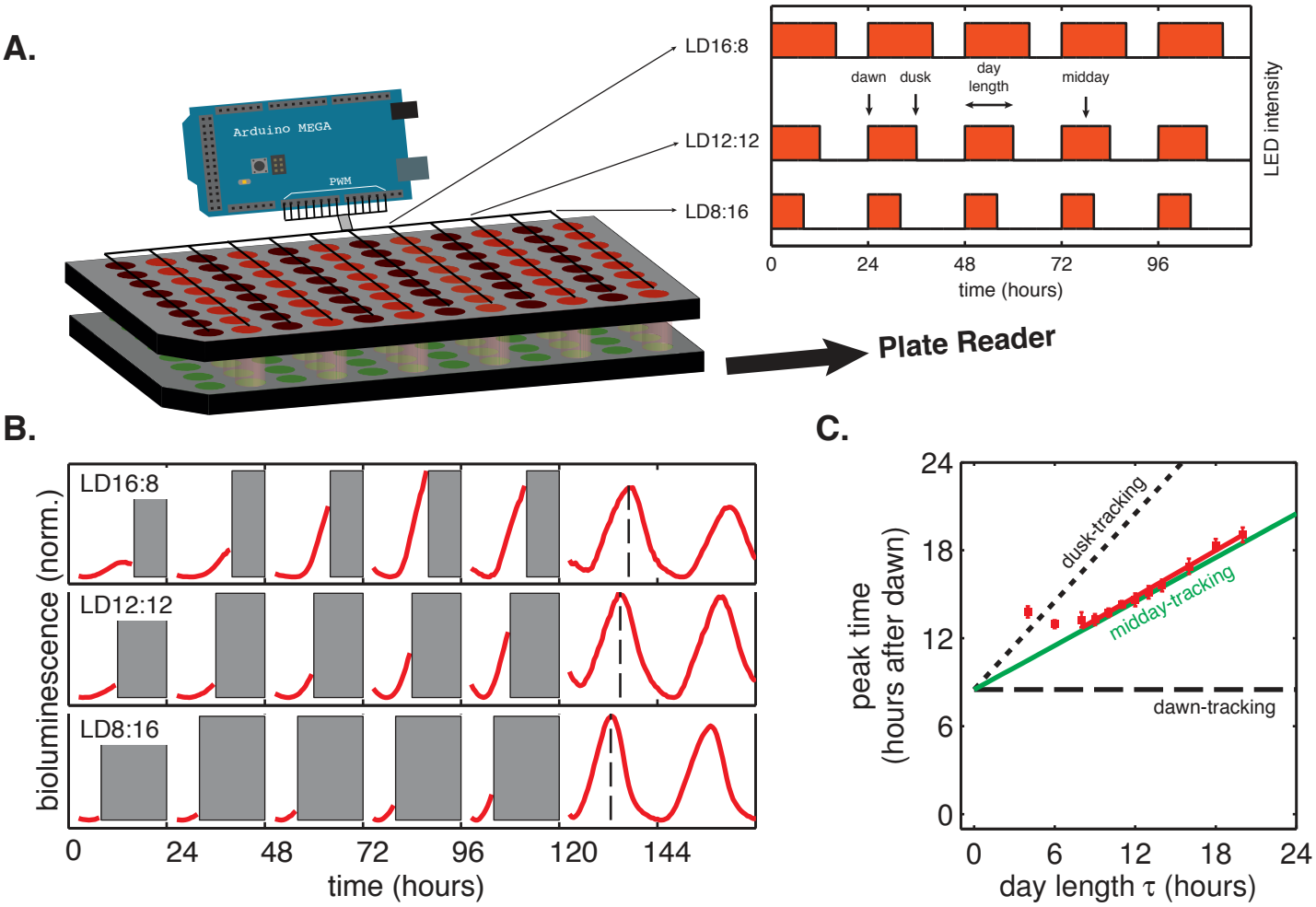
A.
Arduino MEGA
PWM
LD16:8
LD12:12
LD8:16
dawn
dusk
day length
midday
LED intensity
0
24
48
72
96
time (hours)
Plate Reader
B.
LD16:8
LD12:12
LD8:16
bioluminescence (norm.)
0
24
48
72
96
120
144
time (hours)
C.
dusk-tracking
midday-tracking
dawn-tracking
peak time (hours after dawn)
0
6
12
18
24
day length τ (hours)

Figure 1—figure supplement 1.

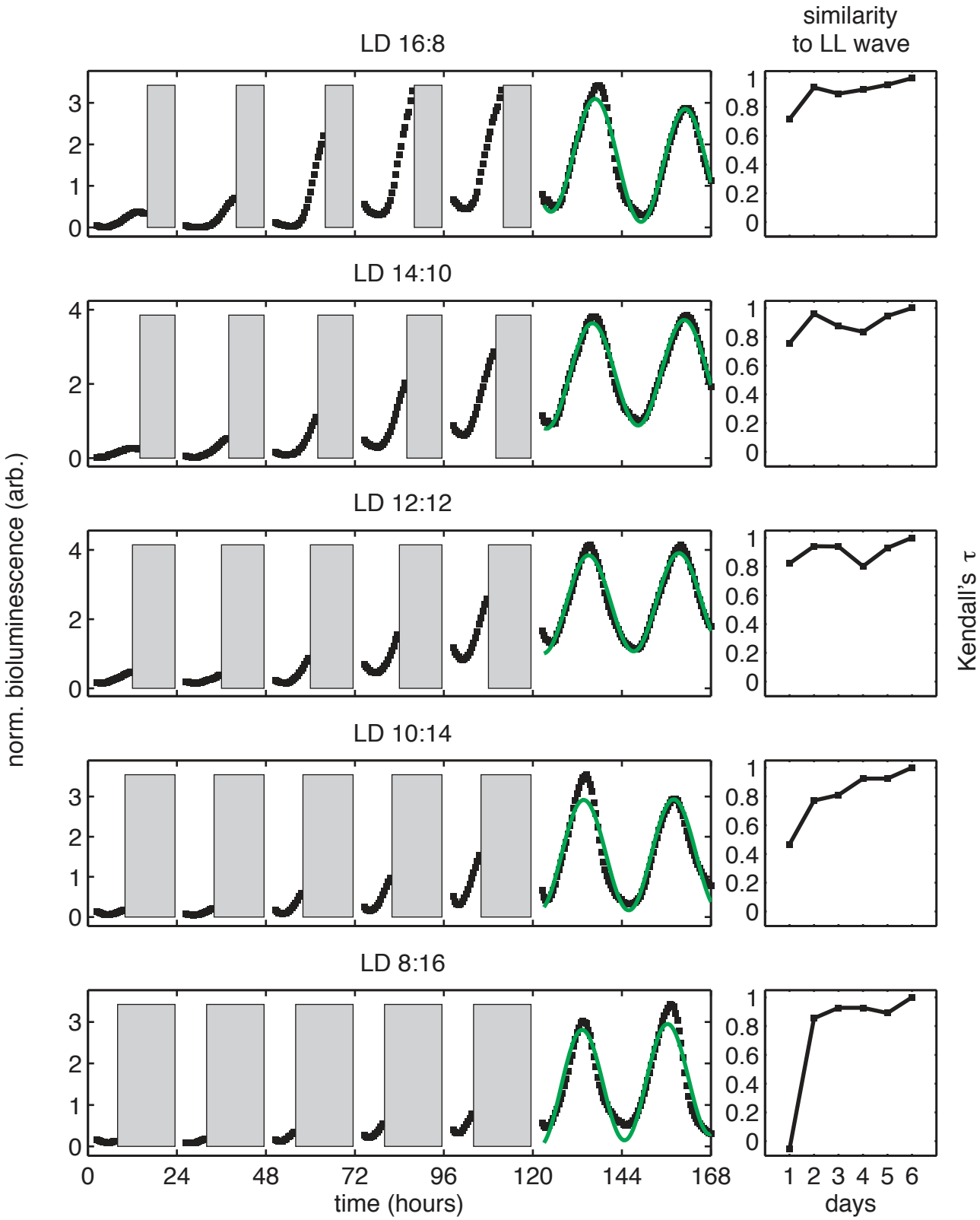

Figure 1—figure supplement 2.

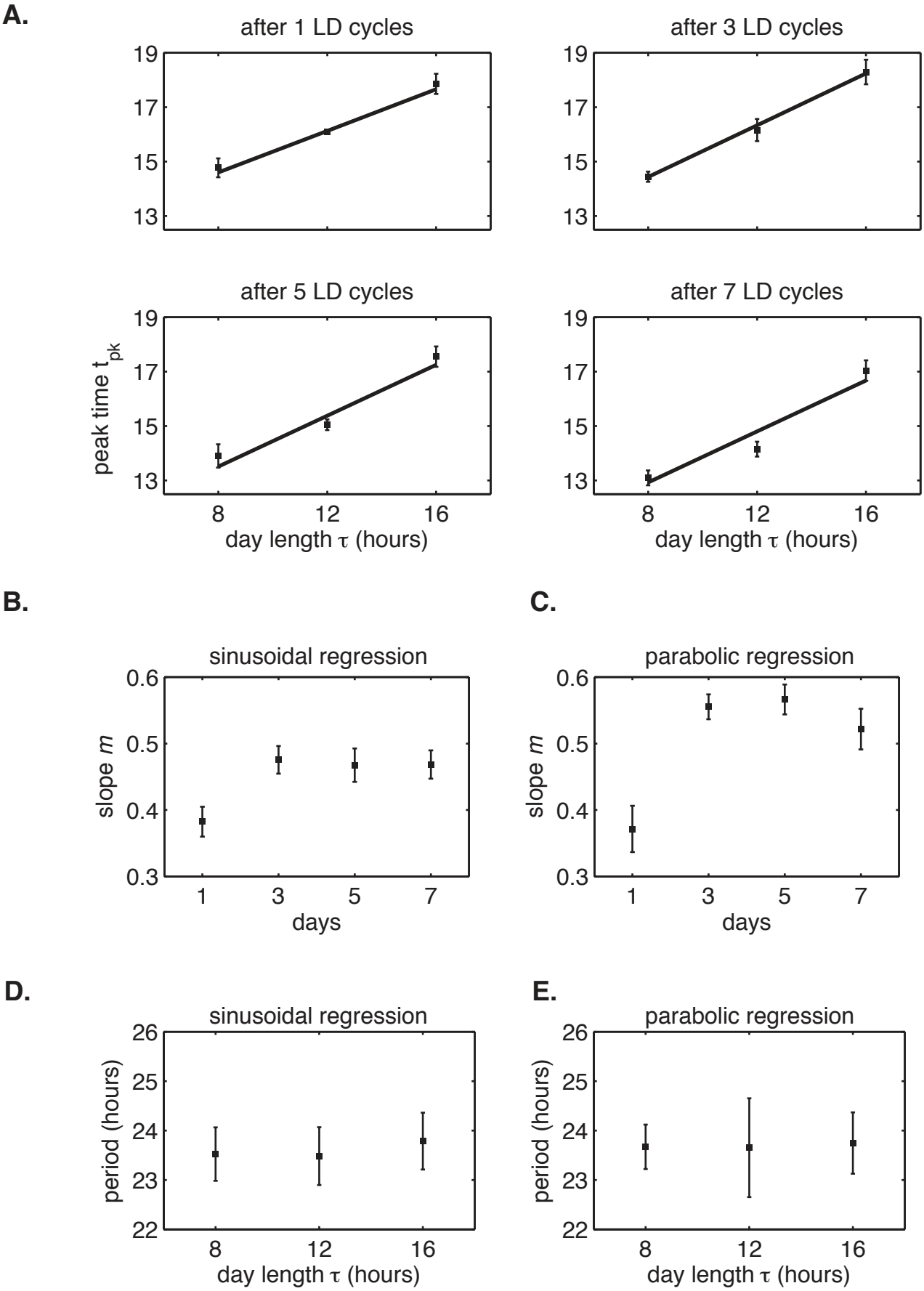

Figure 1—figure supplement 3.

A.

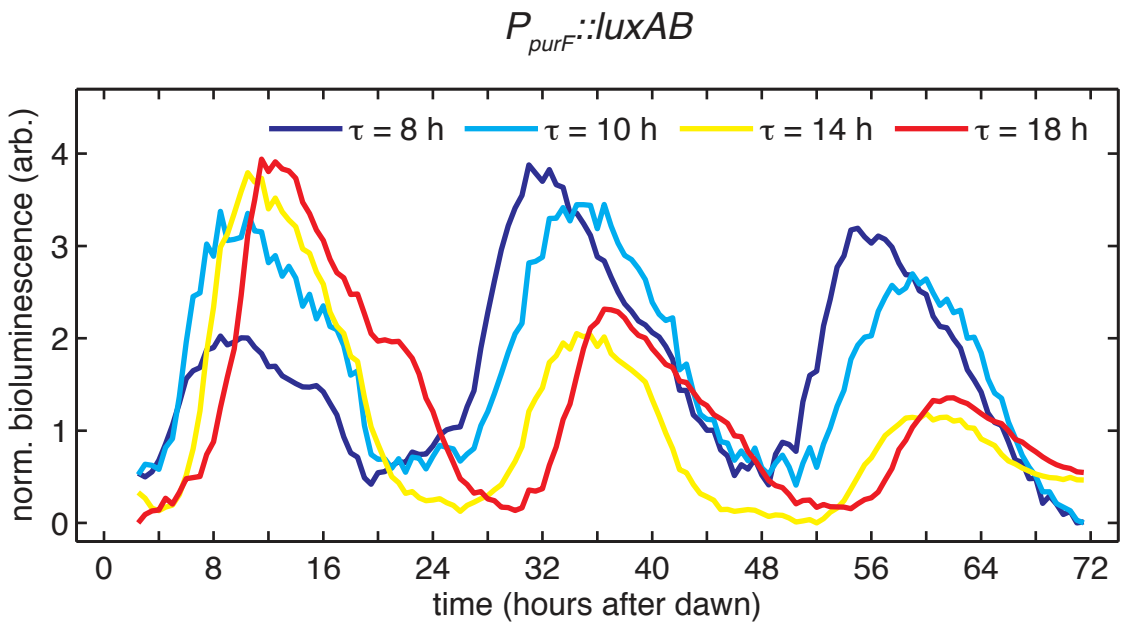

B.

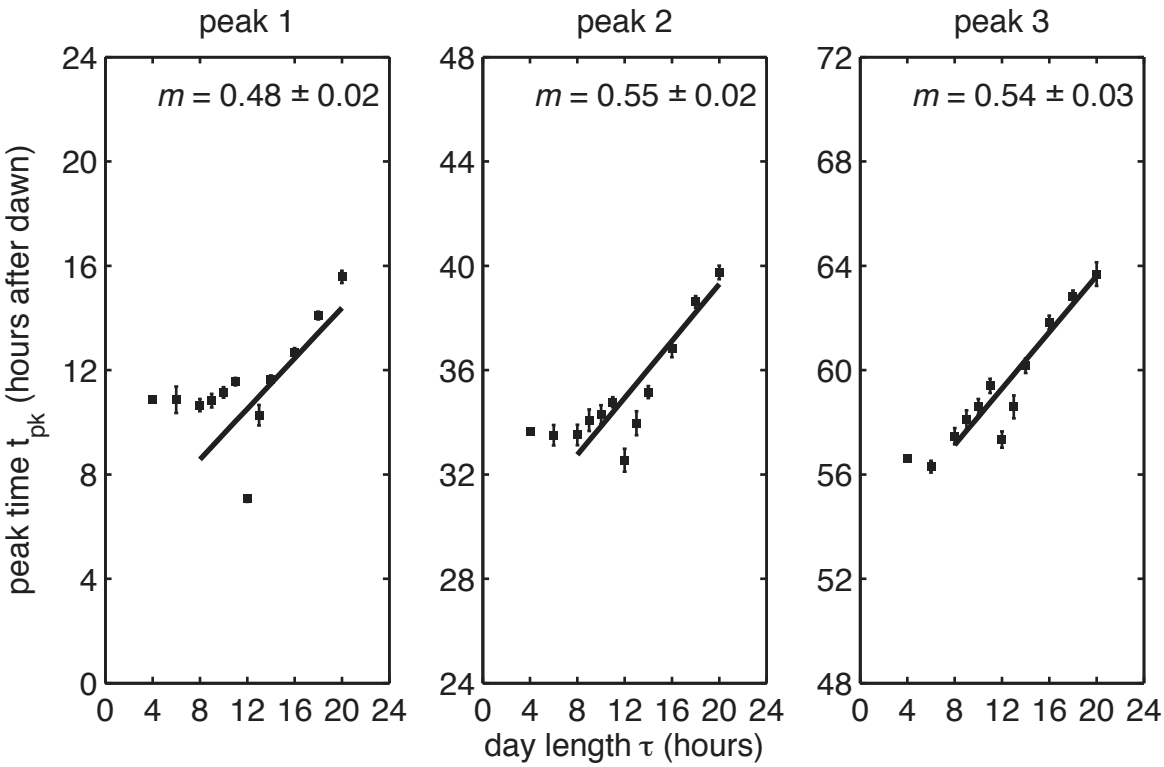

Figure 2.

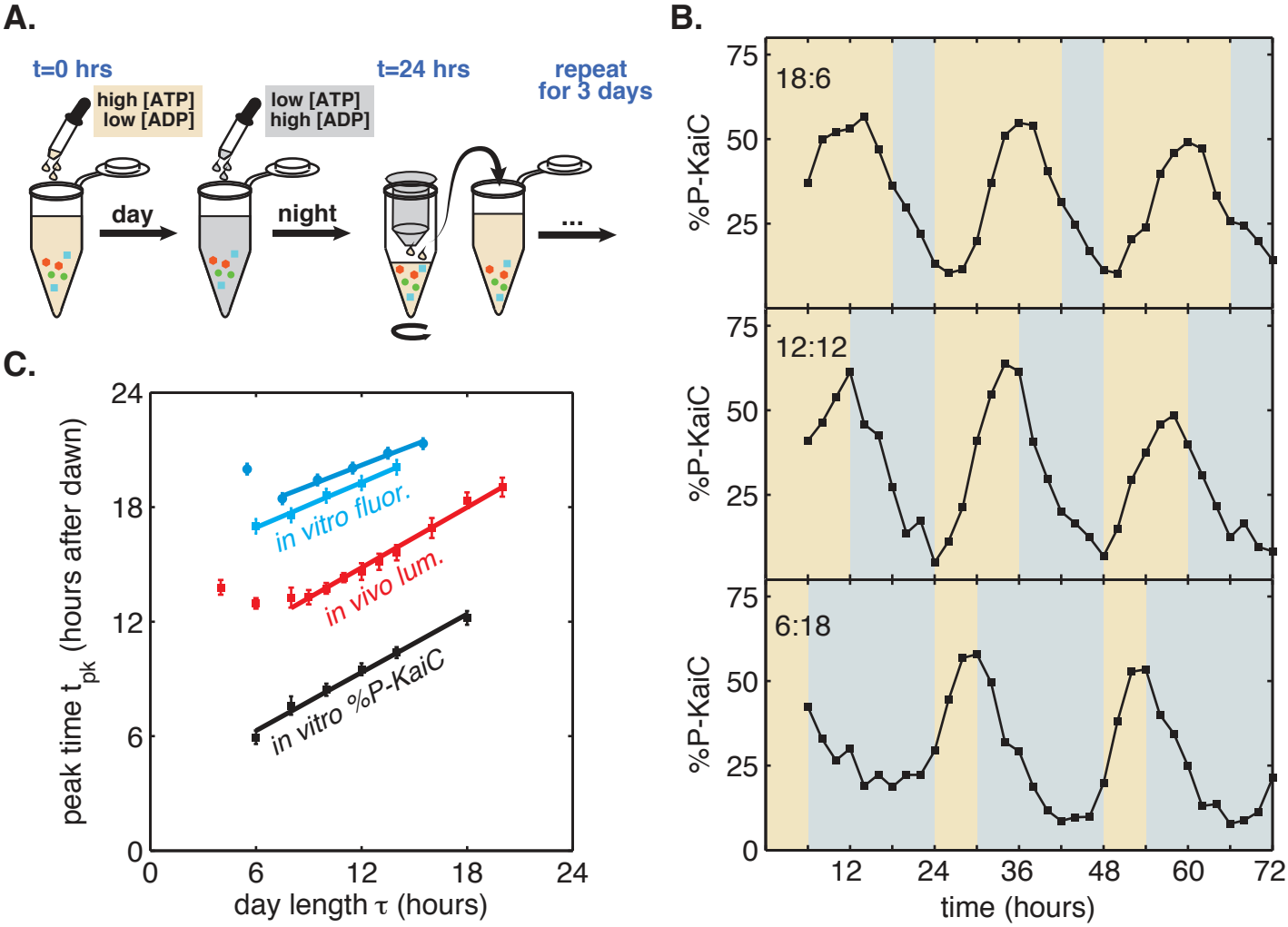
A.
t=0 hrs
high [ATP]
low [ADP]
day
low [ATP]
high [ADP]
night
t=24 hrs
repeat
for 3 days
...
B.
18:6
12:12
6:18
%P-KaiC
75
50
25
0
12
24
36
48
60
72
time (hours)
C.
in vitro fluor.
in vivo lum.
in vitro %P-KaiC
peak time t_{pk} (hours after dawn)
day length τ (hours)
0
6
12
18
24

Figure 2—figure supplement 1.

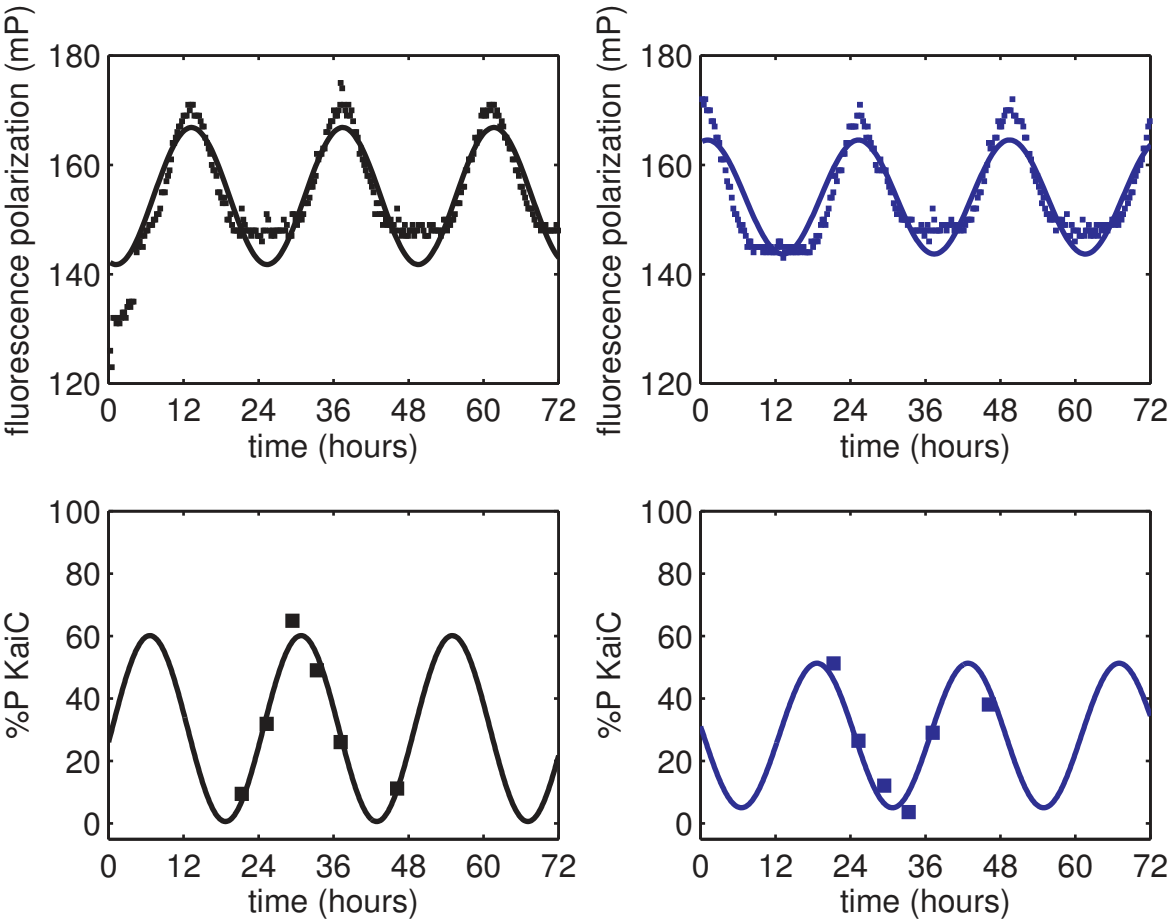

Figure 3.

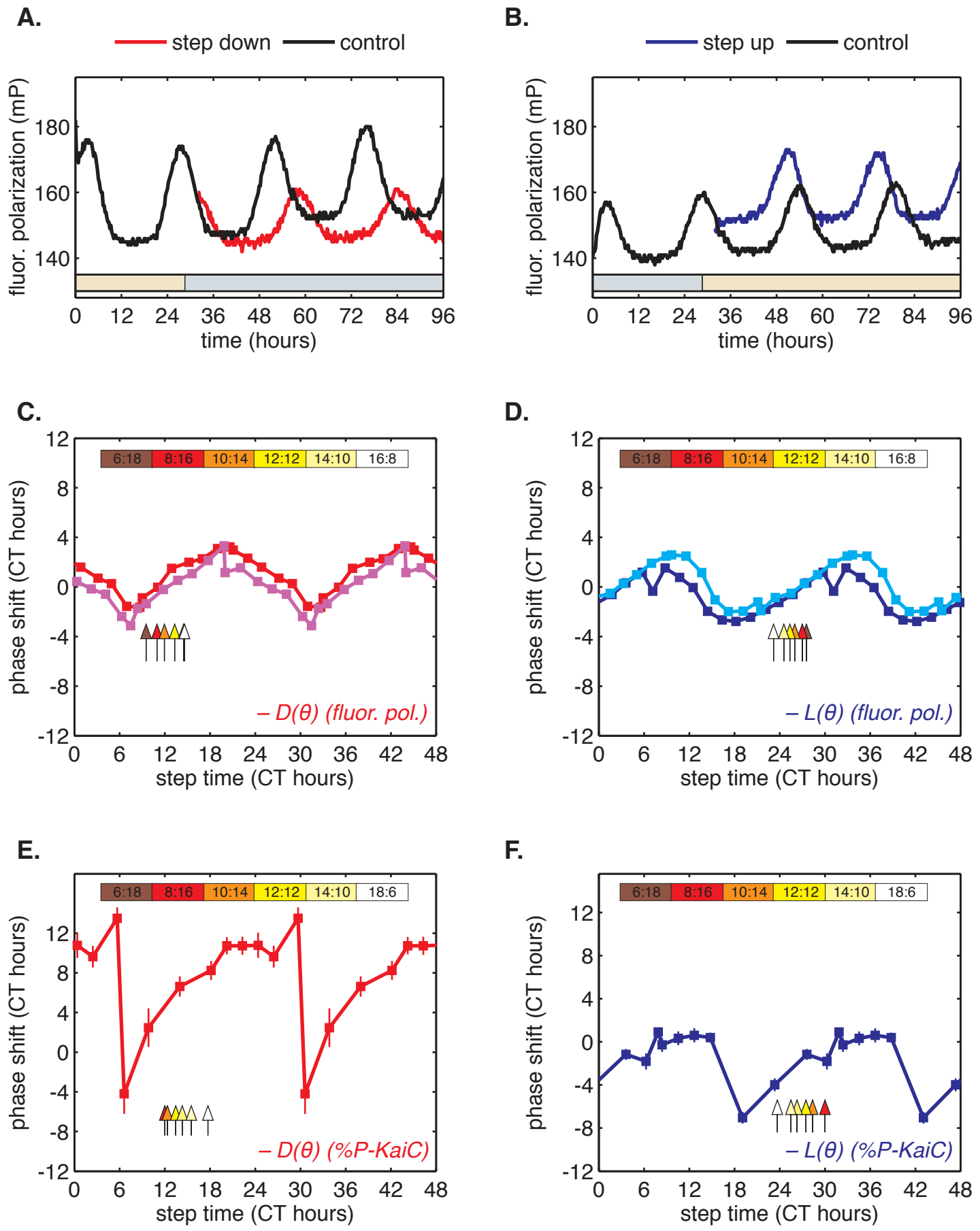
A.
step down
control
fluor. polarization (mP)
180
160
140
0 12 24 36 48 60 72 84 96
time (hours)
B.
step up
control
fluor. polarization (mP)
180
160
140
0 12 24 36 48 60 72 84 96
time (hours)
C.
6:18 8:16 10:14 12:12 14:10 16:8
phase shift (CT hours)
12 8 4 0 -4 -8 -12
– D(θ) (fluor. pol.)
0 6 12 18 24 30 36 42 48
step time (CT hours)
D.
6:18 8:16 10:14 12:12 14:10 16:8
phase shift (CT hours)
12 8 4 0 -4 -8 -12
– L(θ) (fluor. pol.)
0 6 12 18 24 30 36 42 48
step time (CT hours)
E.
6:18 8:16 10:14 12:12 14:10 18:6
phase shift (CT hours)
12 8 4 0 -4 -8 -12
– D(θ) (%P-KaiC)
0 6 12 18 24 30 36 42 48
step time (CT hours)
F.
6:18 8:16 10:14 12:12 14:10 18:6
phase shift (CT hours)
12 8 4 0 -4 -8 -12
– L(θ) (%P-KaiC)
0 6 12 18 24 30 36 42 48
step time (CT hours)

Figure 3—figure supplement 1.

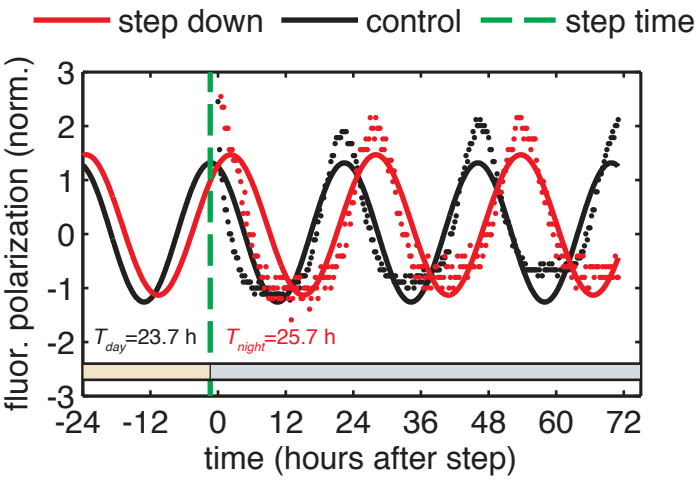

Figure 3—figure supplement 2

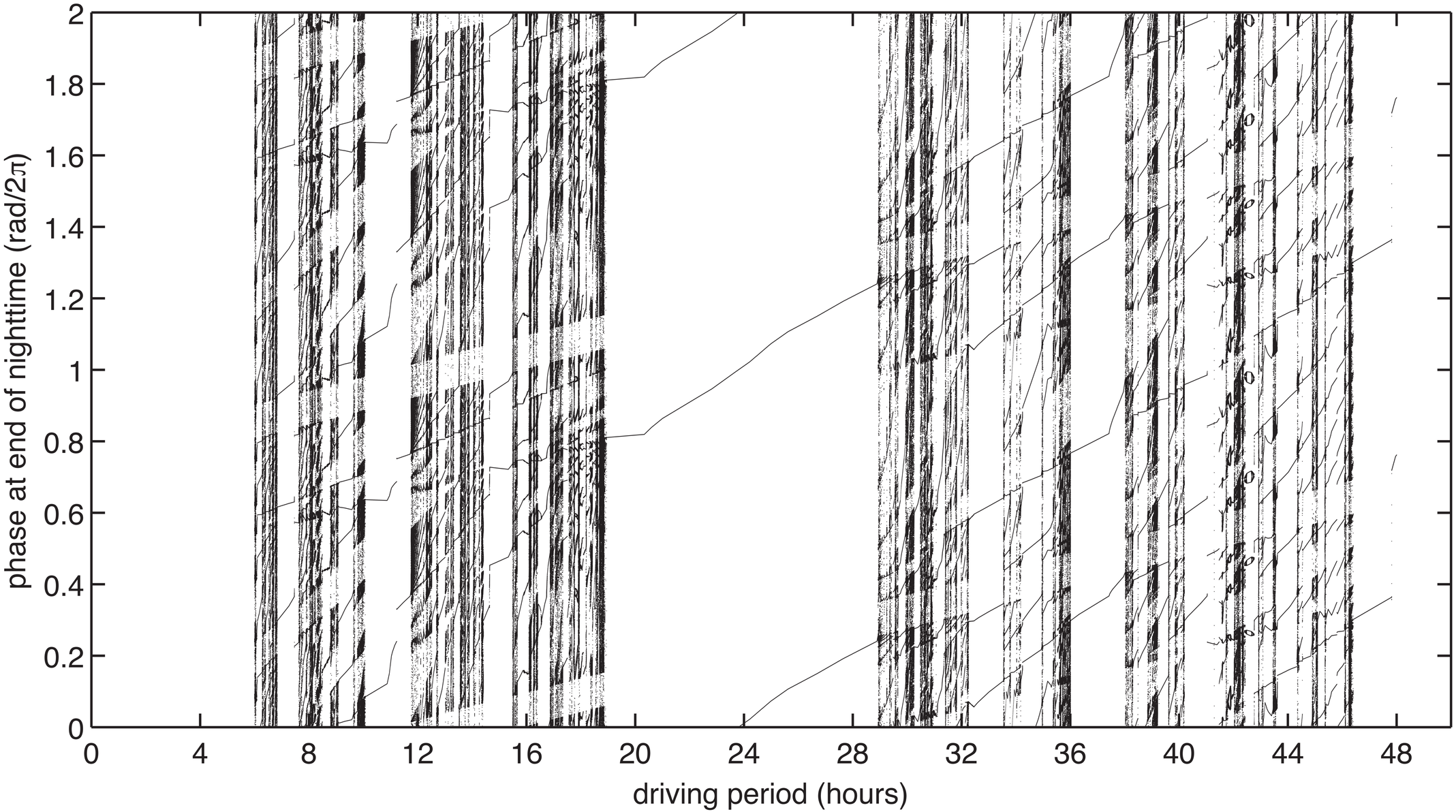

Figure 4.

A.

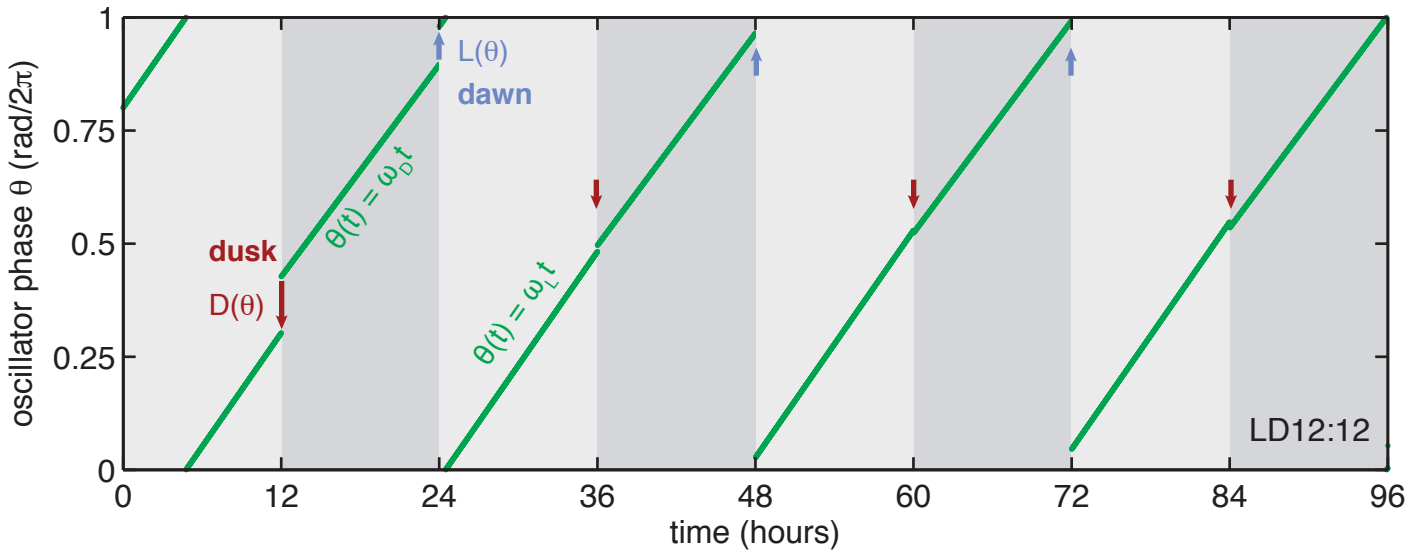
oscillator phase θ (rad/2π)
1
0.75
0.5
0.25
0
0
12
24
36
48
60
72
84
96
time (hours)
L(θ)
dawn
dusk
D(θ)
θ(t) = ω_D t
θ(t) = ω_L t
LD12:12

B.

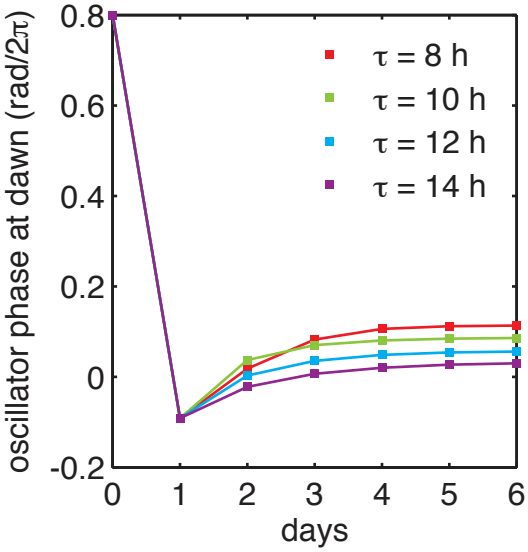
oscillator phase at dawn (rad/2π)
0.8
0.6
0.4
0.2
0
-0.2
0
1
2
3
4
5
6
days
τ = 8 h
τ = 10 h
τ = 12 h
τ = 14 h

C.

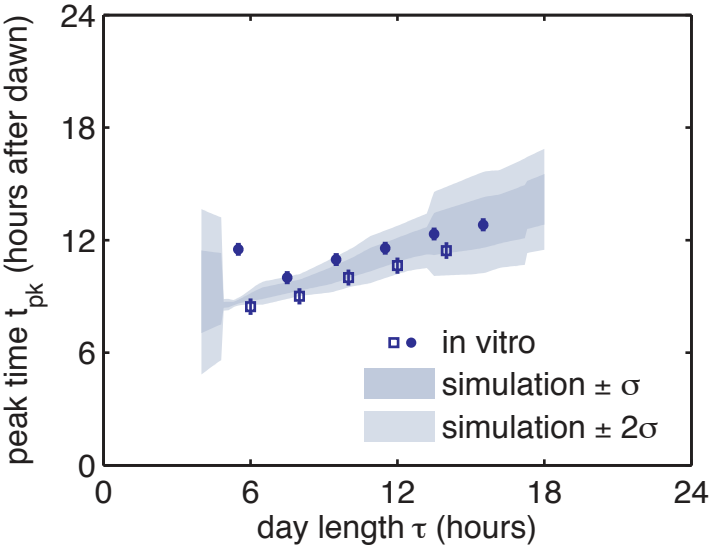
peak time t_pk (hours after dawn)
24
18
12
6
0
0
6
12
18
24
day length τ (hours)
in vitro
simulation ± σ
simulation ± 2σ

Figure 4—figure supplement 1.

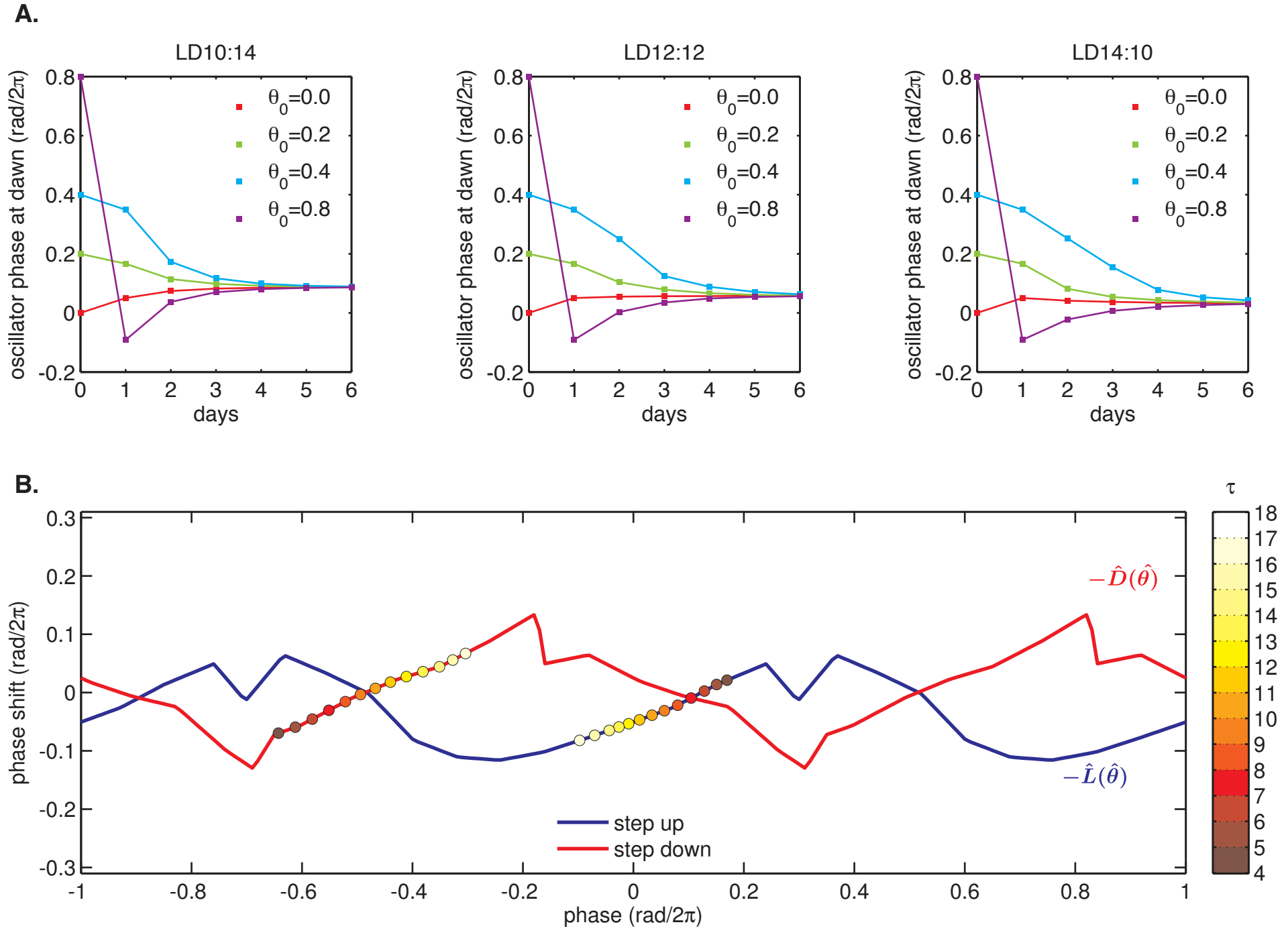

Figure 4—figure supplement 2.

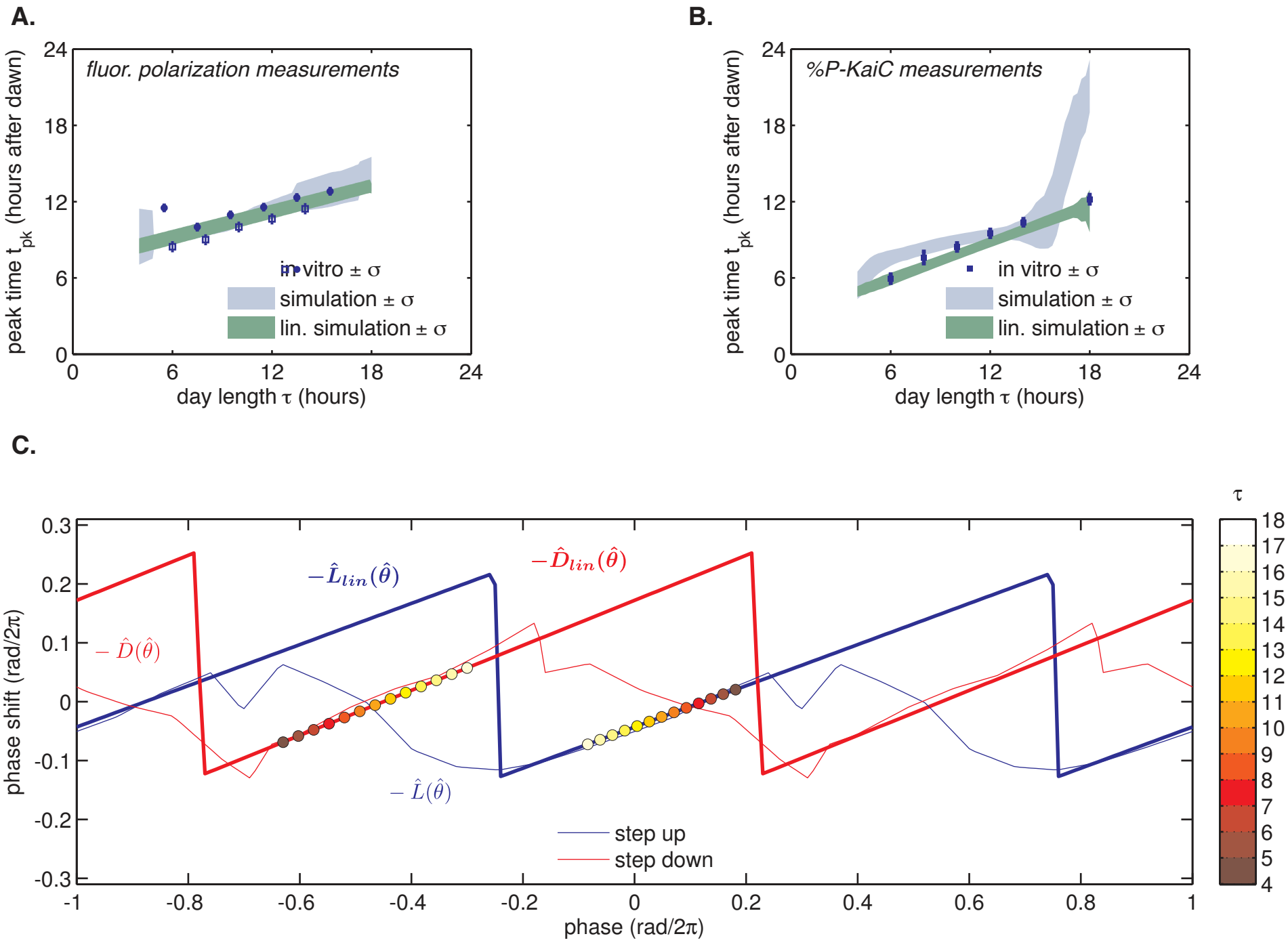

Figure 4—figure supplement 3.

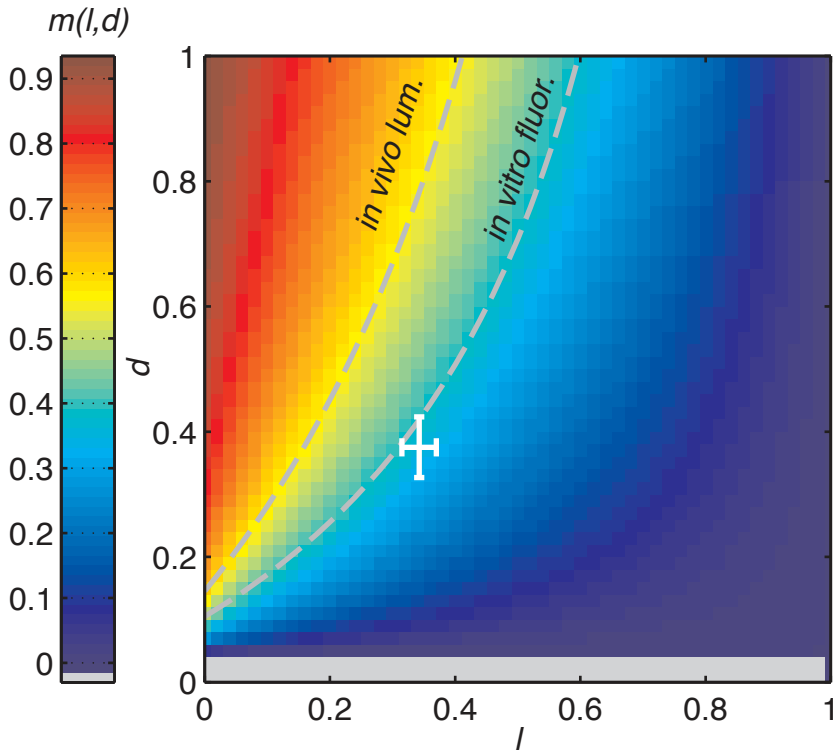

Figure 5.

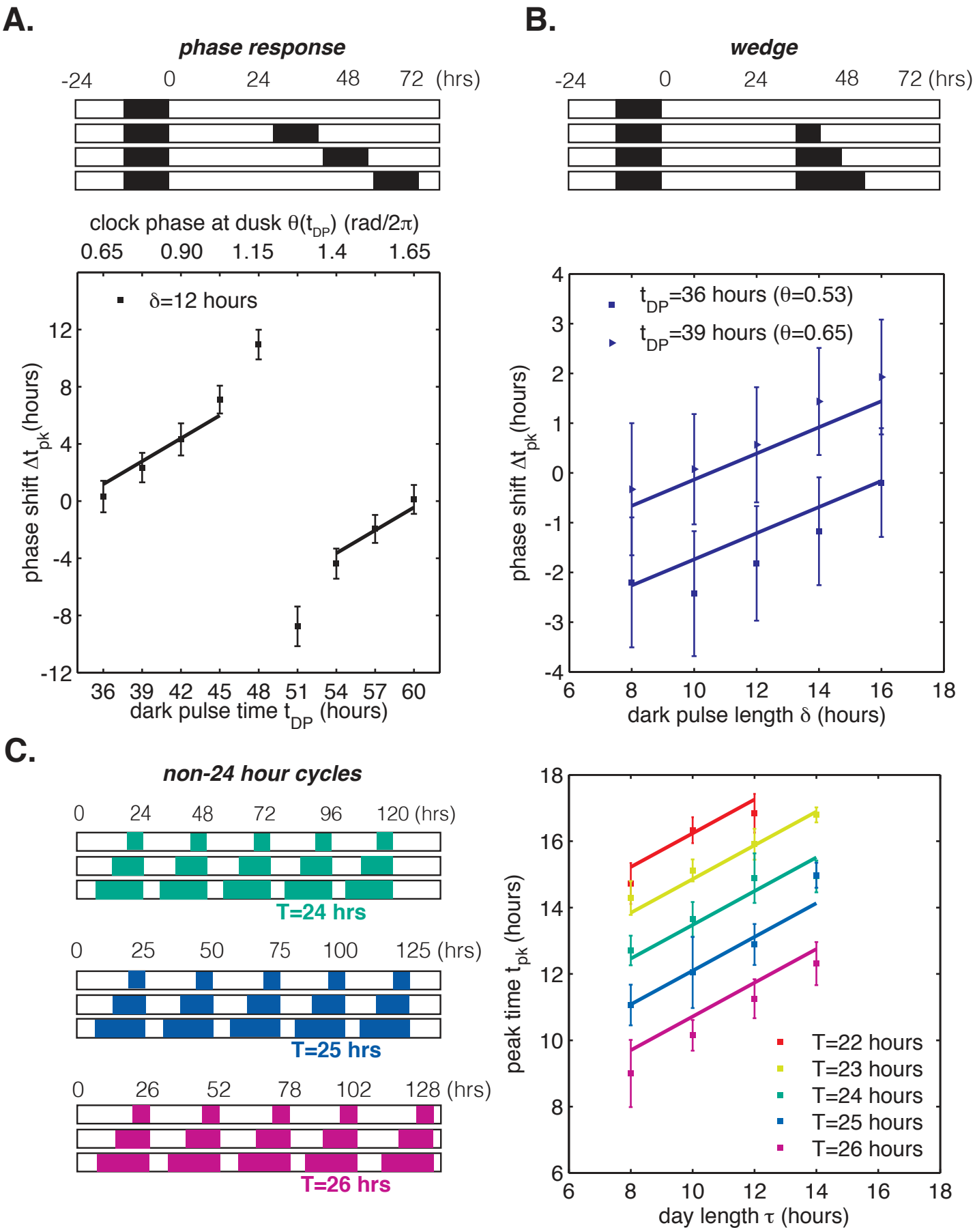
A.
phase response
-24
0
24
48
72 (hrs)
clock phase at dusk θ(t_DP) (rad/2π)
0.65
0.90
1.15
1.4
1.65
δ=12 hours
phase shift Δt_pk (hours)
12
8
4
0
-4
-8
-12
36
39
42
45
48
51
54
57
60
dark pulse time t_DP (hours)
B.
wedge
-24
0
24
48
72 (hrs)
t_DP=36 hours (θ=0.53)
t_DP=39 hours (θ=0.65)
phase shift Δt_pk (hours)
4
3
2
1
0
-1
-2
-3
-4
6
8
10
12
14
16
18
dark pulse length δ (hours)
C.
non-24 hour cycles
0
24
48
72
96
120 (hrs)
T=24 hrs
0
25
50
75
100
125 (hrs)
T=25 hrs
0
26
52
78
102
128 (hrs)
T=26 hrs
peak time t_pk (hours)
18
16
14
12
10
8
6
6
8
10
12
14
16
18
day length τ (hours)
T=22 hours
T=23 hours
T=24 hours
T=25 hours
T=26 hours

Figure 5—figure supplement 1.

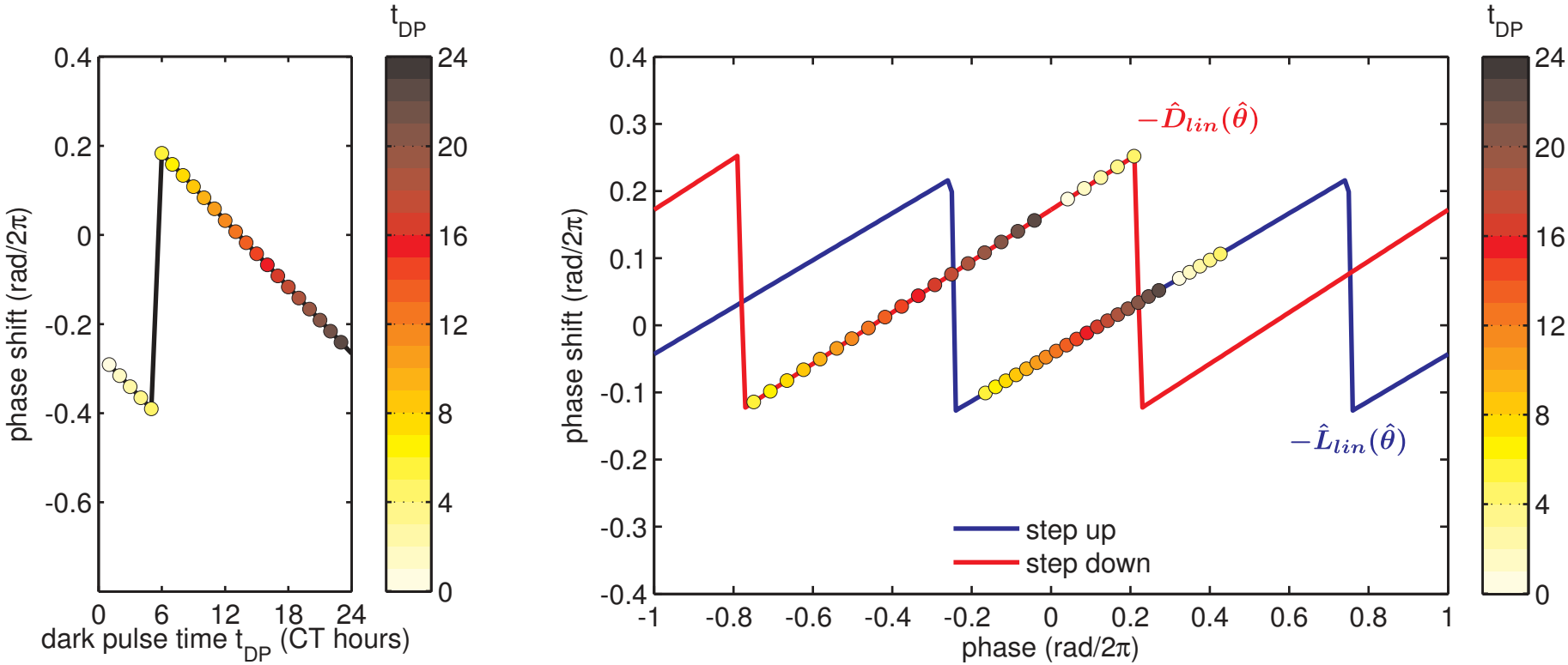

Figure 6.

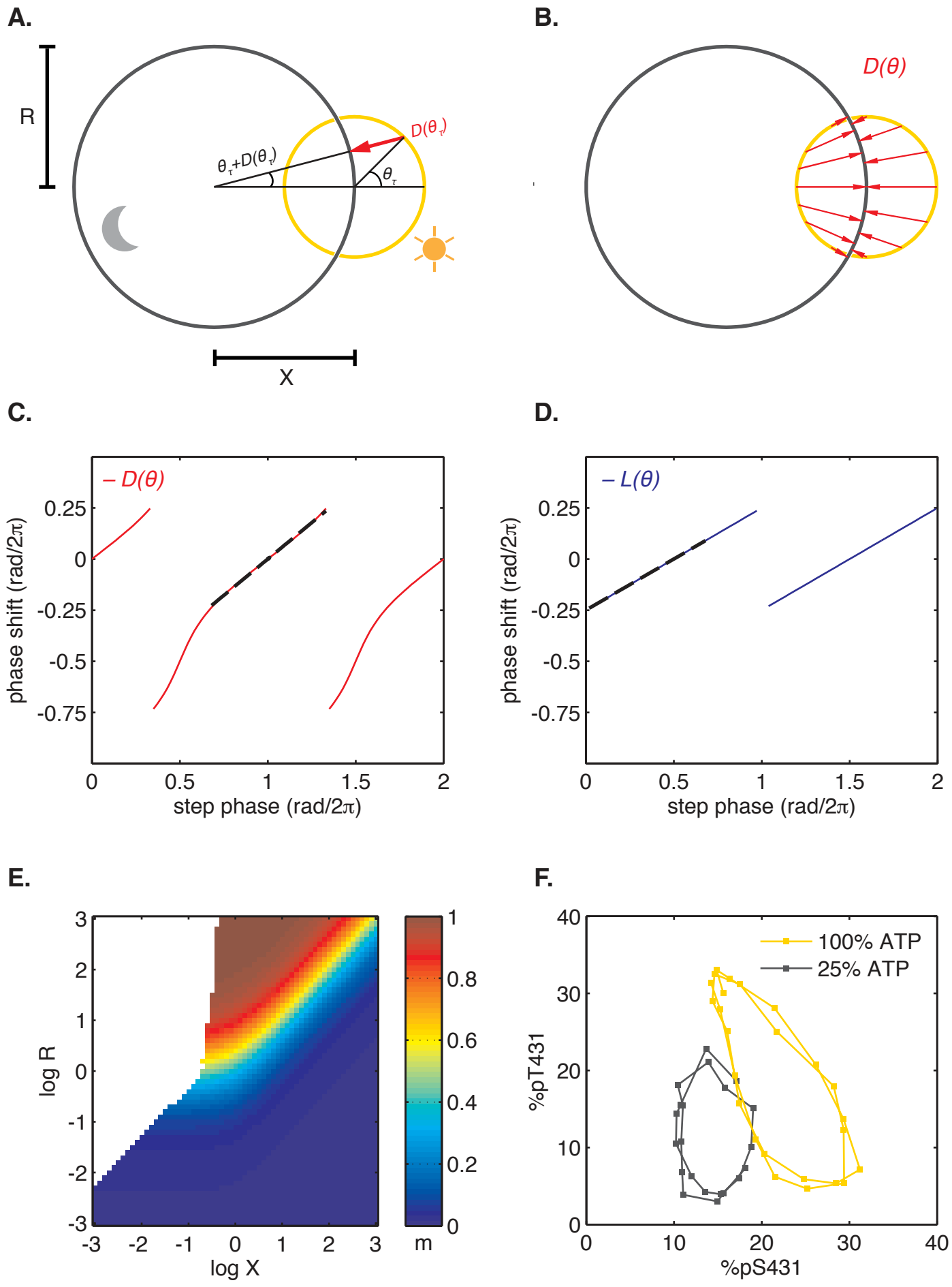
A.
R
X
$\theta_\tau + D(\theta_\tau)$
$D(\theta_\tau)$
θ_τ
B.
$D(\theta)$
C.
$-D(\theta)$
phase shift (rad/2π)
step phase (rad/2π)
D.
$-L(\theta)$
phase shift (rad/2π)
step phase (rad/2π)
E.
log R
log X
m
F.
100% ATP
25% ATP
%pT431
%pS431

Figure 6—figure supplement 1.

A. logR=-1, logX=0.5, m≈0

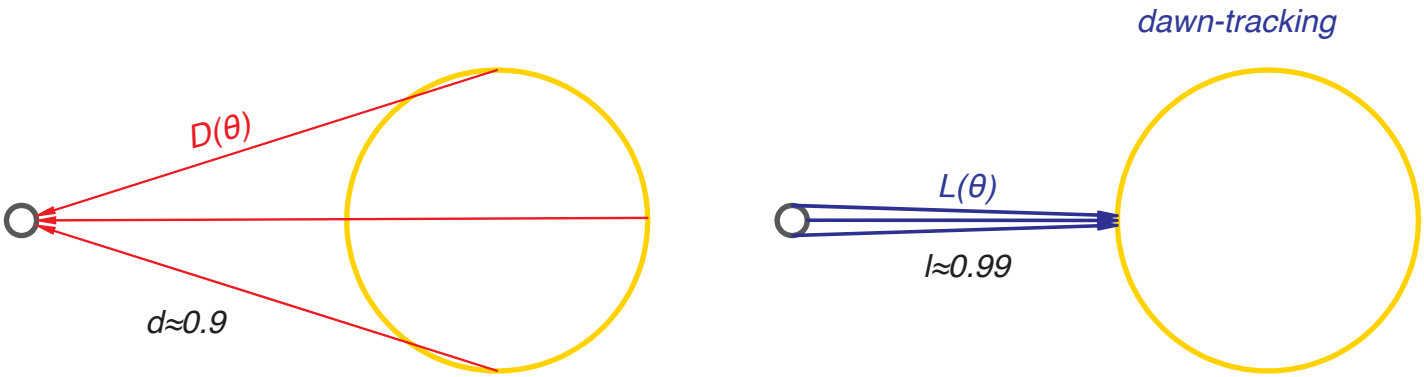

B. logR=0.4, logX=0.5, *m*≈0.4

C. logR=1.5, logX=0.5, *m*≈1

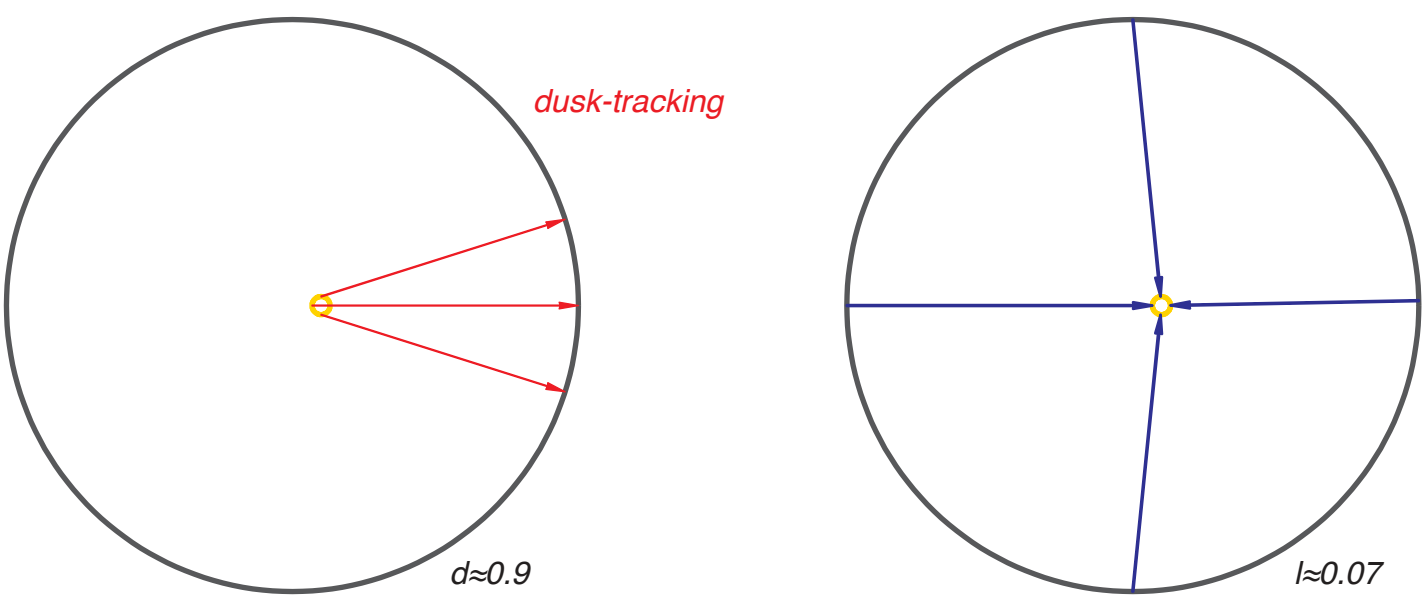

Figure 6—figure supplement 2.

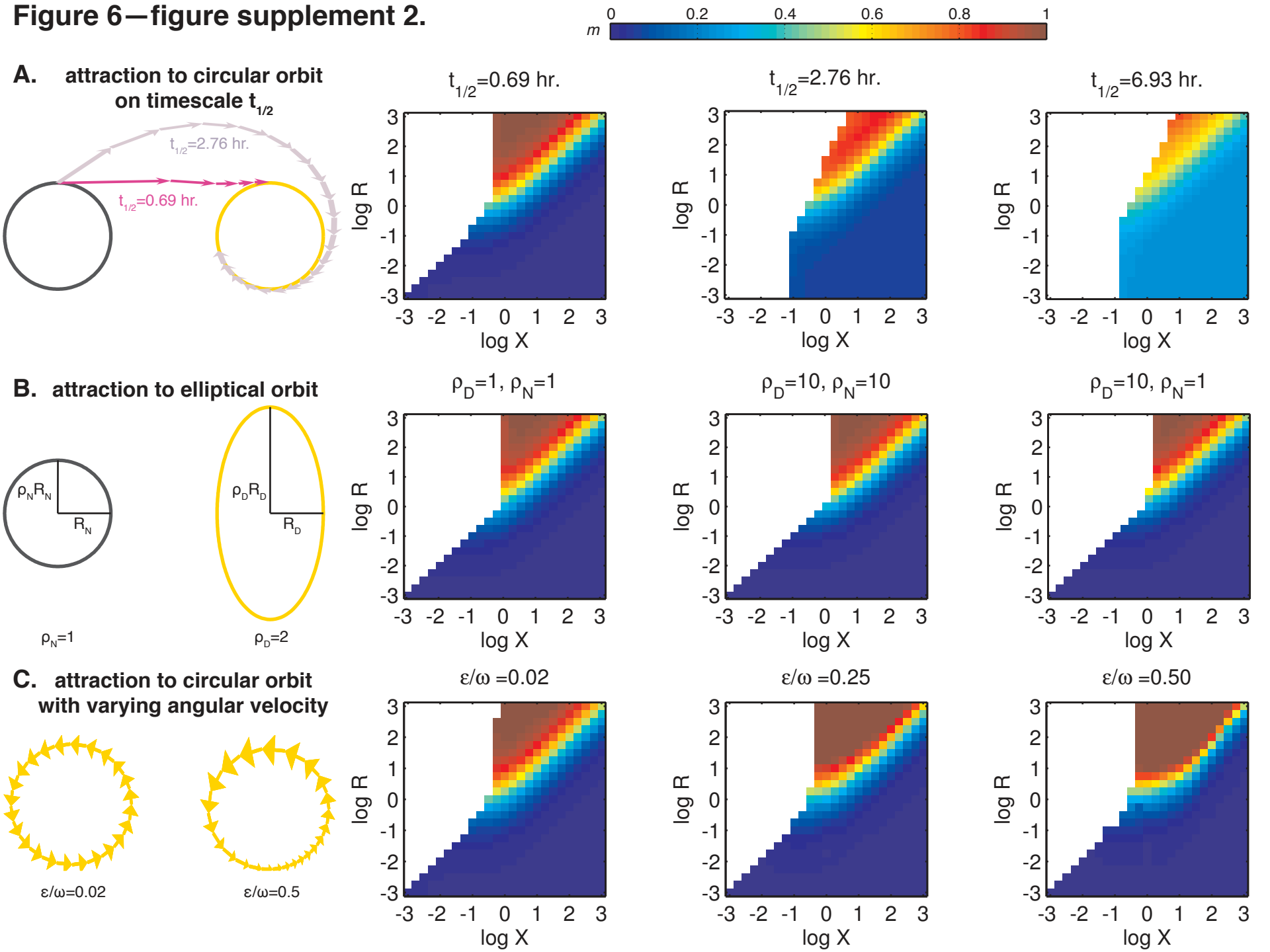

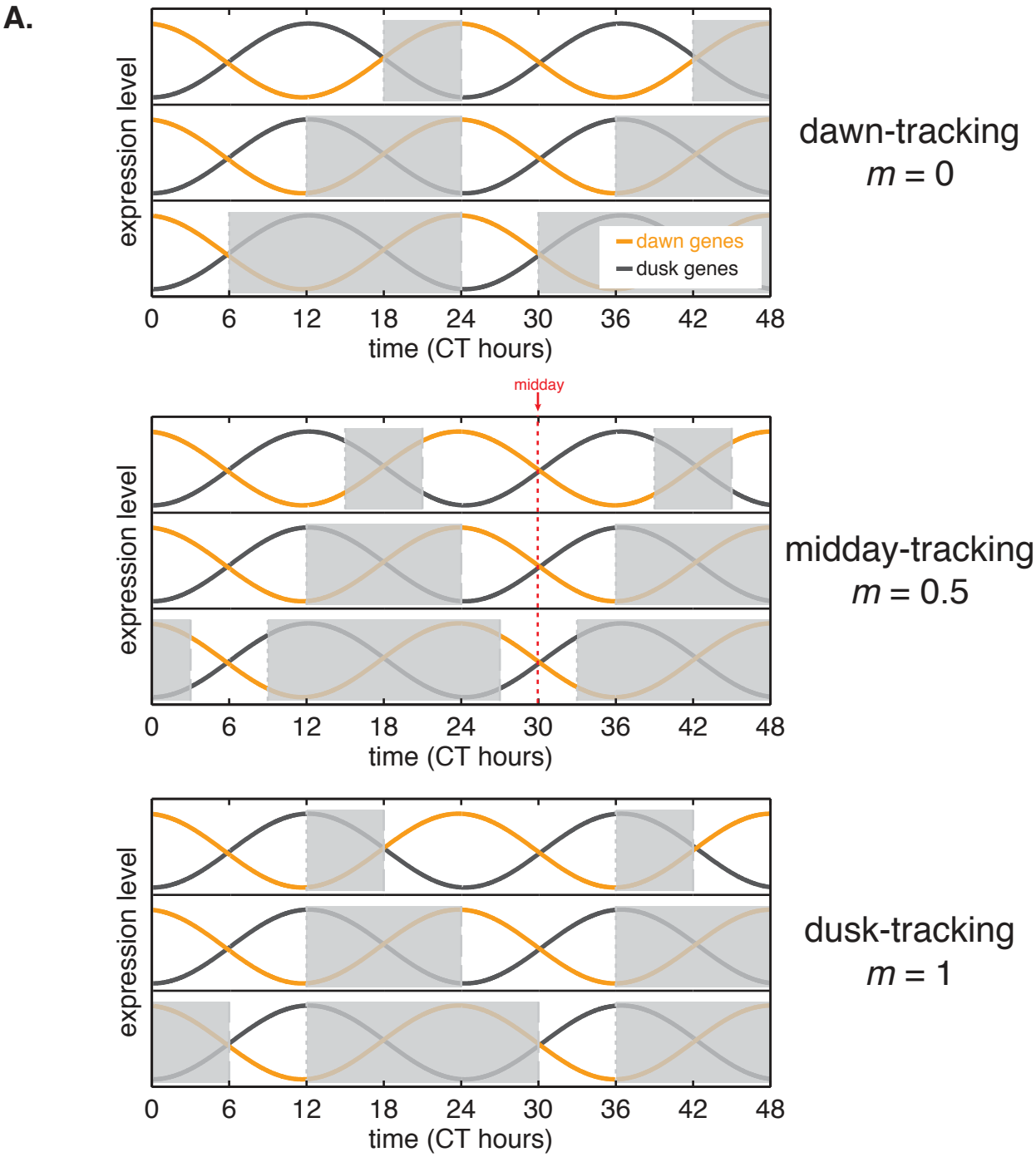

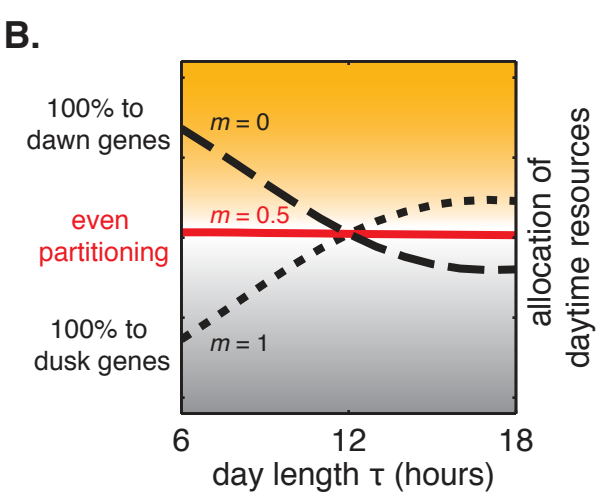

Figure 6—figure supplement 3.

Figure—Mathematical Appendix.

A.

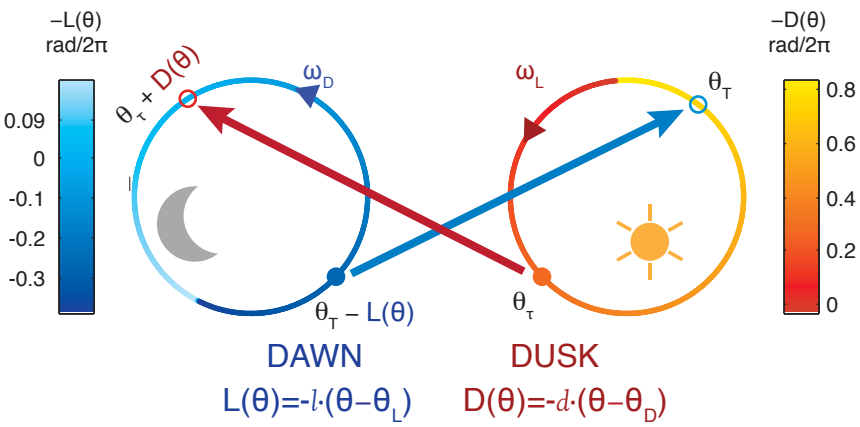

B.

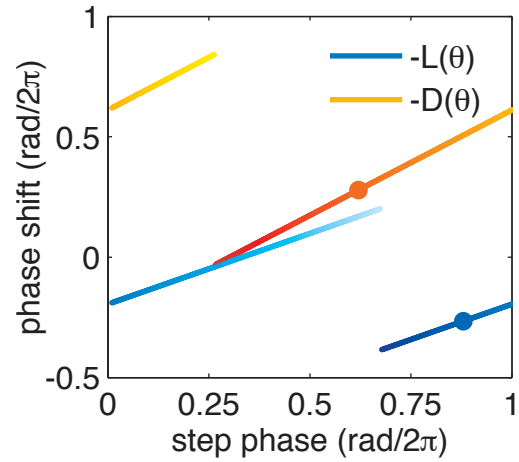

C. ***phase response***

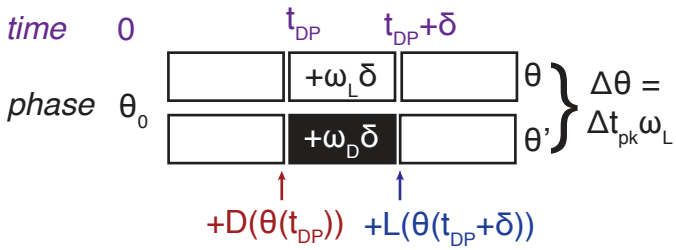

$$\Delta t_{pk}(t,\delta) = \theta_t\left(\frac{1}{\omega_L\beta_2}\right) + \delta\left(1+\frac{\beta_1}{\beta_2}\right) - C_1$$

$$\beta_1 = -\frac{(1-l)\frac{\omega_D}{\omega_L}}{d+l-ld} \qquad \beta_2 = \frac{1}{d+l-ld}$$

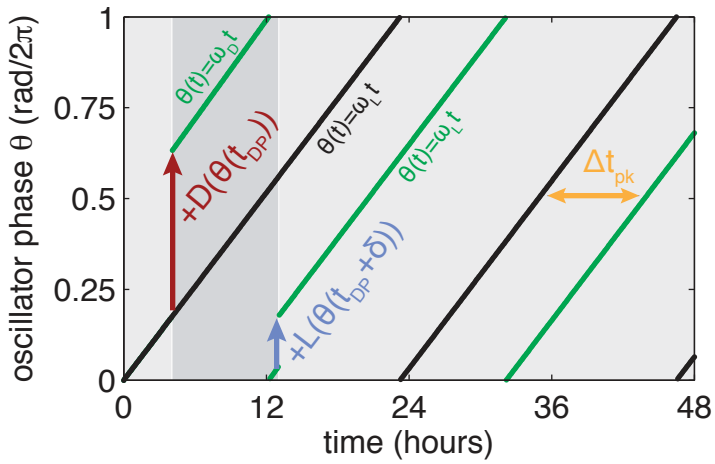

D. ***seasonal entrainment***

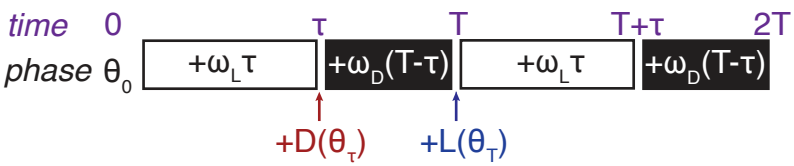

$$t_{pk} = \tau(1-\beta_1-\beta_2) + T\beta_1 + C_2$$
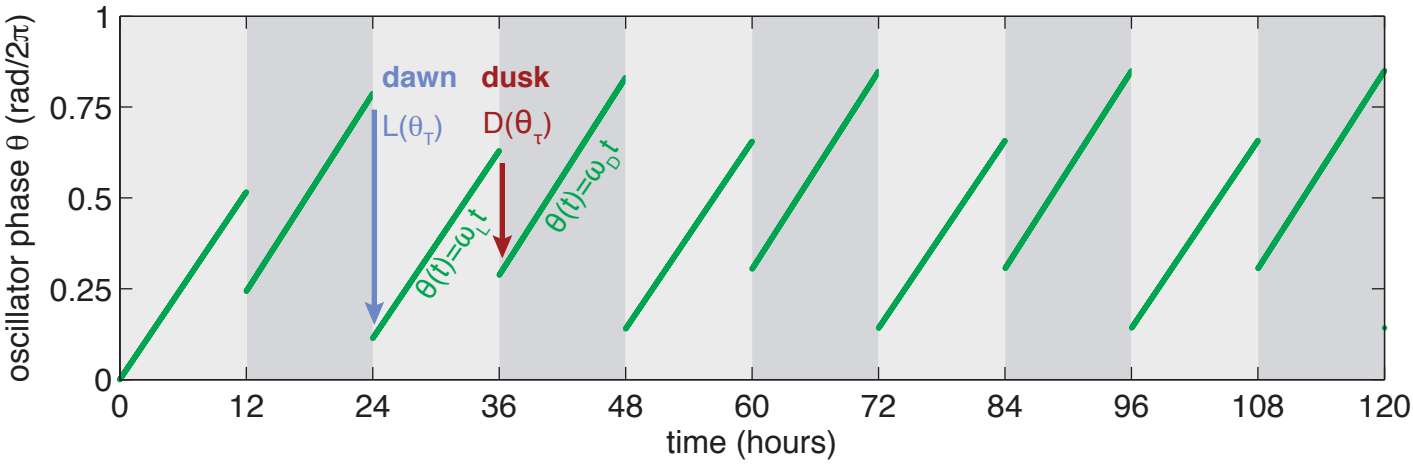
$$\beta_1 = -\frac{(1-l)\frac{\omega_D}{\omega_L}}{d+l-ld} \qquad \beta_2 = \frac{1}{d+l-ld}$$